Abstract

Lu, Wei. **Radiation damage to the materials at SINQ facilities**. (Under the instruction of Prof. Monroe S. Wechsler.)

SINQ (Swiss Spallation Neutron Source) was built to meet the surging demand for neutrons. It was the first continuous spallation neutron source. Taking advantage of SINQ facilities, the SINQ Target Irradiation Program (STIP) is an international collaboration among many well known laboratories and research agencies to study the microstructures and mechanical properties of structural materials in a spallation spectrum. Target 5 is the currently operating target at SINQ in STIP III. The radiation damage (displacement, hydrogen and helium production) calculations were performed for Target 5 and partly for Target 3. The results of the calculations provide an important basis for further experimental explorations. As a complete investigation, the cross sections were developed for some materials, the physics of spallation reactions was studied to explore the neutron production capability of the material, and a new method was conducted in addition to the conventional calculations. The errors of the calculations were analyzed and some of the calculations results were compared to the available experimental data.

The AlMg3 entrance windows of Target 5 received a displacement production of 5.2-5.4 dpa, which indicated a significant radiation-induced strengthening and hardening of the aluminum alloy and suggested further examination on the entrance windows for the working life time.

Radiation damage to the materials at SINQ facilities

by

Wei Lu

A dissertation submitted to the Graduate Faculty of
North Carolina State University
in partial fulfillment of the requirements for
the Degree of Doctor of Philosophy

Department of Nuclear Engineering

Raleigh, North Carolina
August, 2003

Approved by:

Dr. Monroe S. Wechsler, Co-Chair	Dr. Man-Sung Yim, Co-Chair
Dr. Robin P. Gardner	Dr. Robert E. Funderlic

Biography

Wei Lu was born to Mr. Youzhong Lu and Mrs. Xiu'e Liu in Zhoushan, Zhejiang Province, China in 1974, an island in the east frontier of China where the tragic history of neoteric China was started. His life was filled with joy in the middle and high school since he met Miss Qi Qi.

In 1993, he went to the north of China for the college education in Tsinghua University, Beijing. He graduated in 1997 with a B.S. majoring in Engineering Physics, and continued as a master student in the Nuclear Energy Technology Institute of Tsinghua University under the instruction of Prof. Jinhai Bo. During the years in the master program, the author focused his work on the thermal hydraulic safety of a low temperature reactor. In July, 1999, he was awarded a M.S. of Nuclear Science and Technology. Soon after his graduation, he married his favorite girl, Miss Qi Qi, in the hometown. One week later, he was on his trip to U.S. for his Ph. D study.

The author became a Ph.D student in the department of Nuclear Engineering in North Carolina State University in Raleigh, North Carolina, in August, 1999. He was instructed by Profs. Wechsler and Dudziak, and later Prof. Wechsler solely, in the research of radiation damages to the material. In spring 2000, he reunited with his wife, whose support helped him concentrate on the study and work for the Ph.D degree.

Acknowledgements

I would express my deep and genuine gratefulness to Prof. Monroe S. Wechsler, my advisor, who took extraordinary efforts in instructing and assisting me throughout the research of radiation damage to the material and the work of dissertation. His guidance and encouragement led me overcome the difficulties in the research work. His extensive knowledge and creative ideas intrigued our discussions. His attitude to the science and work is a never-forgettable model which I would like to follow. Furthermore, his continuous support laid a smooth way to my study of a Ph.D degree.

I am also thankful to Prof. Man-Sung Yim for co-chairing the advisory committee, during which he helped me through various problems of academic affairs. I learned a lot from the four courses he instructed and his views into resolving problems. To Prof. Robin P. Gardner for leading me into the fundamentals of Monte Carlo simulation at the beginning of my Ph. D study and continuing offering advises thereafter, and being in the advisory committee. To Prof. Robert E. Funderlic for being my minor advisor and delivering me his best computer course. To Prof. Dudziak for hosting and instructing me in the research group before he left North Carolina.

Dr. Yong Dai of Paul Scherrer Institute (PSI), Switzerland and his research group sponsored the project. My gratitude to him is always specially for his generous help in PSI, where the preliminary work of the research was completed. I greatly appreciate the liberal assistance from Dr. Eric J. Pitcher of Los Alamos National Laboratory, and Dr. Phillip D. Ferguson of Oak Ridge National Laboratory during the research work.

Finally, I would thank my wife, Qi Qi, for her love and support, and my parents for their forever love and understanding.

Table of contents

List of Tables vii

List of Figures viii

Chapter 1 Introduction 1

Chapter 2 Radiation damage physics and calculation methods 5
2.1 Spallation reactions----------5
2.2 Radiation effects----------7
2.2.1 Swelling----------7
2.2.2 Hardening and embrittlement---------- 8
2.2.3 Other effects----------11
2.3 Radiation damage calculations----------12
2.3.1 Calculation of displacements----------13
2.3.2 Calculation of gas productions----------18

Chapter 3 MCNPX 20
3.1 Introduction of MCNPX---------- 20
3.2 New characteristics of MCNPX----------21
3.3 Physics models in MCNPX----------23

Chapter 4 SINQ and STIP 26
4.1 SINQ development----------26
4.1.1 The need for neutrons----------26
4.1.2 SINQ introduction---------- 27
4.2 SINQ target irradiation program (STIP)---------- 30

Chapter 5 Neutron yields 32
5.1 Introduction of Calculations---------- 32
5.2 Results and discussion---------- 34
5.2.1 Calculations validity checking----------34
5.2.2 Neutron productions versus incident proton energy----------35
5.2.3 Neutron productions versus target materials---------- 39
5.2.4 Summary and conclusions---------- 40

Chapter 6 Radiation damage calculations 42
6.1 Geometry modeling ----------42
6.1.1 SINQ configuration and Target 5----------42
6.1.2 Specimen rods inside Target 5----------45
6.1.3 Entrance windows---------- 52
6.2 Source beam profiles---------- 54
6.3 Flux calculations---------- 58
6.3.1 Flux distribution in Target 5----------58
6.3.2 Fluxes at the specimen rods---------- 62
6.3.3 Fluxes at the entrance windows----------67
6.4 Cross sections---------- 71
6.4.1 Cross section calculations---------- 71

6.4.2 Cross section analysis----------74
6.5 Results of radiation damage productions ----------78
6.5.1 Radiation damage productions at the entrance windows---------78
6.5.2 Radiation damage productions at the specimen rods----------82
6.6 Summary and conclusions----------86

Chapter 7 Analysis and Discussion 88
7.1 New method in calculations----------88
7.2 Errors and accuracy of the calculations----------93
7.2.1 Errors due to cross sections----------93
7.2.2 Comparison to the experimental data----------96
7.3 Analysis of the calculation results----------98
7.3.1 STIP I and STIP III comparison----------98
7.3.2 Significance of the radiation damage productions----------102
7.4 Other factors of radiation damage ----------104
7.5 Summary and conclusions ----------105

Chapter 8 Conclusions 107

Bibliography 112

Appendix A 118

Appendix B 124

List of Tables

TABLE 2.1 Recommended values for displacement threshold energy.---------- ---14

TABLE 3.1 Particles traceable in MCNPX, "symbol" is the symbol used in MCNPX to designate the particles, "IPT" is the index of particle tracing in MCNPX (after [8]). ----------21

TABLE 4.1 Plan of the SINQ target irradiation program, PIE is the post irradiation examination, the doses are estimated maximum values inside the target. ----------31

TABLE 5.1 Fitting results for neutron production at higher incident energies.---------38

TABLE 6.1 STIP III specimen material compositions.----------48

TABLE 6.2 Materials in specimen rods.----------49

TABLE 6.3 Materials compositions of "averaged" specimen rods.----------50

TABLE 6.4 Displacement, helium, and hydrogen at the lowest tips of entrance windows, Beam 2, incident proton energy, 570 MeV, 10 Ahr of irradiation.----------81

TABLE 6.5 Displacement, helium and hydrogen productions at the center of specimen rods of SS316, Beam 2,10 Ahr of irradiation.----------84

TABLE 7.1. Summary of radiation damage productions at the lowest tip of outer entrance window in Target 3 for STIP-I after an exposure of 6.8 Ah.----------92

TABLE 7.2 The perturbation of displacement production due to neutrons of energies below 20 MeV in percentage versus the change of densities of spallation material, Pb, and structure material, Al.---------95

TABLE 7.3. Comparison of calculation results and experimental data for helium and hydrogen production in Target 3 after an exposure of 6.8 Ah.----------98

TABLE 7.4. Displacement concentrations at the entrance windows of SINQ Targets 3 and 5. ----------102

TABLE A.1 Displacement, helium and hydrogen productions at the center of specimen rods of Al6061, 9Cr-1Mo and Zirc-4, Beam 2, 10 Ah of irradiation.----------119

List of Figures

FIG. 2.1 Schematic diagram of the spallation process (an improved graph from Reference [8]).----------6

FIG. 2.2 Stress-strain curves for annealed 316L stainless steel after irradiation in the LANSCE irradiation facility [5].----------8

FIG. 2.3 SEM Micrograph of T91 specimen after an irradiation dose of 9.4 dpa [14].----------10

FIG. 2.4 Dose dependence curves for the $DBTT_{SP}$ and USE_{SP} of T91 steel [15].----11

FIG. 2.5 Transferred recoil energy, T dependence curve of damage efficiency $\xi(T)$ (after [28]).----------16

FIG. 3.1 Part of an experimental simulation using the radiography tally [32].--------23

FIG. 4.1 Model of SINQ [1].----------28

FIG. 4.2 The moderator tank of SINQ before installation [1].----------29

FIG. 4.3 An overview of the SINQ [1].----------29

FIG. 5.1 Part of MCNPX output file.----------33

FIG. 5.2 Comparison between calculated neutron productions and measured ones.----------35

FIG. 5.3 Neutron productions of infinite targets for different materials.----------38

FIG. 5.4 Fitting analysis of neutron production at lower incident energies.----------39

FIG. 5.5 Neutron productions versus atomic mass number of different materials.---40

FIG. 6.1 A schematic diagram of Target 5(Rods 1 to 17 contain specimens for irradiation).----------43

FIG. 6.2 Cross section diagram of 8th layer of specimen rodsin Target 5 (not to scale).----------44

FIG. 6.3 Axial and radial cross section diagram of Specimen Rod 1 in Target 5.----46

FIG. 6.4 An example of specimen package [3].----------47

FIG. 6.5(a) Sampling points at the outer entrance window of Target 5.----------53

FIG. 6.5(b) Enlarged part of tally volume of P0 at the outer entrance window

of Target 5 (not to scale).----------53

FIG. 6.6(a) STIP III proton source beam profile, Beam 1 (measured), incident proton energy, 575 MeV.----------55

FIG. 6.6(b) STIP III proton source beam profile, Beam 2 (truncated Gaussian), incident proton energy, 570 MeV (σ_x= 2.12 cm, σ_y= 3.56 cm, confined by an ellipse R_x=4.24 cm, R_y=7.12 cm).----55

FIG. 6.7(a) Current density per mA of total current vs distance along the X direction at y = 0 for Beam 1 (measured) and Beam 2 (truncated Gaussian).----------57

FIG. 6.7(b) Current density per mA of total current vs distance along the Y direction at x = 0 for Beam 1 (measured) and Beam 2 (truncated Gaussian).----------57

FIG. 6.8 Proton ((a) ~ (b)) and neutron ((c) ~ (d)) flux at SINQ Target 5, Beam 2.----------59

FIG. 6.9 Proton (a) and neutron (b) flux on Target 5 with part of Target 5 structure imposed for Beam 2.----------61

FIG. 6.10 (a)Proton and (b)neutron differential flux spectra at the centers of specimen rods for Beam 2.----------64

FIG. 6.11 (a) Proton and (b) neutron fluence after 10 Ahr of irradiation in the central specimen rods, Beam 2, incident proton energy, 570 MeV.----------66

FIG. 6.12 (a)Proton and (b)neutron differential flux spectra at the centers of specimen rods for Beam 2.----------68

FIG. 6.13 (a) Proton and (b) neutron fluence after 10 Ahr of irradiation in the entrance windows Beam 2, incident proton energy, 570 MeV.-----70

FIG. 6.14 Interfaces of the cross section calculation program: “XScal”.----------72

FIG. 6.15 Neutron cross sections for displacement (a), helium (b) and hydrogen (c) production of Al6061, SS316, 9Cr1Mo, and Zirc-4.----------76

FIG. 6.16 Proton cross sections for displacement (a), helium (b) and hydrogen (c) production of Al6061, SS316, 9Cr1Mo, and Zirc-4.----------77

FIG. 17 Displacement, helium and hydrogen production in the entrance windows by Beam2 after 10 Ah exposure.----------79

FIG. 6.18 Displacement production on the walls of the rod-container box and the double layered tube in YZ planes after 10 Ah irradiation by Beam 2 (Z=0 is where the double layered tubes mate the entrance

windows, Z=18 cm is the 15th layer of rods).----------80

FIG. 6.19. Cumulative displacement production in aluminum due to neutron flux at the inner entrance window after 10 Ah exposure.---------82

FIG. 6.20 Displacement, helium, and hydrogen productions at SS316 rods, Beam 2.----------83

FIG. 9.21. Cumulative displacement production in SS316 at the center segment of Rod 7 after 10 Ah exposure.----------85

FIG. 7.1 The flow charts for procedures of Methods 1 and 2.----------90

FIG. 7.2 A photo of Target 3 [4].----------91

FIG. 7.3 A Schematic diagram of Target 3.----------97

FIG 7.4. Proton fluxes as a function of distance along Z-axis for Targets 3 and 5.----------99

FIG. 7.5. Neutron fluxes as a function of distance along Z-axis for Targets 3 and 5.----------100

FIG. 7.6. Cumulative neutron flux for the outer entrance windows at SINQ Targets 3 and 5 and at SNS.----------101

FIG. 7.7 Tensile properties of Al5052 after irradiation (after [68]).----------103

FIG. 7.8. Transmutation Product Concentration Per 10 Ahr vs Product Element in Target 5, STIP III.----------105

FIG. A.1 Displacement, helium, and hydrogen productions at Al6061 rods, Beam 2.----------121

FIG. A.2 Displacement, helium, and hydrogen productions at 9Cr-1Mo rods, Beam 2.----------122

FIG. A.3 Displacement, helium, and hydrogen productions at Zirc-4 rods, Beam 2.----------123

Chapter 1

Introduction

The neutron, through neutron scattering, is considered the perfect candidate to provide researchers and scientists a wealth of information about the position and the movement of atoms inside the structure of materials. Such capacity makes neutron sources to be in a surging demand from many disciplines, such as physics, chemistry, biology and material science [1]. One of the methods that are capable to get high neutron production is through spallation reactions which usually occur under the bombardment of protons with energies higher than about 20 MeV on a heavy metal target. SINQ [1] spallation neutron source was built at Paul Scherrer Institute (PSI), Villigen, Switzerland, in order to provide a new source of neutrons. "It is a continuous source - the first of its kind in the world - with a flux of about 10^{14} n /cm^2s." [2].

The SINQ Target Irradiation Program (STIP) [3] is an international collaboration among many well known laboratories and research agencies. It includes a series of irradiation experiments, of which the first one (STIP I) was performed between June 1998 and December 1999 with a maximum dose of about 12.5 dpa (displacement per atom). The main goal of the STIP program is to study the microstructures and mechanical properties of structural materials in spallation proton and neutron spectra. It also investigates the liquid metal corrosion in an environment where the heavy metal target is liquid [4].

Although radiation effects on material properties have been studied in detail in a fission environment for a long time with a great deal of success, a spallation environment imposes new challenges to materials development due to the characteristics of high energy nuclear interactions, which reveal much higher primary knock-on atom (PKA) energies, significantly larger gas productions, and many more points defects. The mechanisms of radiation damage to the materials in a fission environment could not exactly explain the significant degradation of materials after receiving same irradiation dose in a spallation spectrum [5]. Hence, a further investigation into this field for spallation materials is needed to meet new challenges in materials development. The radiation effects of concern in a spallation environment are mainly hardening and embrittlement, in which the productions of displacement, helium and hydrogen play an important role.

The work of the dissertation mainly focuses on the radiation damage to the specimens and structural materials at SINQ Targets 3 and 5 used in STIPs I and III, respectively, with emphasis on the latter. The spallation materials are zirconium for Target 3 and lead for Target 5. Our work investigated radiation damage productions (displacement, helium and hydrogen productions) at the entrance windows and the specimen rods. The calculation results are instructive to further experimental analysis for exploring the mechanisms of radiation damage due to a spallation proton and neutron spectrum. The errors of the calculations were analyzed and part of the calculation results were further examined by experimental data. A new and second method of calculation was brought up and the results from the two methods are compared and examined. In addition to the radiation damage calculations, one aspect of the spallation reaction physics was studied for the neutron production capacities of

materials. Further more, the other transmutation products contributed to the radiation-induced damage on the materials were investigated.

The dissertation work is expressed in six main chapters:

Chapter 2: Briefly, Chapter 2 introduces the process of spallation reactions, radiation effects on the materials mainly concerned in a spallation environment, and the models and methods for performing radiation damage calculations.

Chapter 3: MCNPX is the main Monte Carlo simulation tool used in the dissertation work, and therefore the main features and functionalities of MCNPX are introduced in this chapter. The physics models inside MCNPX for the Monte Carlo calculations at the intermediate energy range are explained as well.

Chapter 4: The background for the construction of SINQ is introduced, followed by a brief description of the SINQ facility configuration and SINQ Target Irradiation Program (STIP).

Chapter 5: The neutron production capacity of the spallation target material under different bombarding proton energies is explored in this chapter. An "infinite" target is used to eliminate the geometry size effect. The results reveal the upper limit of the "threshold" of the material in neutron production above which the neutron yield per incident proton is proportional to the incident proton energy. Also the results reveal the insensitivity of neutron yield to atomic number or atomic mass of the target material in certain atomic number or atomic mass ranges.

Chapter 6: The calculations of radiation damage to materials at the Target 5 are fully described here. The geometry modeling of the target is introduced in detail, followed by the description of two incident proton beam profiles. Although the calculations are done for both beam profiles, only the results of Beam 2, a truncated double-Gaussian profile, are presented in the chapter for the flux analysis and

radiation damage product analysis. For calculating the radiation damage products, the cross sections for the productions of displacement, helium and hydrogen are developed for four materials: Al6061, SS316, 9Cr-1Mo and Zirc-4.

Chapter 7: As an extension of Chapter 6, this chapter examines the calculation results by using another calculation method and compares the results to the experimental data. The error due to the cross sections is analyzed. The calculation results for Targets 3 and 5 are compared and analyzed. Other mechanisms of radiation damage to the material, like other transmutation products, are studied as well.

The dissertation work is finally summarized following the above chapters, in which conclusions and suggestions for future work are made.

Chapter 2

Radiation damage physics and calculation methods

2.1 Spallation Reactions

Spallation reactions occur in a high energy range (> 20 MeV), in which the De Broglie wavelength of the incident particle is so short compared to the nuclear radius that it is able to interact with individual nucleons inside the nucleus. The outcome of the interaction is that nucleons are "chipped away or spalled from the nucleus" [6], which explains the use of the term "spallation". The spallation process is generally described in a two-stage model: (1) intranuclear cascade and (2) evaporation and/or fission, originally due to Serber [7]. As illustrated by FIG. 2.1, in the intranuclear cascade stage the incident particle collides with a single nucleon which, in turn, may hit another nucleon inside the nucleus and forms a cascade. The energetic cascaded particles are able to escape from the nucleus. If the target is thick enough, the emitted particles may trigger cascades in other nucleus, resulting in a chain of secondary interactions, called an internuclear cascade. In modeling the interaction, the nucleons are treated as a cold, free gas within a potential describing the nuclear density as a function of radius, and the Fermi motion of the nucleons is also taken into account [8]. Following an intranuclear cascade the nucleus is left in an excited state, which may evolve into an intermediate stage of pre-

equilibrium by emitting a neutron, proton, deuteron, triton, ^{3}He or alpha particle to reach an equilibrated excitation number. The remaining excitation energy is de-excited in the second stage where either evaporation or high energy fission or both occur. The residual excitation energy falls below the nucleon binding energy of several MeV after the second stage, and is finally removed by gamma emissions. In evaporation, the residual energy is dissipated by emitting a neutron, proton, deuteron, triton, ^{3}He and alpha particle isotropically. As an alternative, high energy fission may take place with a probability proportional to Z^2/A (Z is the atomic number, A is the atomic mass) [9]. Fission due to high energy particles is notably different from thermal neutron fission in its mass-yield spectrum where a single broad curve centered near one-half of the target mass number replaces the familiar double-humped curve in thermal neutron fission [6].

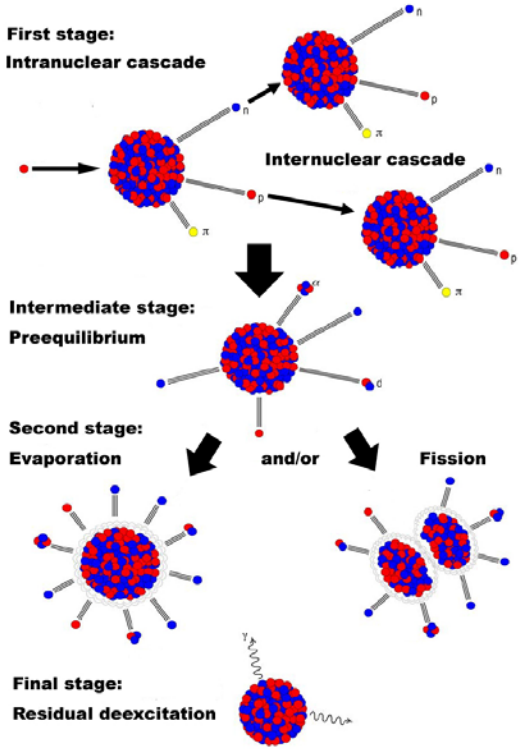

FIG. 2.1 Schematic diagram of the spallation process (an improved graph from Reference [8]).

2.2 Radiation Effects

Radiation effects on material properties have been studied in detail for a long time. A great deal of mechanisms of radiation damage to the materials are revealed and well explained [10]. The corresponding means to prevent or mitigate such effects are also learned. However, a spallation environment imposes new challenges to the material development due to the characteristics of high energy nuclear interactions. A brief review of mechanisms of irradiation effects on mechanical properties is presented in [11], with its emphasis on the effects under a spallation spectrum.

2.2.1 Swelling

A primary effect of concern in the physical changes of materials under irradiation is swelling, a volume change of materials due to voids formed by the aggregation of irradiation produced vacancies. Although vacancies and interstitials are created in equal numbers, interstitials are highly lost to the dislocations and other point defect sinks developed with irradiation dose. The excessive vacancies supersaturate and become sufficiently mobile around temperatures, 0.3 T_m (melt point temperature in K) for FCC (Face Centered Cubic) metals and 0.2 T_m for BCC (Body Centered Cubic) metals, and precipitate to form voids. At the same time the interstitials form planar defects like dislocation loops. The extent to which swelling may occur is dependent on irradiation rate, material state, and the irradiation temperature. A typical temperature range for the occurrence of swelling is around 0.2-0.3 T_m to 0.5-0.6 T_m. The lower limit corresponds to the onset of vacancy mobility which is determined by the irradiation temperature,

while the upper limit depends on the rate of irradiation, the increase of which extends the limit upward. Swelling is not a major concern in our work.

2.2.2 Hardening and embrittlement

The major mechanical property changes after irradiation are hardening and embrittlement. Radiation hardening is controlled by the radiation-induced obstacles to dislocation motion, including dislocation loops, stacking fault tetrahedra, voids, precipitates and others. FIG. 2.2 [5] shows stress-strain curves for 316L stainless steel specimens before and after irradiation at the LANSCE 800 MeV proton accelerator. The specimens received doses up to 9.3 dpa at a temperature of 50 C for both irradiation and test. As illustrated in the figure, the yield stress of the specimen increases with increasing irradiation dose. However, it also undergoes plastic instability with a decrease in strain-to-necking. At a dose of 9.3 dpa, the yield stress of 316L increases 300% from around 300 MPa before irradiation to 900 MPa, but it fractures at a strain below 10% compared to the 50% strain-to-necking before irradiation.

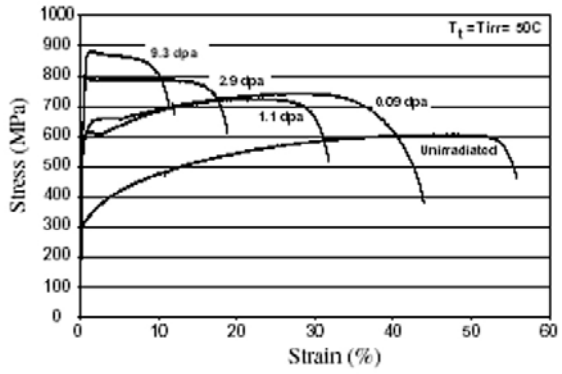

FIG. 2.2 Stress-strain curves for annealed 316L stainless steel after irradiation in the LANSCE irradiation facility [5].

Besides radiation hardening, there are other ways leading to the embrittlement of materials after irradiation. One of them closely related to the spallation spectrum is helium and hydrogen gas production. Helium is a transmutation product through (n, α) reactions. Since it is insoluble in most materials, helium can aid vacancy cluster nucleation and aggregation to form gas-filled voids at a low gas pressure or bubbles at a high gas pressure. The formation of voids and bubbles contributes to the swelling, as mentioned above. The bubbles can become concentrated at the grain boundaries, decreasing cohesion between the grains and provoking the occurrence of grain-boundary fracture, which results in a decrease of tensile and creep ductility. Larger amounts of hydrogen may be produced in spallation environments, but the high diffusivity of hydrogen especially at a high temperature make the problem not so serious as that of helium. However, at a low irradiation temperature the excessive hydrogen may mix with helium, or promote the form of hydrides, the comprehensive effects of which leads to the embrittlement of the metals. In some situations where helium production is low and is believed to be harmless to the material, hydrogen is considered to make a main contribution to the brittleness of the materials [12]. The effects of irradiation-produced hydrogen on the mechanical properties at a low temperature are still under discussion and need further work [13]. FIG. 2.3 [10] shows an SEM micrograph of a T91 small punch specimen after an irradiation dose of 9.4 dpa in STIP (SINQ Target Irradiation Program) I. It clearly shows the bubbles formed by the irradiation produced helium and hydrogen. At this irradiation dose, the gas production is calculated as 720 appm helium and 3880 appm hydrogen. In addition to helium and hydrogen, other transmutation products, e.g.

Si, in the proton irradiation of aluminum, become impurities in the irradiated target and may have complicated effects on the material.

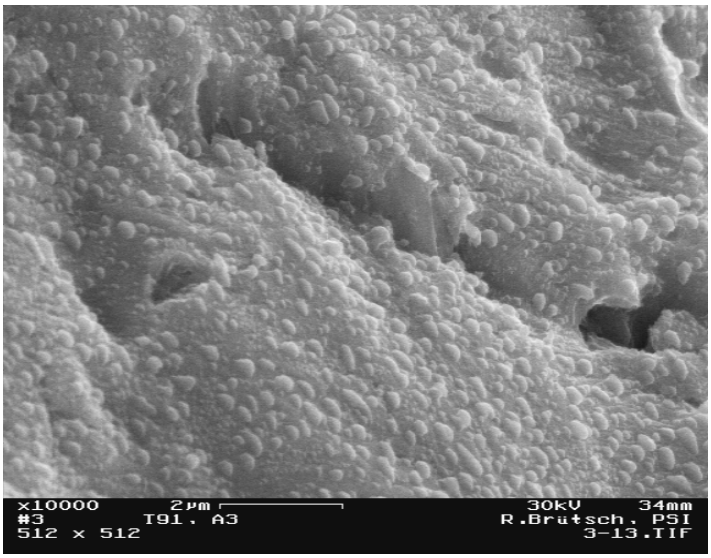

FIG. 2.3 SEM Micrograph of T91 specimen after an irradiation dose of 9.4 dpa [14].

Another type of radiation embrittlement prevails in the BCC metals, which exhibit a ductile-brittle transition temperature (DBTT). A metal is considered to be ductile at a temperature above DBTT and brittle below it. FIG. 2.4 [15] shows the dose dependence curve for the $DBTT_{SP}$ (small punch DBTT) and the USE_{SP} (small punch upper shelf energy) of irradiated T91 steel specimens. As the irradiation dose goes from zero to 9.4 dpa, the DBTT of T91 increases rapidly from -153 C to -35 C. At the same time the USE_{SP} decreases gradually.

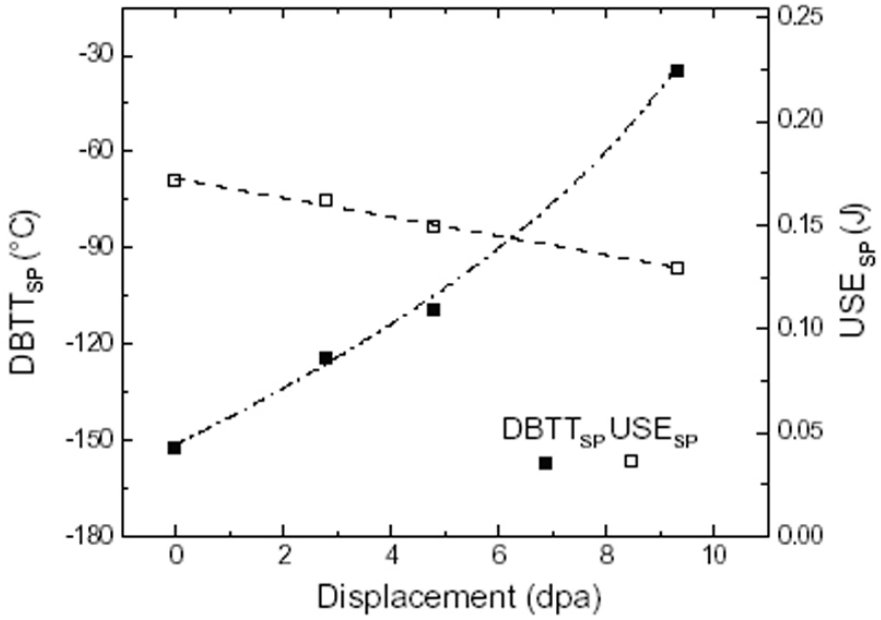

FIG. 2.4 Dose dependence curves for the DBTT$_{SP}$ and USE$_{SP}$ of T91 steel [15].

2.2.3 Other effects

Other radiation effects like irradiation creep, fatigue, and crack growth are also concerns for materials under irradiation in a spallation spectrum. Due to the point defects induced by the irradiation, irradiation creep is a marked process at even low temperatures [11] because of the absorption of point defects along stressed directions. Previous work on fatigue is presented in [16-20], which clearly reveals reduced fatigue lives after irradiation. As a liquid metal spallation target proposed for SNS (Spallation Neutron Source), recent works [21-23] mainly focus on the fatigue behavior in liquid metals like LBE (Lead-Bismuth Eutectic) and mercury. The investigations reveal that the presence of mercury or LBE does not have a significant effects on the endure limit of 316 stainless steel.

In a summary of radiation effects, the significant physical difference between effects in a spallation spectrum and a fission spectrum has to be emphasized, that is, in the spallation environment there are much higher primary knock-on atom (PKA) energies, significantly larger gas productions, and many more points defects. The mechanisms of radiation damage to the materials are well studied originally in a fission spectrum. Most of them are appropriate to apply to the materials in a spallation spectrum. However, they could not exactly explain the significant degrade of materials after receiving same irradiation dose in a spallation spectrum than in a fission spectrum. Hence, a further investigation into this field for spallation materials is needed to meet new challenges in materials development.

2.3 Radiation damage calculations

As discussed above, the essential radiation damage due to a spallation spectrum stems from the displacement cascade of lattice atoms and the significant gas production of helium and hydrogen. They can further produce excessive point defects and a large amount of bubbles, respectively, which are the primary agents for the cause of radiation hardening and embrittlement. Thus, it makes the calculation of displacement, helium and hydrogen production an essential task in the estimation of radiation damage. In addition, it can assist experimental data analysis for exploring the mechanisms of radiation damage due to a spallation spectrum. A part of this dissertation is devoted to this task. Therefore, before proceeding to the main body of calculation results, an attempt is made to better explain the underlying irradiation physics.

2.3.1 Calculation of displacements

To dislodge it from its normal place in the lattice a critical energy is required to transfer to the struck atom, which is known as the threshold displacement energy, T_d. TABLE 2.1 [24] shows the recommended values for T_d in displacement calculations, though some of them may be corrected for newer values during recent investigations [25], like T_d for Al is recommended as 27 eV instead of 25 eV. The displacement threshold energy is so small that an incident neutron with a few MeV kinetic energy may not only displace the primary struck atom but also produce a lot of secondary displacements which, in turn, may result in a displacement cascade, which is evident from the calculation of the maximum energy transferred to the struck atom [26]. The classical theory of the maximum transferred energy in an elastic head-on collision is expressed in Eq. (2.1),

$$T_{\max} = \frac{4mM}{(m+M)^2} E \qquad (2.1)$$

where m and E are the mass and kinetic energy of the incident particle, and M is the mass of the target material. If the kinetic energy of the incident particle is greater than its rest energy (mass), a relativistic form, (2.2), is used instead of (2.1), where c is the speed of the light.

$$T_{\max} = \frac{2ME(E+2mc^2)}{(m+M)^2 c^2 + 2ME} \qquad (2.2)$$

For the purpose of T_d measurement, where only a few displacements are desired in a head-on collision, electron irradiation is used for the best performance of the measurement [26].

TABLE 2.1 Recommended values for displacement threshold energy.

Metals	T_d (eV)
Al	25
Ti	30
V	40
Cr	40
Mn	40
Fe	40
Co	40
Ni	40
Cu	30
Zr	40
Nb	60
Mo	60
Ta	90
W	90
Pb	25

Not all the energy transferred to the struck atom contributes to the radiation damage on the material. The energy delivered to electrons inside an atom produces ionization and electronic excitation but has no lasting effects on the material. Only that portion of the transferred energy partitioned to the nuclei will produce secondary displacements and cause point defects. It is called radiation damage energy, T_{dam}. Strictly speaking, T_{dam} is the portion of the energy of the incident atom transferred to the nuclei, which must exceed the energy required to displace an atom from its lattice cite, T_d. At a lower kinetic energy the incident atom delivers most of its energy to the nuclei, while at a higher kinetic energy to the electrons. A simple model was once put forward for the calculation of displacements with an ionization cutoff energy, T_I. An incident atom partitions its kinetic energy to the nuclei only when it falls below T_I, otherwise it transfers all its kinetic energy to the electrons. A more sophisticated model was

developed by Lindhard and co-workers [27] to have a gradual transition of the energy partitioned to from the electrons to the nuclei when a moving atom slows down. T_{dam} is then given by Eqs. (2.3)-(2.6), where T is the transferred energy to the primary struck atom in the unit of ergs, a_0 is the Bohr radius (5.292 x 10^{-9} cm), e is the electronic charge (1.602 x 10^{-19} coulomb, e^2 =1.440 x 10^{-7} eV·cm), and A_1, Z_1, and A_2, Z_2, are the atomic

$$T_{dam} = T[1 + kg(\varepsilon)]^{-1} \tag{2.3}$$

$$k = \xi_e \frac{0.0793(A_1 + A_2)^{3/2} Z_1^{1/2} Z_2^{1/2}}{(Z_1^{2/3} + Z_2^{2/3})^{3/4} A_1^{3/2} A_2^{1/2}}, \quad \xi_e \cong Z_1^{1/6} \tag{2.4}$$

$$\varepsilon = \frac{A_2 T}{(A_1 + A_2)} \frac{a}{Z_1 Z_2 e^2} \tag{2.5}$$

$$a = a_0 (\frac{9\pi^2}{128})^{1/3} (Z_1^{2/3} + Z_2^{2/3})^{-1/2} \tag{2.6}$$

masses and atomic numbers of the incident atom and the target atom respectively. The function g(ε), which was presented graphically by Lindhard and co-workers [27], was later evaluated numerically as given in Eq. (7) due to the work of Robinson and co-workers [28].

$$g(\varepsilon) = \varepsilon + 0.40244\varepsilon^{3/4} + 3.4008\varepsilon^{1/6} \tag{2.7}$$

In a special case of interest when A_1=A_2 and Z_1=Z_2, Eqs. (6) and (7) can be simplified as followings:

$$k = 0.1337 Z_1^{2/3} A_1^{-1/2} \tag{2.8}$$

$$\varepsilon = T/(0.08693 Z_1^{7/3}) \tag{2.9}$$

They are quite useful for a monatomic system where Z_1=Z_2, or for a non-monatomic system where Z_1 and Z_2 are sufficiently close.

For a better description of Eqs (2.3)-(2.7), FIG. 2.5 [24] presents the damage efficiency, $\xi(T)=T_{dam}/T$, as a function of primary recoil energy for several irradiated materials.

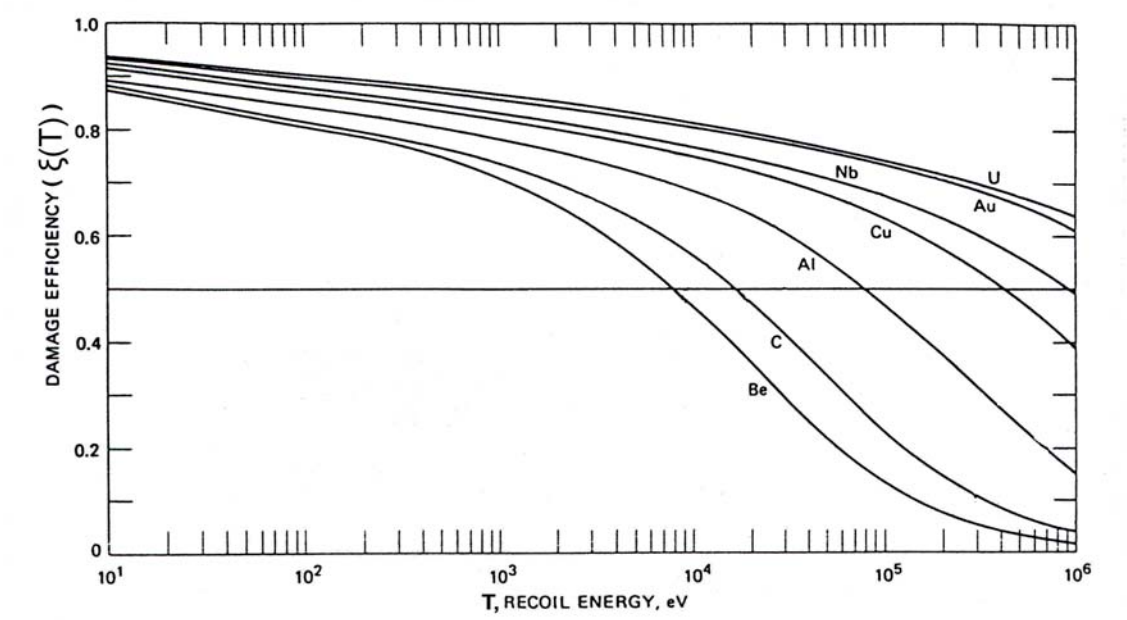

FIG. 2.5 Transferred recoil energy, T dependence curve of damage efficiency ξ(T) (after [28]).

A simplified model to describe the number of displacements due to a damage energy of T_{dam} from a primary struck atom, $\upsilon(T_{dam})$, is developed and recommended by IAEA and USERDA [24]:

$$\upsilon(T)=\begin{cases}0 & T<T_d \\ 1 & T_d \le T<2T_d/\beta \\ \beta T_{dam}/2T_d & T \ge 2T_d/\beta\end{cases} \qquad (2.10)$$

where β usually equals to 0.8 for the compensation of the forward scattering in the displacement cascade, and the factor of 2 in the denominator allows energy loss in subthreshold interactions [26].

Eq. 2.10 is a bridge for the conversion from damage energy to displacement cross section, σ_d, which represents the rate of displacement production per atom per unit flux.

$$\sigma_d = \int_{T_d}^{T_{dam}} \sigma_T'(E,T)\upsilon(T_{dam})dT \qquad (11)$$

In Eq. 2.11 E is the energy of the projectile and σ_T'(E,T) is the differential scattering cross section . Therefore σ_T'(E,T)dT is the cross section for transferring energy between T and T+dT to the struck atom by a projectile of energy E. Eq. 2.10 in Eq. 2.11 gives:

$$\sigma_d = \frac{\beta}{2T_d}\int_{T_d}^{T_{dam}} \sigma_T'(E,T)T_{dam}dT = \frac{\beta}{2T_d}\sigma_E \qquad (2.12)$$

σ_E is defined as damage-energy cross section [24], representing the rate of damage energy deposited per atom per unit flux. The displacement production rate per atom, K, is then given by:

$$K = \int_0^{\infty} \sigma_d(E)\phi(E)'dE \qquad (2.13)$$

where $\phi(E)'$ is the differential incident flux.

The above theories are widely adopted for the displacement calculations and are proved to be useful. However, it overestimates the experimentally measured amount of damage since radiation damage involves complicated and subtle developments in collision cascades, crystal effects, the structure of damaged regions, cascade-induced microstructure, and etc [29].

For a sufficiently thin target with the incident flux uniformly over the entire volume, a more simplified model is used for the calculation of displacement cross sections taking advantage of average damage energy over time t, $<T_{dam}>$. Suppose a cylindrical target of cross-sectional area A and thickness x under the irradiation of totally n atoms over t, the number of target atoms, N, is:

$$N = N_v A x \tag{2.14}$$

where N_v is atomic density of the target material, and the incident flux is:

$$\varphi = n / At \tag{2.15}$$

The rate of damage energy transferred per atom, K_E, is given by:

$$K_E = < T_{dam} > / Nt = < T_{dam} > / N_v Axt \tag{2.16}$$

Given the definition of σ_E in Eq. (12) and Eqs. (15) and (16), σ_E is expressed as:

$$\sigma_E = \frac{K_E}{\varphi} = \frac{< T_{dam} > / n}{N_v x} \tag{2.17}$$

By Eq. (10) we have

$$\sigma_d = \frac{\beta}{2T_d} \frac{< T_{dam} > / n}{N_v x} \tag{2.18}$$

Eq. (18) is generally used in the calculation of displacement cross sections not available from the literature. A Monte Carlo code, in the case of our work MCNPX, is usually used to assist the calculation of $<T_{dam}>$.

2.3.2 Calculation of gas productions

Helium production is largely due to (n, α) and (p, α) reactions. One of reactions producing helium in the bombarding of thermal neutron on the 316 stainless steel is separated in two steps.

$$Ni^{58} + n^1 \rightarrow Ni^{59} + \gamma$$

$$Ni^{59} + n^1 \rightarrow Fe^{56} + He^4$$

Hydrogen is mainly produced by the energetic neutrons through (n, p) reactions. Although specific gas calculation expressions are given for specific reactions, a more general used method is to take advantage of a Monte Carlo code, like MCNPX, which will tally the gas production based on the unit incident atom. If a thin target model as mentioned in the calculation of displacement cross sections is used, the gas production cross sections are given by Eq. 2.19:

$$\sigma_{gas} = \frac{n/n_0}{N_v x} \qquad (2.19)$$

where σ_{gas} is either the production cross section of helium, σ_{He}, or hydrogen, σ_H, n/n_o is the number of gas atoms produced per incident particle, N_v is the atomic density of the target material, and x is the thick ness of the target.

The diffusivity of the gas may put some difficulty in the gas production calculations, especially in the case of hydrogen which is highly diffusive. In the post calculation of MCNPX, HTAPE has two options to tally the productions of helium or hydrogen. IOPT=3 tallies gases where they are generated, while IOPT=4 tallies those when they come to rest. In a very thin target some of the gas production may leave the surface, which may lead the estimation to a lower value. Therefore a careful selection of the target thickness has to be made for better estimation according to the real target.

Chapter 3

MCNPX

3.1 Introduction of MCNPX

MCNPX [8] is a Monte Carlo particle transport code merging two of its preceding codes, MCNP [30], a Monte Carlo code tracking lower energy particles (< 20 MeV for neutrons) and LAHET (Los Alamos High Energy Transport Code) [31], tracking higher energy particles. MCNPX was developed to provide a better simulation tool for the design of the spallation target, surrounding lead blanket and associated shielding in the support of the Accelerator Production of Tritium Project (APT). MCNPX program began in 1994, and was intended to extend the existing functionalities of MCNP to be able to track all particles at all energies, to improve physics simulation models, to extend or develop neutron, proton and photonuclear libraries up to 150 MeV, and to introduce new variance reduction and data analysis techniques. In a short period, MCNPX has rapidly developed into a significant Monte Carlo simulation tool for various applications in the low-energy and high-energy transport fields:

(1) accelerator spallation targets design, accelerator isotope production and destruction programs (i.e. ATW), and accelerator-driven energy sources research;

(2) proton and neutron therapy in medical physics, neutron and proton radiography in accelerator-based imaging technology;

(3) Shielding design, cosmic-ray radiation backgrounds investigation for high altitude aircraft and spacecraft, charged-particle propulsion for space flight;

(4) high-energy dosimetry and neutron detection, detection technology using charged particles

(5) design of neutrino experiments, comparison of physics-based and table-based data. charged-particle tracking in plasmas;

(6) single-event upset in semiconductors, from cosmic rays in spacecraft or from the neutron component on the earth's surface.

3.2 New characteristics of MCNPX

The primary characteristic of MCNPX distinguished from MCNP, as stated in its development goal [8], is that it can track all basic particles at all energies. TABLE 3.1 lists 34 particles within the tracking capability of MCNPX in current version 2.4.0, though not all of them are fully transported due to their extreme short halflives.

TABLE 3.1 Particles traceable in MCNPX, "symbol" is the symbol used in MCNPX to designate the particles, "IPT" is the index of particle tracing in MCNPX (after [8]).

Particle Name	Symbol	IPT	Particle Name	Symbol	IPT
neutron (n) / anti-neutron (n)	n	1	Photon (γ)	p	2
electron (e^-) / positron (e^+)	e	3	muon$^-$ (μ^-) / anti-muon$^-$ (μ^+)	|	4
tau$^-$ (τ^-)	*	5	electron neutrino (ν_e)/ anti-electron neutrino	u	6
muon neutrino (ν_m)	v	7	tau neutrino (ν_t)	w	8
proton (p) / anti-proton (p)	h	9	lambda^0 (Λ^0)	L	10
sigma$^+$ (Σ^+)	+	11	sigma$^-$ (Σ^-)	-	12
cascade^0 (Ξ^0)	x	13	cascade$^-$ (Ξ^-)	y	14
omega$^-$ (Ω^-)	o	15	lambda$_c^+$ (Λ_c)	c	16
cascade$_c^+$ (Ξ_c^+)	!	17	cascade$_c^0$ (Ξ_c^0)	?	18
Lambda$_b^0$ (Λ_b^0)	r	19	pion$^+$ (π^+) \ pion$^-$ (π^-)	\	20
neutral pion (π^0)	z	21	kaon$^+$ (K^+) \ kaon$^-$ (K^-)	k	22
K_0 short	%	23	K_0 long	^	24
D^+	g	25	D^0	d	26
D_S^+	f	27	B^+	j	28
B^0	b	29	B_S^+	q	30
deuteron	D	31	triton	t	32
helium-3	s	33	Helium-4 (α)	a	34

The other two major progresses in MCNPX lie in the visualization capabilities: the geometry-independent mesh tallies and the radiography simulation. The implementation of a mesh tally requires the user to define arbitrary rectangular, cylindrical, or spherical meshes which are independent from the cells defining the MCNPX geometry. In such a way, the mesh tally can tally and present graphically such properties as flux, dose and energy deposition over a continuous space volume without complicating the geometry specification and the particle transportation through the geometry [32]. The presentation of mesh tally results can be found in figures in Chapter X. As an improvement from MCNP point detector tally, the radiography tally adds image capability into MCNPX. There are two types of image recording capabilities in the radiography tally: the pinhole image projection and the transmitted image projection. In the pinhole projection, it is necessary to specify a collimating pinhole at a spatial location with an optional radius, and a film plane where the image is projected via an arbitrary rectangular grid. In the transmitted project, only a film plane is needed for recording the transmitted image. The current version of MCNPX does not support the image capability of charges particles, nor neutrons at energies higher than the tabulated nuclear data tables. However, the future version of the code may address this problem [32]. FIG. 3.1 [32] shows a part of a simulation for a very low energy neutron radiography experiment done by group P-23 at Los Alamos National Laboratory. The sample model was a beryllium block with both a carbon bolt and a steel bolt uniformly irradiated by parallel beams of neutrons at an energy of 7.7×10^{-3} eV. As showed in the figure, the image of the beryllium block and the carbon bolt is clear while only a part of the steel bolt can be seen at the top.

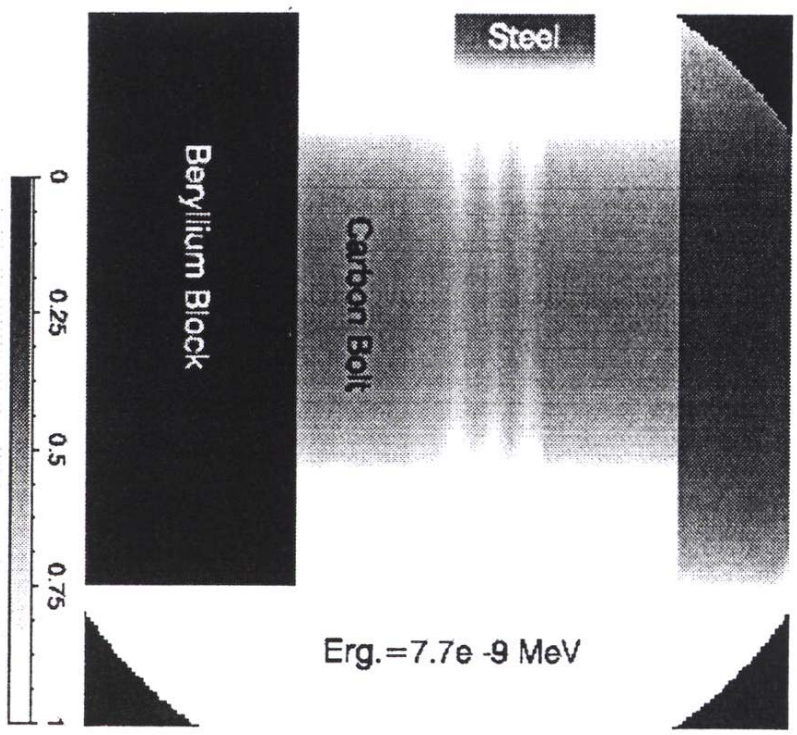

FIG. 3.1 Part of an experimental simulation using the radiography tally [32].

3.3 Physics models in MCNPX

As particles undergo different phases of reactions at different energies during transportation, MCNPX uses three sets of physics models or data in its simulations. For energies below the tabulated nuclear data table limit (20 MeV for most isotopes, 150 MeV for isotopes in LA 150), the tabulated nuclear data are directly used since they are carefully evaluated for the consideration of nuclear structure effects. Most of the interaction physics in this range can be inherited from MCNP with some improvements. Above the table limit up to a few GeV, it is the region of intranuclear cascade (INC) /pre-equilibrium/evaporation for spallation. For energies higher than the natural limitations of intranuclear cascade where quantum effects are considered, MCNPX contains an early version of FLUKA [33-34] to handle high-energy interactions.

The interaction physics in the second energy range, i.e. the intermediate interaction physics, is commonly initialized by intranuclear cascades and is widely interested in the accelerator applications as well as our work. MCNPX contains three physics models for the simulation in this region, two of them, BERTINI [35-36] and ISABEL models [37-40] are inherited from LAHET while the CEM model [39] is newly included in the code. The main frame of physics models in the intermediate energy range is explained already in the spallation reactions in Chapter 2, however those three models deal differently with the details of the interaction. A summary of the comparison among three models is briefly reviewed in [8]. BERTINI model is a relatively old model with an energy range from 20-150 MeV to 2.5-3.5 GeV for incident particles like proton, neutron and pions. It has only three nuclear density steps. Instead, ISABEL model represents nuclear density up to sixteen steps and has the capability of treating nucleus-nucleus interactions as well as particle-nucleus interactions. However, it only allows projectiles with atomic mass less than 4 with no antiproton annihilation. The upper energy limit of the ISABEL model is only 1 GeV, and the running time is 5-10 times longer than for the BERTINI model. The CEM model is suitable for incident particle energy up to 5 GeV. But it can only treat the interactions with nuclei heavier than carbon. Also it takes longer time. In the adaptation of multistage pre-equilibrium models (MPM) to the ISABEL INC model, it is able to determine explicitly the particle-hole state of the residual nucleus. However the interface between the BERTINI INC model and the MPM is rather a rough approximation for initial evaluation.

Fermi-breakup model [40] is used in all three physics models for the disintegration of light nuclei (A, atomic mass, less than 17) instead of the evaporation model. It models a sequence of simultaneous breakups of the excited nucleus into

two or more products until each of products reaches a stable state. For heavier nuclei, an evaporation model is used, in which the energy is dissipated by the emission of neutron, proton, deuteron, triton, ^{3}He, and alpha particles. The Dresner model [41] is used in BERTINI and ISABEL for evaporation, but the CEM 97 model is used in CEM. For the high-energy fission, there are two models: the ORNL (Oak Ridge National Laboratory) model [42] and the RAL (Rutherford Appleton Laboratory) model [43]. The RAL model deals with both actinides and subactinides in fission but the ORNL model only covers actinides.

Chapter 4

SINQ and STIP

4.1 SINQ development

4.1.1 Need for neutron sources

As a fundamental particle that builds up the world of matter, neutron sources are in a surging demand from many disciplines, such as physics, chemistry, biology and materials research [1]. The unique characteristic of the neutron makes it capable to provide researchers and scientists a wealth of information about the position and the movement of atoms inside the structure of materials. The way to glean such details about the nature of the materials is through neutron scattering or diffraction, in which the energies, angles, and patterns of the scattered neutrons are measured. Applications of neutron scattering extend widely from the proteins of medicine research, through the superconductor study, to the non-destructive measurement of materials. A few examples of utilizing neutron scattering may be illustrated as below.

Neutrons provide an extremely sensitive tool in studying hydrogen atoms. The use of neutron scattering can therefore precisely locate the position of hydrogen atoms, which provides a better understanding of the molecular structure in the design of new therapeutic drugs. The locating of hydrogen in water helps to detect moisture in fighter jet wings, which reveals the microscopic crack and early corrosion [44]. Neutrons can also locate other light atoms among heavy atoms. For example, scientists use neutron scattering to determine the critical positions of light oxygen

atoms in yttrium-barium-copper oxide (YBCO), a promising high-temperature, superconducting ceramic [1,2,44]. Neutrons have magnetic moments which enable neutrons to be polarized. The polarized neutron beams can be used to probe the properties of magnetic materials [1,2,44]. Thermal neutrons, whose energies are close to that of atoms in motion, can be utilized to track molecular vibrations and movements of atoms during catalytic reactions [44].

In a word, neutrons are so essential to the science research that new methods for producing large quantities of neutrons are desired.

4.1.2 SINQ introduction

One of the methods that are capable to get high neutron yield is through spallation reactions. SINQ (Swiss Spallation Neutron Source in German) was built at Paul Scherrer Institute(PSI), Switzerland, in order to meet the demand for neutrons. "It is a continuous source - the first of its kind in the world - with a flux of about 10^{14} n /cm^2s. " [1]. The energy of the proton beam out of the end of the accelerator system is 590 MeV at a current up to 1.8 mA [45]. The proton beam is first pre-accelerated by by a Cockroft-Walten preaccelerator to 870 keV, and is then further accelerated by two isochronous cyclotrons to 590 MeV. After passing through two pion production targets (Targets M and E) where the beam energy drops to 570 MeV, the proton beam is deflected by magnetic fields and delivered to the spallation target through a sloping drift tube. Target E is a 4 cm long graphite block and is able to capture 70% of the beam flux. Hence, the maximum current of the beam hitting the spallation target is reduced to 1.3 mA. FIG. 4.1 [1] shows the model of SINQ in which the proton beam is directed upward to the bottom of the target from underneath through beam guides.



FIG. 4.1 Model of SINQ [1].

The spallation target is located at the center of a moderator tank. Inside the moderator tank, the target is enclosed by a double-walled safety hull which itself is surrounded by layers of heavy water, light water and shielding materials. Heavy water also flows filling the gap between the target and the safety hull. It serves as a moderator for producing cold neutrons. The details of the target are revealed in Chapter 5. FIG. 4.2 [1] shows the shape of the moderator tank right before installation. The whole target platform is hung from the top of the shielding block and is exchangeable by a shielded exchange flask if the top shielding block is removed. FIG. 4.3 [1] is an overview of the SINQ before the construction was completed. It shows the massive concrete block on the top of the building protecting

against exceedingly fast neutrons and protons. Thermal neutrons are extracted by the beam tubes through the “steel thimble-shaped penetrations of the moderator tank” [1]. Cold neutrons are transported through neutron guides to the experimental facilities.



FIG. 4.2 The moderator tank of SINQ before installation [1].



FIG. 4.3 An overview of the SINQ [1].

4.2 SINQ target irradiation program (STIP)

SINQ target irradiation program (STIP) started in PSI in 1996 under the collaboration among Forschungszentrum Jülich (FZJ), Oak Ridge National Laboratory (ORNL), Commissariat à l'Energie Atomique Centre d'Etudes de Saclay (CEA), Japanese Atomic Energy Research Institute (JAERI) and Los Alamos National Laboratory (LANL) [4]. One main purpose of the program is to study the microstructures and mechanical properties of structural materials in a spallation spectrum. The detailed focuses [4] are:

(1) radiation damage on the different types of alloys of the same base;

(2) radiation effects on welded materials;

(3) examination of the advanced low-activation martensitic/ferritic steels developed for fusion reactors.

The program is planned in four phases. The time schedule of the four phases is listed in TABLE 4.1, as well as target materials and irradiation doses [3]. STIP I received a total of 6.8 Ahr of proton charge and STIP II received 10.03 Ahr of proton charge. Most of the specimens irradiated in the targets are stainless steels, like 316L, T91, HT-9, F82H, and Eurofer 97. Besides investigation of radiation damage to the structural materials under the bombardment of high energy protons and the resulting spallation neutrons, STIP also examines the liquid metal corrosion in an environment of liquid target material, as proposed for the SNS (Spallation Neutron Source) [46]. This is reflected in the configuration of specimens and the choice of target spallation material in different STIP phases.

TABLE 4.1 Plan of the SINQ target irradiation program, PIE is the post irradiation examination, the doses are estimated maximum values inside the target.

	Target number	Irradiation time	PIE	Spallation material	Temp. (C)	Displ. (dpa)	Helium (appm)
STIP I	3	06/98~12/99	2000~2002	Zr	80 ~ 410	12.5	900
STIP II	4	03/00~12/01	2003~2004	Pb	80 ~ 480	23	1600
STIP III	5	02/02~12/03	2005~2006	Pb	80 ~ 550	25	1800
STIP IV	6	03/04~12/04	2006	Pb	80 ~ 600	15	1000

Our work mainly focuses on STIP III, and some parts of STIP I.

Chapter 5

Neutron yields

5.1 Introduction of calculations

As stated in the previous chapter, neutron production is a vital concern in a spallation system. The ultimate goal of the system design is to produce as many neutrons as ideally possible. However, in the practical engineering neutron production is a much more complicated matter. It has to be a balance between the technical constraints imposed by the performance requirements from other concerns in the system and their corresponding economic costs. Therefore, a more practical question brought up to the system design would be what is the optimized neutron yield? It is still a tough question in the comprehensive view of the system, but in the part of nuclear and particle physics the question may be confined to a choice of the incident proton energy, the target material and the target geometry. The calculations of neutron yields in this chapter was initiated by the comparison of the neutron yields between STIP I and STIP III. However, further exploring of this matter extended itself to a more general purpose for illustrating neutron yields due to different target materials and incident proton energy, and their underlying physics.

MCNPX, a Monte Carlo code, is used in our calculations. The versatility of the code may provide many methods in calculating neutron yields. A simple method in dealing with this problem is an indirect way taking advantage of the output file of MCNPX. FIG. 5.1 is a part of MCNPX output file showing only the summary of

neutron creation and neutron loss. The net neutron production would be the sum of the difference of weights between neutron creation and neutron loss in all possible reaction channels, like nuclear interaction, (n, xn) reaction, and fission. For example, the total neutron production (n/p, neutrons per incident proton) in the problem summary of FIG. 5.1 can be expressed as

$$n/p = A - a + B - b.$$

A more simple method is to sum the weights of the escaped and the captured as

$$n/p = E + C$$

since all the neutrons produced either leave the target or are absorbed by the target. Although MCNPX does not give the uncertainty of the results, a reasonable estimation [8] of the upper limit of the relative error is $\frac{1}{\sqrt{N}}$, where N is particle number in the simulation.

1problem summary

run terminated when 10000 particle histories were done.

\+ 10/29/02 20:17:00

N/P yield calculations probid = 10/29/02 20:14:54

neutron creation		tracks	weight (per source particle)	energy (per source particle)
source		0	0.	0.
nucl. interaction	A	213380	2.1338E+01	4.6821E+02
particle decay		0	0.	0.
weight window		0	0.	0.
cell importance		0	0.	0.
weight cutoff		0	1.1002E-03	8.0114E-06
energy importance		0	0.	0.
dxtran		0	0.	0.
forced collisions		0	0.	0.
exp. transform		0	0.	0.
upscattering		0	0.	0.
photonuclear		0	0.	0.
(n,xn)	B	80602	8.0559E+00	4.0856E+01
prompt fission		0	0.	0.
delayed fission		0	0.	0.
tabular boundary		2	2.0000E-04	2.9932E-02
tabular sampling		0	0.	0.
total		293984	2.9395E+01	5.0910E+02

neutron loss		tracks	weight (per source particle)	energy (per source particle)
escape	E	263148	2.5472E+01	2.4869E+02
energy cutoff		0	0.	0.
time cutoff		0	0.	0.
weight window		0	0.	0.
cell importance		0	0.	0.
weight cutoff		67	1.4858E-03	8.5660E-06
energy importance		0	0.	0.
dxtran		0	0.	0.
forced collisions		0	0.	0.
exp. transform		0	0.	0.
downscattering		0	0.	2.4852E+01
capture	C	0	8.4693E-01	5.0769E-01
loss to (n,xn)	b	27060	2.7041E+00	1.0051E+02
loss to fission		0	0.	0.
nucl. interaction	a	3707	3.7070E-01	1.3450E+02
particle decay		0	0.	0.
tabular boundary		2	2.0000E-04	2.9932E-02
total		293984	2.9395E+01	5.0910E+02

number of neutrons banked	266924	average time of (shakes)	cutoffs
neutron tracks per source particle	2.9398E+01	escape 9.6708E+00	tco 1.0000E+34
neutron collisions per source particle	9.5017E+01	capture 2.0242E+00	eco 0.0000E+00
total neutron collisions	950175	capture or escape 9.4247E+00	wc1 -5.0000E-01
net multiplication	0.0000E+00 0.0000	any termination 8.4407E+00	wc2 -2.5000E-01

FIG. 5.1 Part of MCNPX output file.

5.2 Results and Discussion

5.2.1 Calculation validity checking

The default intranuclear cascade mode of MCNPX uses the BERTINI model [35-36] which is also the model used in our calculation. A concern over the validity of the model was raised due to neglect of nuclear structure effects in the nonelastic interactions in its modeling [47]. The model is considered in a good agreement with measured data for the differential neutron yields of targets made of heavier elements, such as Pb and W, at incident energies above 100 MeV. But it overestimates the production in the evaporation region for lighter elements in this energy range. For the energies lower than 100 MeV, the estimation is worse for both heavy and light elements [48-49]. However, as mentioned in [47] a conclusion for the differential neutron yields may be not correct for the integral neutron yield. The reason is due to the factor that so many reaction channels are opened up in the spallation reaction energy region (usually greater than 20 MeV) that the discrepancies in the differential spectrum may be cancelled out. Previous work done in [50-51] proved that the BERTINI model can be used for incident energies down to 15 MeV with satisfactory results for the integral neutron yields. The difference is within 20% from the empirical data.

Such potential error in our calculations for the integral neutron yields using BERTINI model may be further eliminated due to the merits of MCNPX. As introduced in Chapter 3, MCNPX incorporates the use of LA 150 which evaluates cross sections up to 150 MeV for the elements of the common used spallation target materials. Most of our calculations used LA 150 for the accuracy. For those elements with no available cross section libraries in LA 150, the regular cross section libraries (upper limit 20 MeV) are used.

The validity of our calculations for the neutron yield may be checked in a comparison with the measured data from Fraser et al. [52]. FIG. 5.2 shows the comparison between. The targets in the experiments of [52] are cylinders, most of which are 10.2 cm in diameter and 61 cm in length. The proton beam impinges at the center of the front surface of the cylindrical target. The materials and geometry size of the targets are marked in FIG. 5.2. The solid lines represent our calculated data, and the black dots represent the measured neutron yield escaping from the targets as given in [52]. As observed in the figure, except the data of uranium target which shows a deviation from the experimental data of 20%, the calculated data of neutron yields from all other targets are in a fine agreement with the experimental data.

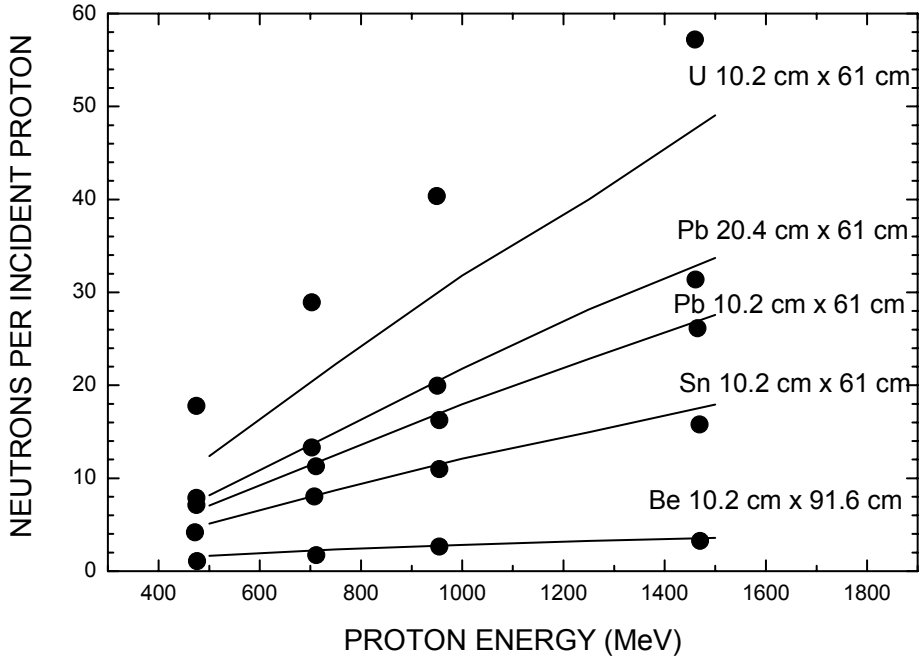

FIG. 5.2 Comparison between calculated neutron productions and measured ones.

5.2.2. Neutron production versus incident proton energy

Neutron yield is a function of incident proton energy, target material and target geometry. However, target geometry varies from system to system. It is

difficult to predict a specific target geometry for a spallation system since requirements from other parts of the system may impose further restrictions. To eliminate the effects of target geometry and to focus on the capacity of the material in neutron production, an "infinite" target is used in the calculations. Precisely, the "infinite" target is defined as a target which is large enough to allow the number of neutrons escaping from any surface of the target to be negligible. In the real calculations, the target is usually a right circular cylinder with 20 m in diameter and 20 m in length. The proton source is a pencil beam at the center axis of the cylinder. It is positioned at 1 to 2 m downstream from the front surface to prevent any significant back scattering.

FIG. 5.3 shows the calculated neutron production per incident proton in the "infinite" targets for commonly used target materials: W, Hg, Pb, LBE, Bi, U, and Zr. Other materials, Pa, Th, Ta, Au, Eu, Sn and Rh, are also calculated for comparison and better understanding. Pa-233, U-238 and Th have higher neutron productions than other materials due to the neutrons contributed by fission reaction. Although at the lower energy the neutron production has a polynomial dependence on the incident proton energy, at the higher energy it almost perfectly linearly depends on the incident proton energy. The relationship between the neutron production and the incident proton energy at higher energy (>400 MeV) can be expressed in a liner equation, $y=a(x-b)$, where x is the incident proton energy, y is the neutrons per proton. The fitting results for a and b are listed in TABLE 5.1. An interesting phenomenon is that all the materials seem to have a similar "threshold" energy, b, around 220 MeV for neutron production. It is not a true threshold since below this energy neutron production is not cut off to zero. However it may represent a level above which the energy of the incident proton partitioned to other uses than producing neutrons is

negligible. If the measured data in FIG. 5.2 are fitted into such a linear expression, a similar "threshold" of 120 MeV is concluded in [53] as "E-120 rule". The apparent threshold may be due to the part of the incident proton energy that goes to the heating of the struck nuclei into excited state and does not later contribute to the production of neutrons. It occurs in intranuclear cascade, the first stage of a spallation reaction. At lower incident energies, the percentage of the energy dissipated in such purpose is large, therefore only a few neutrons are produced and the neutron production is not proportional to the incident proton energy. As the incident proton energy increases, the percentage of the dissipated energy becomes negligible. Most of the energy goes to release nucleons bonded inside the nuclei with certain energies. Hence, a linear dependence of the incident proton energy is observed. When the target size gets larger the threshold gets higher. As observed the threshold increases from 120 MeV in 20 cm x 61 cm targets in [52] to 220 MeV in infinite targets. In a thicker target the internuclear cascade due to secondary interactions prevails and contributes mostly to the neutron production, therefore more energy is consumed in heating the nuclei.

In the analysis, the contribution to the neutron production may be separated into two components: one is from the lower incident energies and the other is from the higher incident energies. FIG. 5.4 shows fitted curves for an infinite target of Pb. There are 3 curves: A, the fitted curve for neutron production at the lower energy portion (< 400 MeV); B, the extension of the fitted curve for neutron production at the higher energy portion (> 400 MeV) with incident proton energy down to the "threshold"; C, the difference of A and B. Curve C is then the lower energy contribution component and Curve B is the higher energy contribution component. As observed in FIG. 5.4, the contribution from the lower incident energy portion increases non-linearly and reaches a peak where the contribution from the higher

energy portion rises. After the peak, the higher energy contribution dominates and the lower energy contribution drops.

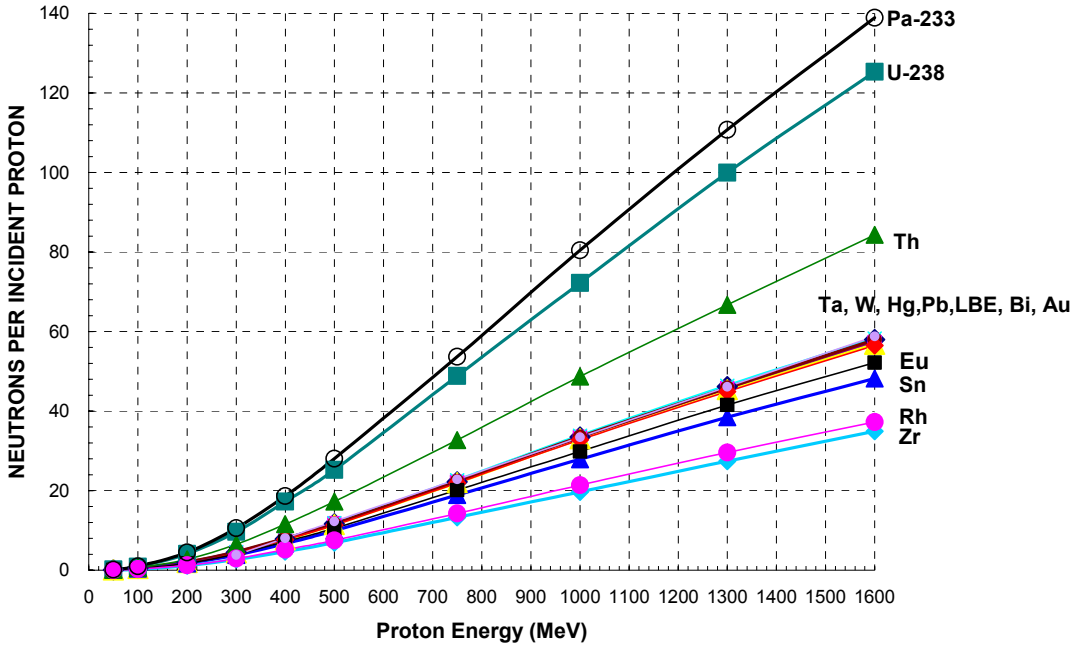

FIG. 5.3 Neutron productions of infinite targets for different materials.

TABLE 5.1 Fitting results for neutron production at higher incident energies.

	y=a*(x-b)	
	a	**b**
	(n/p per MeV)	(MeV)
Pb	0.0424	219.7736
LBE	0.0416	209.0361
Bi	0.0414	214.1184
Ta	0.0423	212.6005
W	0.0421	216.3705
Hg	0.0418	217.9737
U	0.0913	215.7722
Sn	0.0349	208.4183
Zr	0.0255	228.8431

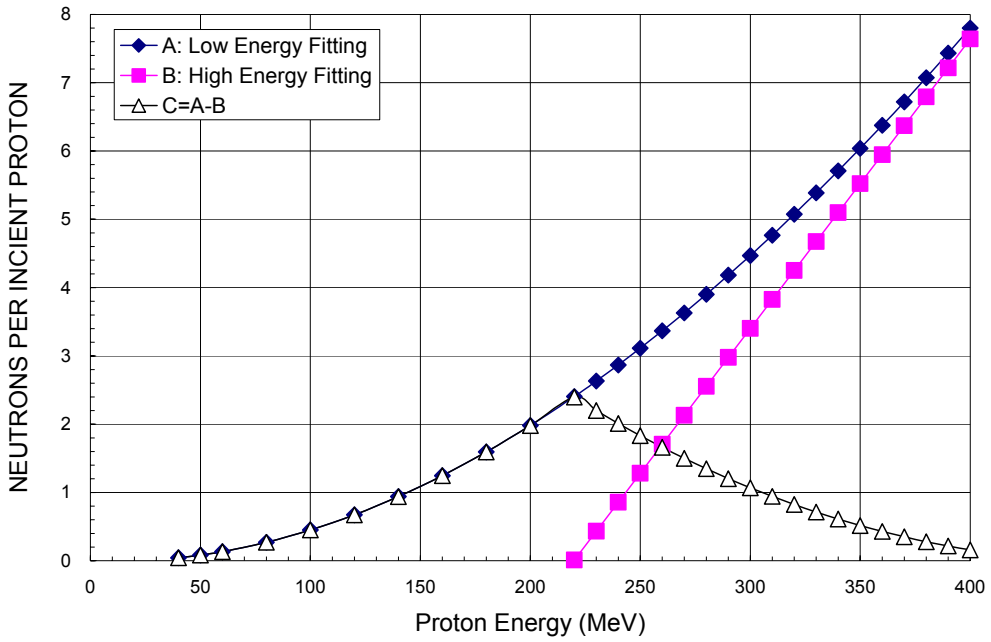

FIG. 5.4 Fitting analysis of neutron production at lower incident energies.

5.2.3 Neutron production versus target materials

Another interesting phenomenon in FIG. 5.3 is that for the materials from Ta to Bi whose atomic number ranges from 73 to 83, the neutron production curves just overlap to one another. However the physical properties of the materials differ from one another. It reveals that the capacity of neutron production of materials in this rang is not sensitive to the atomic number. The conclusion is further confirmed by the experimentally measured data for neutron production from thick targets (Pb, Hg, and W) under the bombardment of 0.4 up to 2.5 GeV proton [54].

FIG. 5.5 shows the neutron production versus the atomic mass of the target material at bombard energies from 300 to 1600 MeV. At a certain energy, the neutron production increases with the increasing atomic mass of the target material since there are more neutrons and protons waiting to be released inside heavier nuclei. The only exception lies in Pa-233, U-238, and Th. Since they are both fission materials, the rich neutron production has a large contribution from fission reaction. But the fission

capacity of the material is not discussed in our work. As illustrated by FIG. 5.5, for the remaining materials the tendency of the neutron production increasing with increasing atomic mass is very small. The only two step rises are from Rh (Z=45) to Sn (Z=50), and from Bi (Z=83) to Th (Z=90). The curve between Ta and Bi remains almost flat with a little fluctuation.

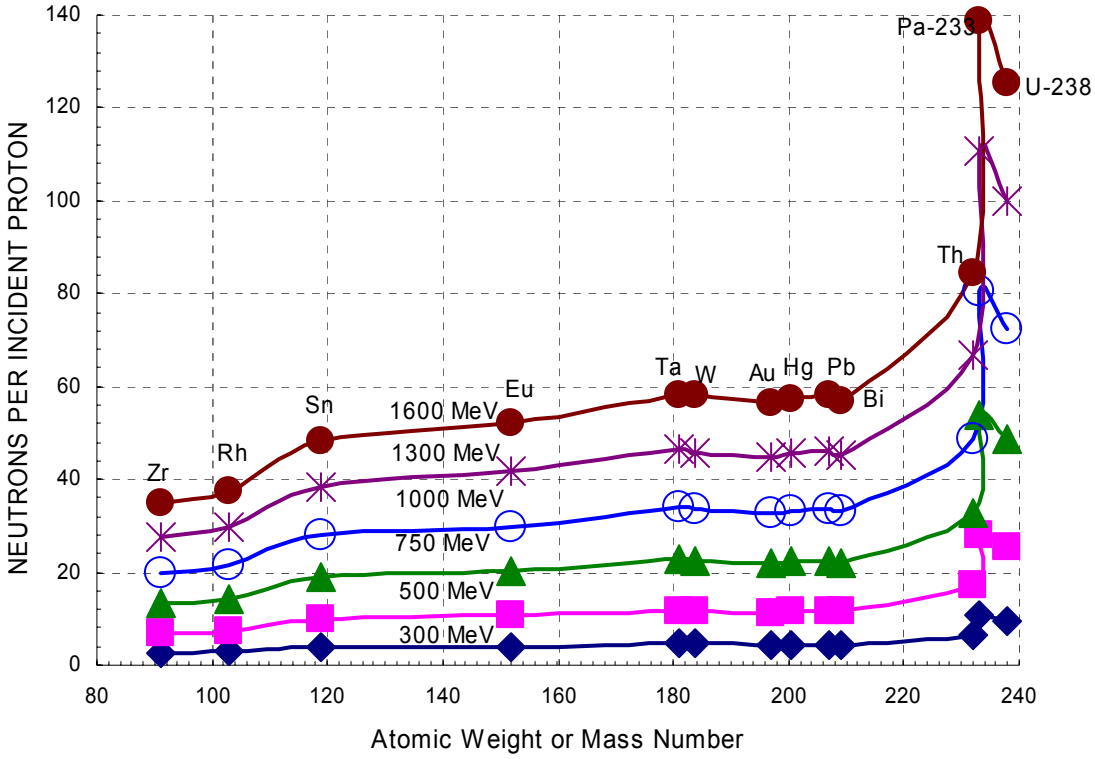

FIG. 5.5 Neutron productions versus atomic mass number of different materials.

5.2.4 Summary and conclusions

We explored the maximum neutron production of the target materials due to spallation reactions in "infinite" targets. Some of calculation results were compared with experimental data. The results are illustrative and a few conclusions may be made:

(1) Neutron production increases polynomially with the incident proton energy at the lower energy region. However at the higher energy region, it increases proportional to the incident proton energy.

(2) 220 MeV appears as the "threshold" for the neutron production in all materials. It is not a true threshold, instead it represents the level above which the energy partitioned to excite the nuclei while not later contribute to the neutron production may be ignored.

(3) The neutron production is attributed to two components: the lower energy part and the higher energy part. A fitting analysis of the two components was showed.

(4) The capacities of neutron production due to spallation reactions for materials with atomic number from 73 to 83 are very close to one another. The underlying physics for this conclusion requires a complete investigation.

Chapter 6

Radiation damage calculations of Target 5

6.1 SINQ system modeling

6.1.1 SINQ configuration and Target 5

The SINQ target irradiation program is scheduled in four phases with different spallation targets in each phase. In STIP III, the spallation target is in the shape of a square box and is designated as Target 5. It has some of the same characteristics as the previous STIP targets. The target is located inside a safety full, which consists of a vertical double cylinder (two shells, one inside the other) connected at the bottom to a mating double hemisphere. A schematic diagram of the STIP III Target 5 is shown in FIG. 6.1. For convenience in modeling, the cylinder axis is chosen to be the Z axis directed upwards and in the same direction as the proton beam. The X and Y axe are horizontal with the X axis perpendicular to the plane of paper. The hemispherical section of the safety hull is designated as the entrance window. At the lowest point of the entrance window, the thickness of each shell is 2 mm, and the gap between them is also 2 mm. The thicknesses of the shells and the gap increase gradually to 3 mm at Z=0 in FIG. 6.1 [55]. The outside diameter of the outer cylinder and the outer hemisphere is 21.2 cm. The safety hull and the rod-container box are both made of AlMg3, whose composition is given in TABLE 6.1. Target 5 contains three types of "rods" in a rod-container box; all three types have 316L tube as the outer member.

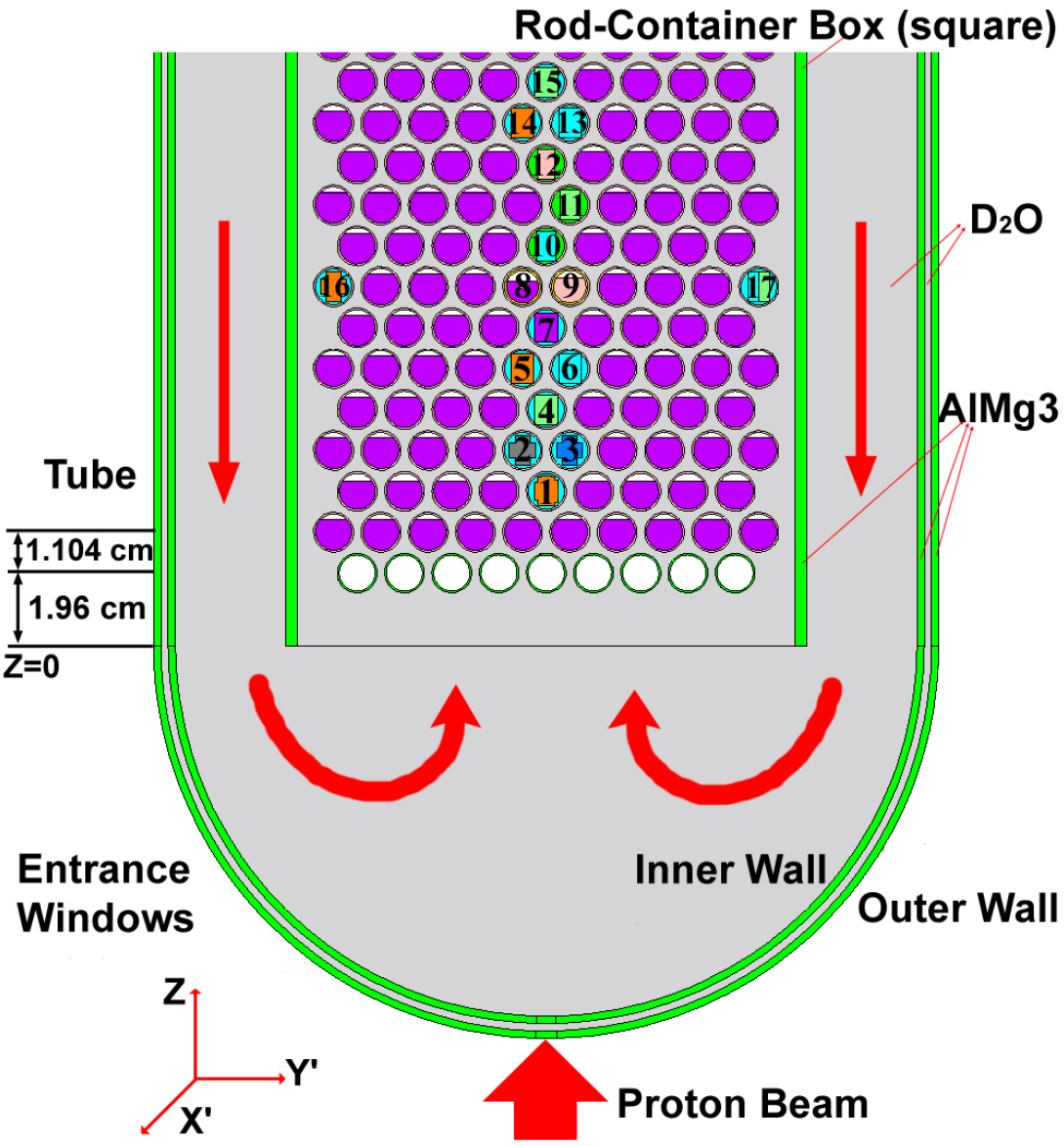

FIG. 6.1 A schematic diagram of Target 5 (Rods 1 to 17 contain specimens for irradiation).

These rods are: (1) target rods, typically 13.4-cm-long 90% filled with the Pb target material, (2) empty rods at the bottom layer, and (3) specimen rods containing test specimens. The rods are arranged in layers and the center-to-center distance between layers is 1.10 cm. The specimen rods are specifically numbered in FIG. 6.1 from 1 to 17 (1-15 are central rods and 16 and 17 are side rods). The densities and compositions of the specimen materials are given in TABLE 6.1, and the contents of

each of the 17 specimen rods are identified in TABLE 6.2. FIG. 6.2 is a radial cross section diagram of Target 5, which shows the axial direction of the rods is parallel to X' (X' and Y' axes are rotated 45º from X and Y axes). Also as shown in FIG. 6.2, the footprint of the incident proton beam (i.e., the area that contains the incident beam) is an ellipse with minor and major axes along X and Y, respectively.

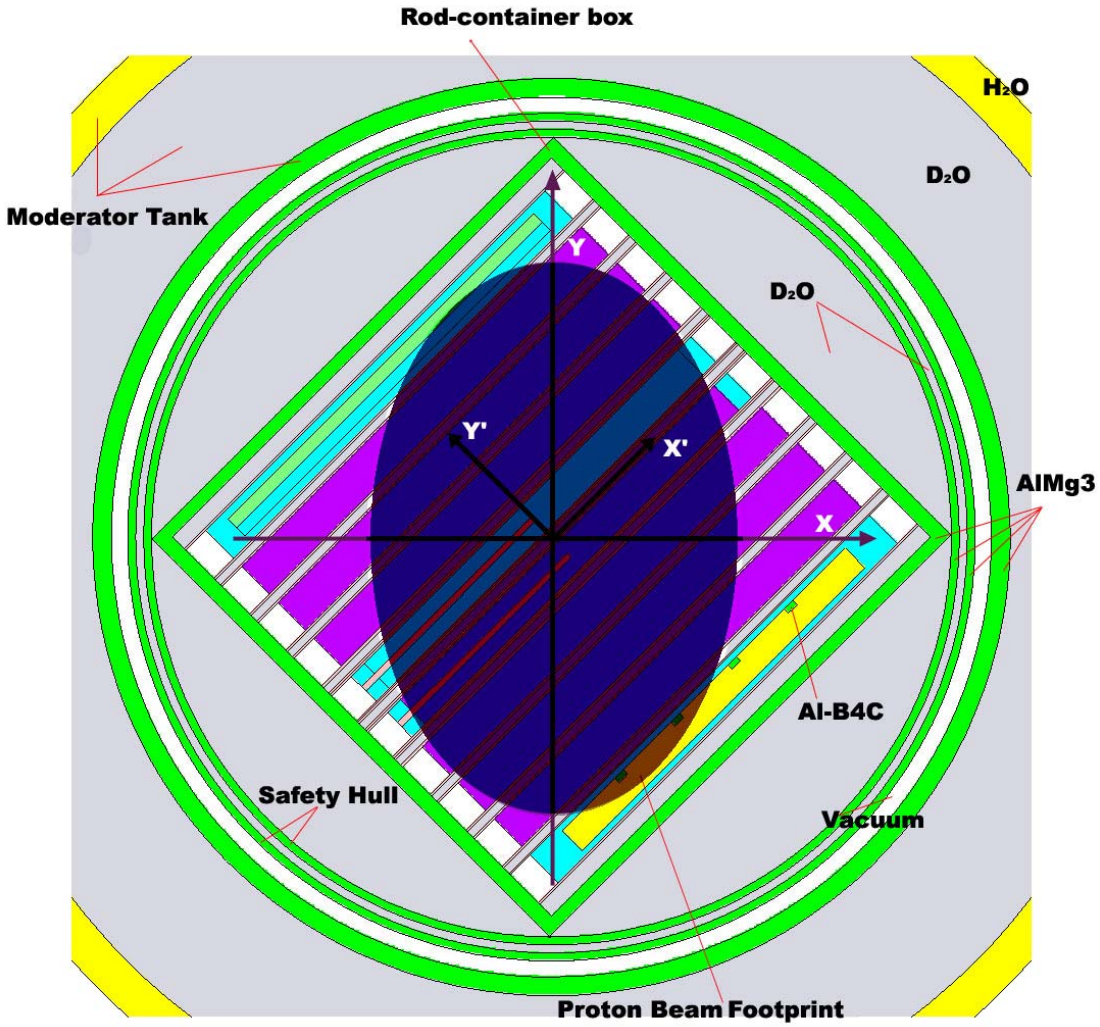

FIG. 6.2 Cross section diagram of 8th layer of specimen rods in Target 5 (not to scale).

As shown in FIG. 6.1, the target rods are cooled by D_2O, which flows down between the inner wall of the inner shell and the rod-container box and then upward past the target and specimen rods in the rod-container box. D_2O also flows in the

annulus between the inner and outer shells. The safety hull is further surrounded by a larger cylinder container of aluminum (inner radius is 11 cm), which is surrounded by a cylindrical layer of heavy water, 90 cm in thickness, followed by another cylindrical layer of light water, 10 cm in thickness (FIG. 6.2). The larger cylinder container, the heavy water layer and the light water layer serve as the moderator tank for the target with the cylinder container as the boundary. Whenever a particle hits into the moderator (D_2O and H_2O) of the moderator tank region, it has only a small chance to be reflected back into the safety hull, which implies insignificant effects on the flux inside the safety hull. To save the calculation time, in geometry modeling the heavy water layer and the light water layer are therefore reduced to a thickness of 4 cm and 1 cm, respectively, which results in a factor of 10 shorter calculation time.

6.1.2 Specimens rods inside Target 5

A typical geometry for specimen rods is sketched in FIG. 6.3. The 316L tube has a total length of 13.4 cm, the outer diameter is 1.08 cm, and the inner diameter 0.98 cm. All the specimens are contained within the tube in a specimen holder of alloy T91 for Rods 1-9 and 13-17 or AlMg3 for Rods 10-12 (diameter 0.98 cm and length 12 cm). The specimen holder is hold within the 316L tube to the cladding, leaving voids equally at the two ends for ease of mechanical processing. It is recessed inside to form a hollowed-out region for containing specimens (orange region). The length of this region may vary from 9.6 to 11.0 cm depending on the rod, since designs differ from rod to rod. Exceptions to this geometry configuration are central rods 8 and 9 located at the 8th layer from the bottom as shown in FIG. 6.2. Rods 8 and 9 are different from regular specimen rods in that they do not contain test specimens; instead they have an inner tube as cladding (outer diameter 0.98 cm and inner

diameter 0.88 cm) of Zircaloy-2 (Zirc-2) filled with specific metals (lead for Rod 8 and lead-bismuth for Rod 9). At the center of each, there is a thermocouple for measuring the temperature of the target. Since the composition of the thermocouple is complicated, it is simulated as 316L in the calculations.

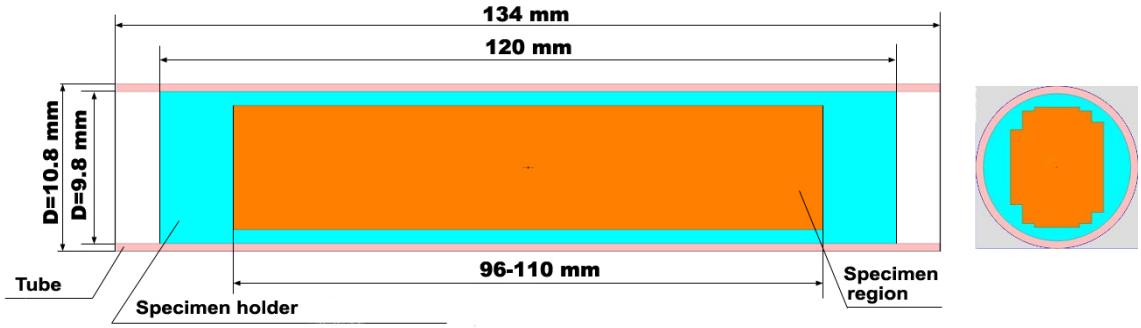

FIG. 6.3 Axial and radial cross section diagram of Specimen Rod 1 in Target 5.

Most of the test specimens are austenitic and martensitic steels, including 316L, T91, Eurofer97, F82, EP823, EP823(ods) and HT-9. A few of them are pure metals like Ta, Au, Cu, Ti, and Ni. There is an interesting material—Al-B4C—inside Rod 16, as shown in FIG. 6.2. The regions containing Al-B4C are tallied separately in calculations. TABLE 6.1 lists all compositions of the specimen materials used in the Target 5 and their densities, although due to lack of specific density information for the steels, all of the steels are assigned the same density of 7.76 g/cm^3. TABLE 6.2 lists all the materials in the rods, including tube, holder, and specimen materials. As noticed in TABLE 6.2, the specimen holder for Rod 17 is separated into two cells, since it contains two kinds of specimens in two separated sub-regions. The specimens inside the rods have different geometries and are irradiated for different purposes. The typical ones are TEM, tensile, bend fatigue, bend bar and Charpy specimens. FIG. 6.4 [3] shows a typical specimen package of one rod. The detailed description of

specimen geometries and configuration is presented in [56]. The gaps between the specimens are filled with 316L filler pieces.

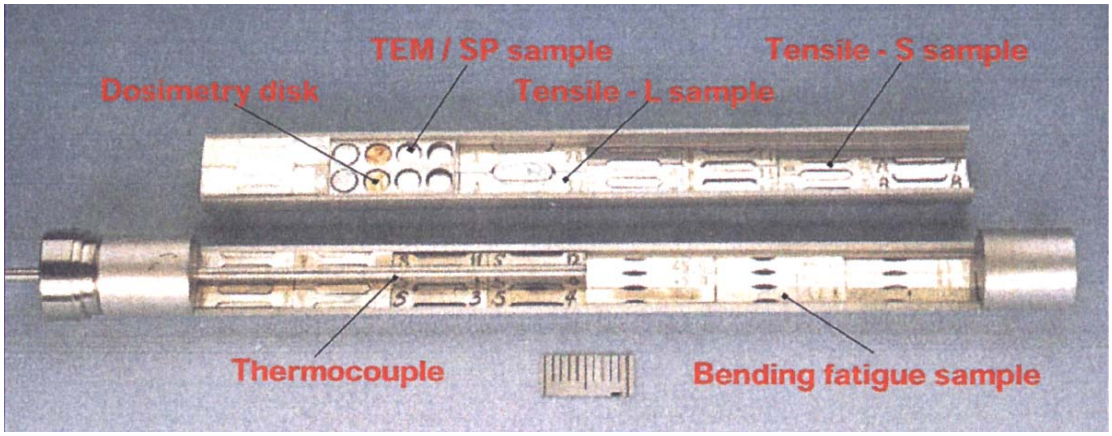

FIG. 6.4 An example of specimen package [3].

Since most of the materials are steel specimens whose compositions do not vary significantly, we used an average-effective method to describe the region where specimens reside inside the rods. In the calculations, we treat the region containing specimens as a whole single cell, and we consider all the atoms of the different specimens to be distributed uniformly inside the region. The average-effective compositions for Rods 1, 2, 3, and 16 are given in TABLE 6.3. Other specimen rods contain single materials inside the rods, and there is no need to use the average-effective method. The use of a single average-effective composition for the specimen rods in this way saves a huge amount of work instead of describing every single specimen, which may be complicated in geometry. Also, this simplification improves the efficiency of the calculations.

TABLE 6.1 STIP III specimen material compositions.

Material Name	Density (g/cm^3)	Compositions (wt%)													
		Fe	Cr	Ni	Mo	Mn	Ti	Co	Cu	C	Si	P	S	N	Ta
SA316L	7.76	65.5590	17.4500	12.2000	2.5000	1.8100	------	------	------	0.0240	0.3900	------	------	0.0670	------
T91	7.76	89.4330	8.6300	0.2300	------	0.9500	0.0030	0.0190	0.0460	0.1000	0.3100	------	0.0060	------	------
Eurofer97	7.76	88.8800	8.9900	0.0070	------	0.4400	0.0090	0.0040	0.0210	0.1200	0.0700	------	0.0040	0.0160	0.1400
F82H /F82H (ods)	7.76	89.6218	7.8700	0.0200	0.0030	0.1000	0.0040	------	0.0100	0.0900	0.0700	0.0030	0.0010	0.0070	0.0300
EP-823	7.76	81.7700	12.0000	0.8900	0.7000	0.6700	------	------	------	0.1400	1.8000	------	------	------	------
HT9	7.76	84.8400	11.8000	0.5800	1.0200	0.5000	------	------	------	0.2100	0.2200	0.0070	0.0030	------	------
Ta/Ta(15%cw)	16.60	------	------	------	------	------	------	------	------	------	------	------	------	------	100.000
Zr-2	6.49	0.1700	0.1100	0.0660	------	------	------	------	------	------	------	------	------	------	------
Pb	11.40	------	------	------	------	------	------	------	------	------	------	------	------	------	------
Pb-Bi	10.40	------	------	------	------	------	------	------	------	------	------	------	------	------	------
AlMg3	2.66	0.2500	0.0400	------	------	0.3500	0.0300	------	0.0300	------	0.3000	------	------	------	------
Al	2.70	------	------	------	------	------	------	------	------	------	------	------	------	------	------
Cu	8.96	------	------	------	------	------	------	------	100.000	------	------	------	------	------	------
Nb	8.55	------	------	------	------	------	------	------	------	------	------	------	------	------	------
Ti	4.50	------	------	------	------	------	100.000	------	------	------	------	------	------	------	------
Au	19.30	------	------	------	------	------	------	------	------	------	------	------	------	------	------
Ni	8.90	------	------	100.000	------	------	------	------	------	------	------	------	------	------	------
Fe	7.86	100.000	------	------	------	------	------	------	------	------	------	------	------	------	------
Al-B4C	2.60	0.4900	0.1400	------	------	0.1050	0.1050	------	------	6.7300	0.4200	------	------	------	------

TABLE 1(Continued) STIP III specimen material compositions

Material Name	Density (g/cm^3)	Compositions Continued (wt%)												
		Nb	V	Sn	W	Al	Pb	O	Bi	Mg	Au	Zr	Zn	B
SA316L	7.76	------	------	------	------	------	------	------	------	------	------	------	------	------
T91	7.76	0.0600	0.2100	0.0030	------	------	------	------	------	------	------	------	------	------
Eurofer97	7.76	------	0.1900	------	1.1000	0.0080	------	0.0010	------	------	------	------	------	------
F82H /F82H (ods)	7.76	0.0002	0.1900	------	1.9800	------	------	------	------	------	------	------	------	------
EP-823	7.76	0.4000	0.4300	------	1.2000	------	------	------	------	------	------	------	------	------
HT9	7.76	------	0.3200	------	0.5000	------	------	------	------	------	------	------	------	------
Ta/Ta(15%cw)	16.60	------	------	------	------	------	------	------	------	------	------	------	------	------
Zr-2	6.49	------	------	1.3600	------	------	------	0.1340	------	------	------	98.1600	------	------
Pb	11.40	------	------	------	------	------	100.000	------	------	------	------	------	------	------
Pb-Bi	10.40	------	------	------	------	------	45.0000	------	55.0000	------	------	------	------	------
AlMg3	2.66	------	------	------	------	96.2400	------	------	------	2.7200	------	------	0.0400	------
Al	2.70	------	------	------	------	100.000	------	------	------	------	------	------	------	------
Cu	8.96	------	------	------	------	------	------	------	------	------	------	------	------	------
Nb	8.55	100.000	------	------	------	------	------	------	------	------	------	------	------	------
Ti	4.50	------	------	------	------	------	------	------	------	------	------	------	------	------
Au	19.30	------	------	------	------	------	------	------	------	------	100.000	------	------	------
Ni	8.90	------	------	------	------	------	------	------	------	------	------	------	------	------
Fe	7.86	------	------	------	------	------	------	------	------	------	------	------	------	------
Al-B4C	2.60	------	------	------	------	67.5700	------	------	------	0.7000	------	0.0840	0.1750	23.4800

TABLE 6.2 Materials in specimen rods.

Rods	Material Name			Length of Specimen Region (cm)	Z *(cm)
	Tube	Holder	Specimen Material		
Rod 1	316L	T91	Ta, Ta(15%cw), F82H, F82H(ods), EP823, HT-9, Eurofer97 & T91	9.6	4.168
Rod 2	316L	T91	F82H, F82H(ods), HT-9 & T91	10.0	5.272
Rod 3	316L	T91	Eurofer97 & 316L	10.0	5.272
Rod 4	316L	T91	Eurofer97	10.8	6.376
Rod 5	316L	T91	F82H	10.8	7.480
Rod 6	316L	T91	T91	10.8	7.480
Rod 7	316L	T91	HT9	10.8	8.584
Rod 8	316L Zr-2	T91	Lead	11.1	9.688
Rod 9	316L Zr-2	T91	Lead-Bi	11.1	9.688
Rod 10	316L	AlMg3	T91	10.4	10.792
Rod 11	316L	AlMg3	Eurofer97	10.4	11.896
Rod 12	316L	AlMg3	316L	10.4	13.000
Rod 13	316L	T91	F82H	10.8	14.104
Rod 14	316L	T91	T91	10.8	14.104
Rod 15	316L	T91	Eurofer97	10.8	15.208
Rod 16	316L	T91	316L, T91 & Eurofer97	10.0	9.688
Rod 17	316L	T91	T91 Eurofer97	10.8	9.688

*** This column denotes a specimen rod center's position at Z-axis, which is the distance from the bottom of the rod-container box.**

TABLE 6.3 Materials compositions of "averaged" specimen rods.

Composition (wt%)	Rod 1	Rod 2	Rod 3	Rod 16
Fe	67.721	85.482	76.135	81.017
Cr	11.575	10.565	13.613	11.575
Ni	5.246	1.491	6.671	4.074
Mo	1.132	0.612	1.366	0.805
Mn	1.03	0.795	1.189	0.992
Ti	0.002	0.002	0.004	0.052
Co	0.003	0.009	0.002	0.006
Cu	0.011	0.022	0.010	0.113
C	0.065	0.132	0.068	0.084
Si	0.319	0.264	0.245	0.226
P	0.001	0.003	------	------
S	0.002	0.004	0.002	0.003
N	0.031	0.007	0.044	0.029
Ta	12.355	0.003	0.063	0.063
Nb	0.027	0.027	------	0.103
V	0.106	0.228	0.086	0.132
Sn	0.0005	0.001	------	0.001
W	0.373	0.355	0.499	0.493
Al	0.001	------	0.004	0.032
O	0.00014	------	0.000	0.000
Au	------	------	------	0.201
Density (g/cm^3)	8.305	7.760	7.760	7.765

6.1.3 Entrance windows

The entrance windows are the hemispherical section of the safety hull, the most upstream position to the proton beam. They are double layered as the inner and the outer entrance window. The thickness of each window and the gap between them are 2 cm at the lowest point, gradually increasing to 3 cm at Z=0 in FIG. 6.1. The entrance windows are made of AlMg3 whose capacity in withstanding radiation damage is the main concern in the design of the safety hull. Therefore, calculations have to be done for checking the status of material degradation of the entrance windows. The characteristic points on the windows and their tally volumes are carefully selected for the calculations. FIG. 6.5(a) shows the locations of these points. FIG. 6.5(b) is an enlarged and separated view of the tally volume of P_0, the lowest tip of the window. It consists of an intersection of a 1.5 degree half-angle cone surface and the window wall. Other points are sampled in the same way every 15 degrees symmetrically at YZ and XZ planes. The tally volumes are 0.022 cm^3 for P_6 and P_6', and 0.044 cm^3 for the remaining points.

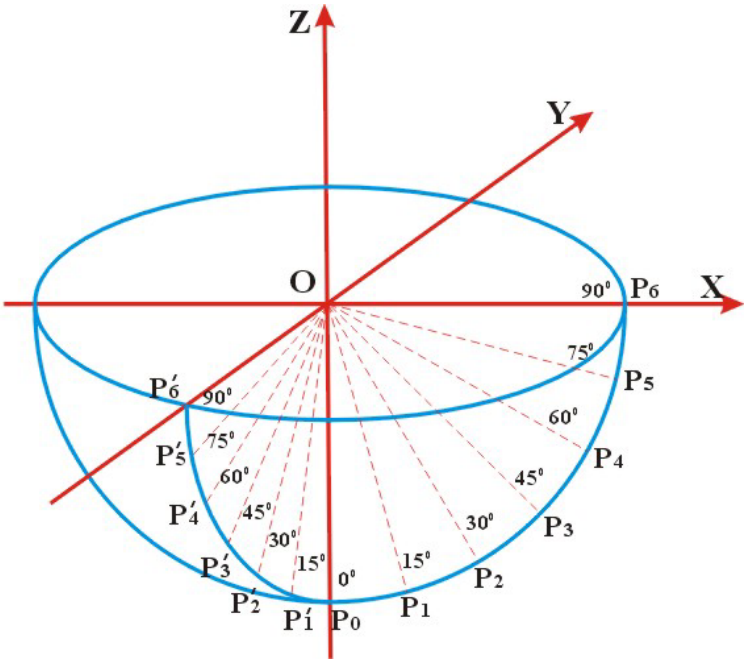

FIG. 6.5(a) Sampling points at the outer entrance window of Target 5.

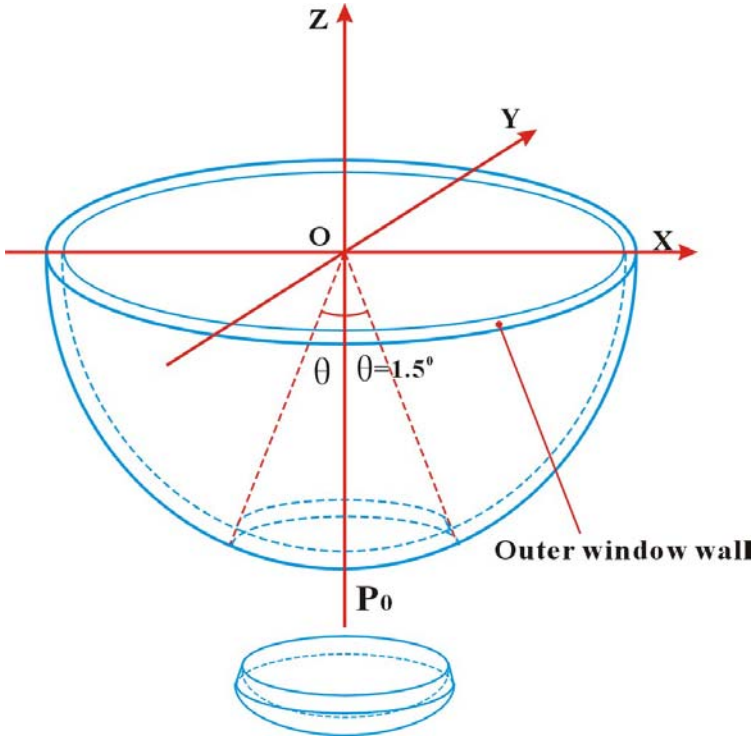

FIG. 6.5(b) Enlarged part of tally volume of P_0 at the outer entrance window of Target 5 (not to scale).

6.2 Proton source beams

As discussed in Chapter 4, proton beam is directed from the pion target (Target E) through beam guides into the bottom of the SINQ target. The configuration of the pion target, like target thickness, may produce different profiles and energies of the proton beam. There are two beams used in the calculations: (a) Beam 1 at 575 MeV, an experimentally measured profile at Target E, and (b) Beam 2 at 570 MeV, a simulated truncated double-Gaussian profile.

FIG. 6.6 presents color-coded contour diagrams of the proton beam current density as a function of x and y for Beam 1 (FIG. 6.6(a)) and Beam 2 (FIG. 6.6(b)). The key to the color coding is given in the vertical color strip at the upper right-hand corner of each diagram in units of protons/cm^{2}s at (x,y) per mA of source beam. As shown in FIG. 6.6, Beam 1 has a blocky discontinuous appearance due to the large step size for the experimental measurement (1x1cm). It also seems to have a more compacted profile than Beam 2, especially along the Y axis, with a higher peak current density. A more clear comparison of the two beams is made in FIG. 6.7, which shows profiles along X and Y axes, respectively, for Beams 1 and 2. As shown in FIG. 6.7, the shape of curve for Beam 1 along X axis appears to be roughly Gaussian (the fitting result reveals a $(FWHM)_X$ of about 5.0 cm) and is close to that of Beam 2 which is a Gaussian distribution with a $(FWHM)_X$ of 5.0 cm. However, along Y axis Beam 1 has a rather narrower shape of curve compared to Beam 2. The peak current density of Beam 1 is 1.86 x 10^{14} 10^{14} protons/cm^{2}s per mA, about 22% higher than that of Beam 2.

As indicated in FIG. 6.6(b), Beam 2 [55] is a double Gaussian distribution confined to an ellipse (footprint ellipse) with semi-axes R_X = 4.24 cm and R_Y = 7.12 cm, where the X and Y directions are rotated 45° from the X' and Y' axes shown in

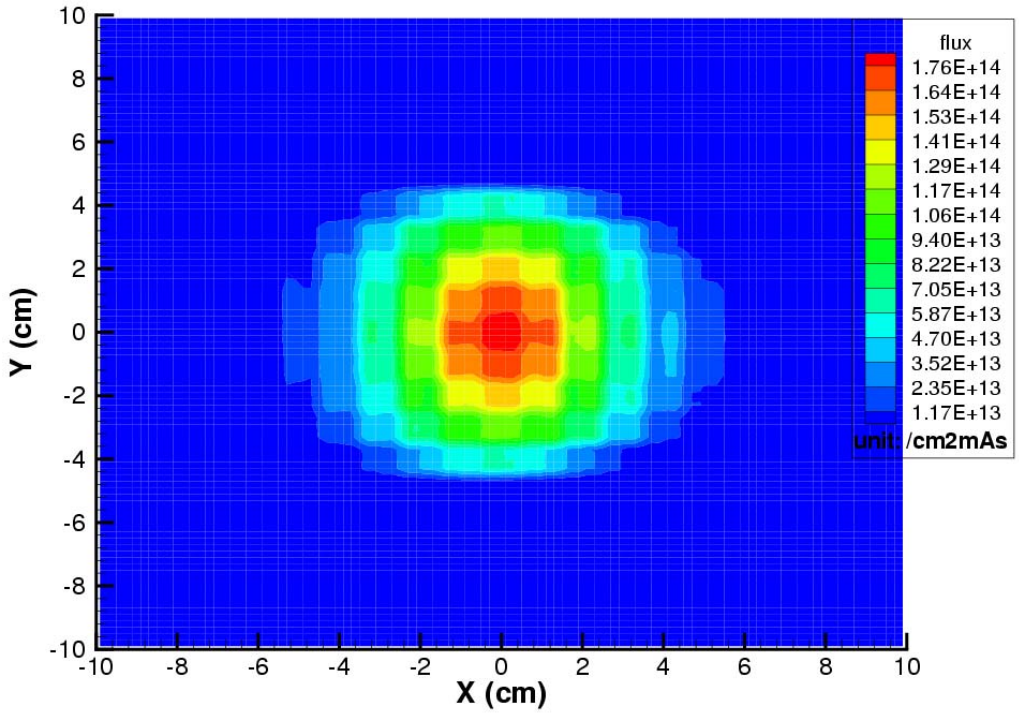

FIG. 6.6(a) STIP III proton source beam profile, Beam 1 (measured), incident proton energy, 575 MeV.

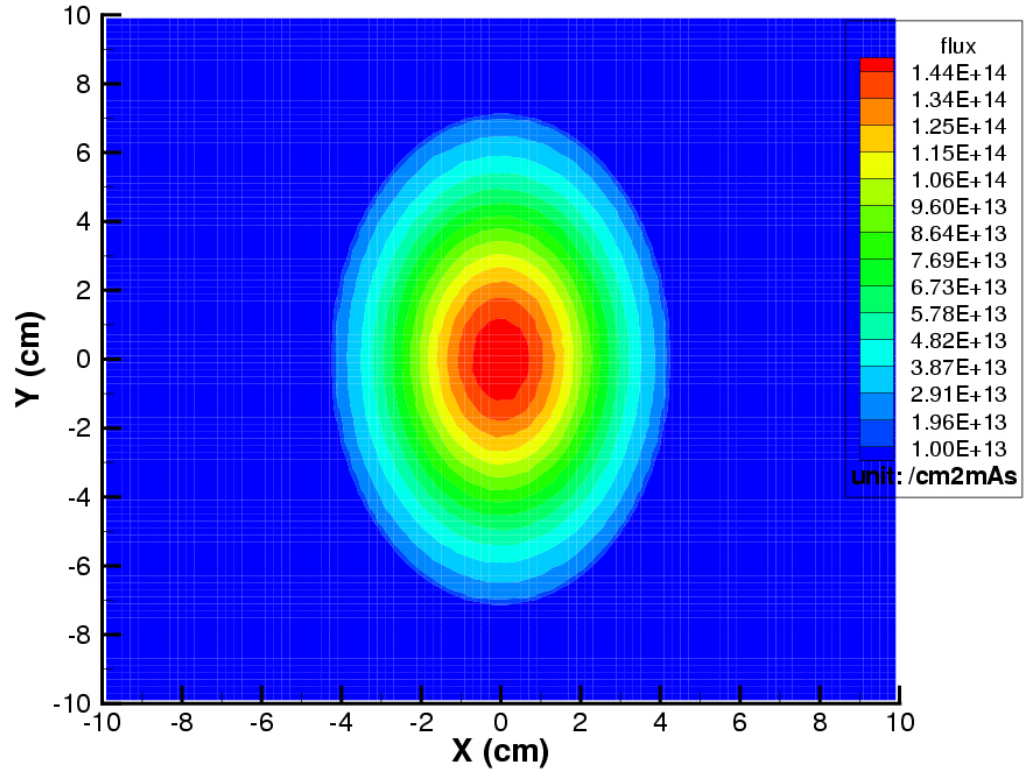

FIG. 6.6(b) STIP III proton source beam profile, Beam 2 (truncated Gaussian), incident proton energy, 570 MeV
(σ_x= 2.12 cm, σ_y= 3.56 cm, confined by an ellipse R_x=4.24 cm, R_y=7.12 cm).

FIG. 6.2. The Gaussian parameters of Beam 2 are σ_x = a = $R_X/2$ = 2.12 cm and σ_y = b = $R_Y/2$ = 3.56 cm. The current density function is given by

$$\frac{p(x,y)}{p(0,0)} = \exp\{-\frac{1}{2}[\left(\frac{x}{a}\right)^2 + \left(\frac{x}{b}\right)^2]\} \qquad (6.1)$$

where p(x,y) is the current density at x,y per incident proton. The integral of p(x,y) over the footprint ellipse gives the total current

$$I = 2\pi[1-\exp(-2)]\ ab\ p(0,0) \qquad (6.2)$$

and, setting I = 1, we get p(0,0) = 0.024 p/cm^2 per incident proton. Since there are 6.24 x 10^{15} p/s per mA, we also get p(0,0) = 1.52 x 10^{14} p/cm^{2}s per mA, nearly the same value from MCNPX mesh tally in FIG. 6.7. Furthermore, the equation of the footprint ellipse is

$$\left(\frac{x}{2a}\right)^2 + \left(\frac{y}{2b}\right)^2 = 1 \quad (6.3)$$

and we see by (1) and (3) that at the footprint ellipse

$$p(x,y)=p(0,0)\ \exp(-2) = 0.135\ p(0,0) \qquad (6.4)$$

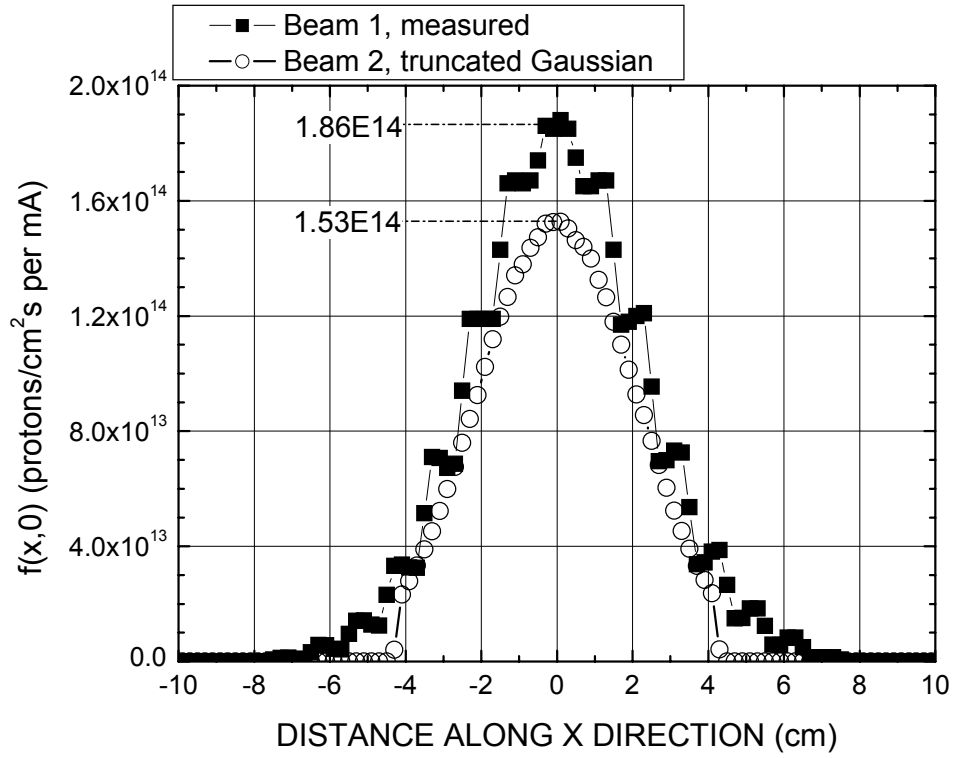

FIG. 6.7(a) Current density per mA of total current vs distance along the X direction at y = 0 for Beam 1 (measured) and Beam 2 (truncated Gaussian).

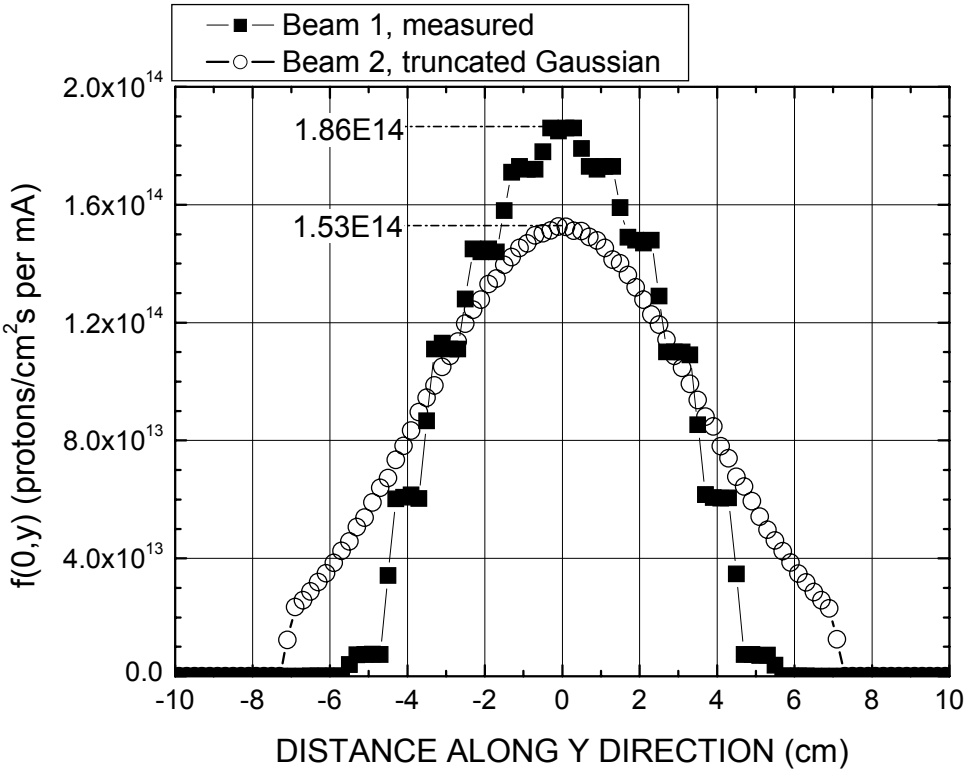

FIG. 6.7(b) Current density per mA of total current vs distance along the Y direction at x = 0 for Beam 1 (measured) and Beam 2 (truncated Gaussian).

6.3 Flux calculations

6.3.1 Flux distribution in Target 5

Although the calculations are done based on two beam profiles: Beam 1, an experimentally measured profile at an upstream location, and Beam 2, a truncated double Gaussian profile, the results from the calculations for the two beam profiles reveal that they bear similar characteristics in flux distribution and flux spectra. Therefore, only the results for Beam 2 are presented here and the difference between Beams 1 and 2 is mentioned for the comparison.

FIG. 6.8 presents color-contoured maps of total proton and neutron fluxes throughout the Target 5 for Beam 2. All the plots cover the flux profiles from where the proton beam impinges (the lowest tip of the entrance window, Z=-10.6 cm) to the highest layer of lead rods (Z = 42.24 cm) along Z axis (beam direction) at X=0 or Y=0. FIGs. 6.9(a) and 6.9(b) are the enlarged part of FIGs. 6.8(b) and 6.8(d), respectively, color-contoured maps of total proton and neutron flux profiles at X = 0, with part of the Target 5 structure superimposed.

The proton beam is transmitted through the double entrance windows with negligible scattering or absorption. It is slightly scattered by the heavy water on its way to the targets rods. The highest proton flux region in red in FIG. 6.9(a), corresponding to proton fluxes of about 1.4 to 1.6 x 10^{14} protons/cm^2s per mA, extends from the outer entrance window at Z = -10.6 cm and from Y = -1 cm to Y = +1 cm upward to about the third layer of rods at about Z = 4 cm. As the proton beam travels further into the heavy lead targets rods, the proton flux drops quickly due to more and more proton loss to spallation reactions. Although there are secondary protons produced by spallation reactions, their contribution to the total proton flux is relatively small. Therefore, no apparent increase of proton flux is observed in FIGs.

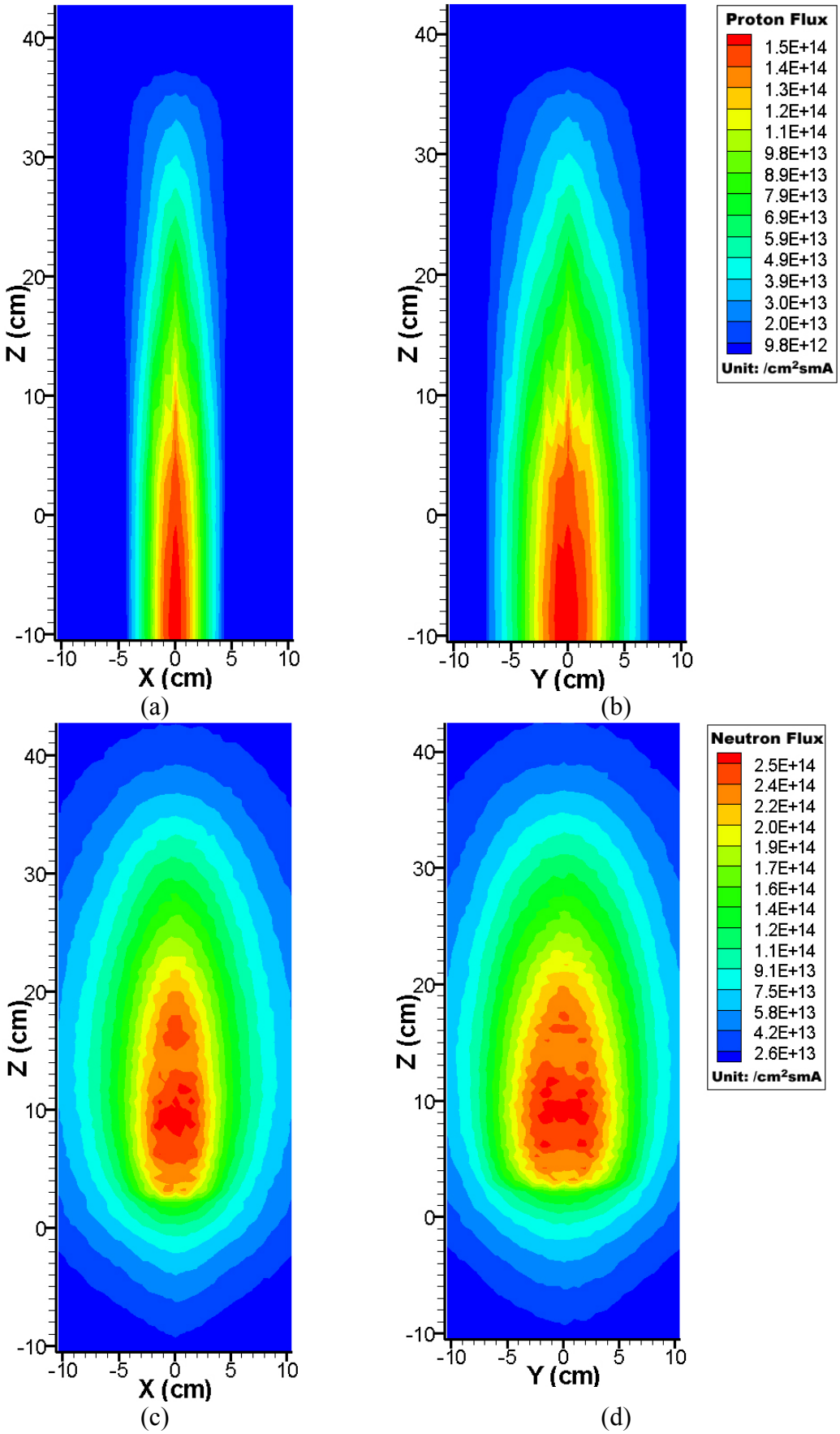

FIG. 6.8 Proton ((a) ~ (b)) and neutron ((c) ~ (d)) flux at SINQ Target 5, Beam 2.

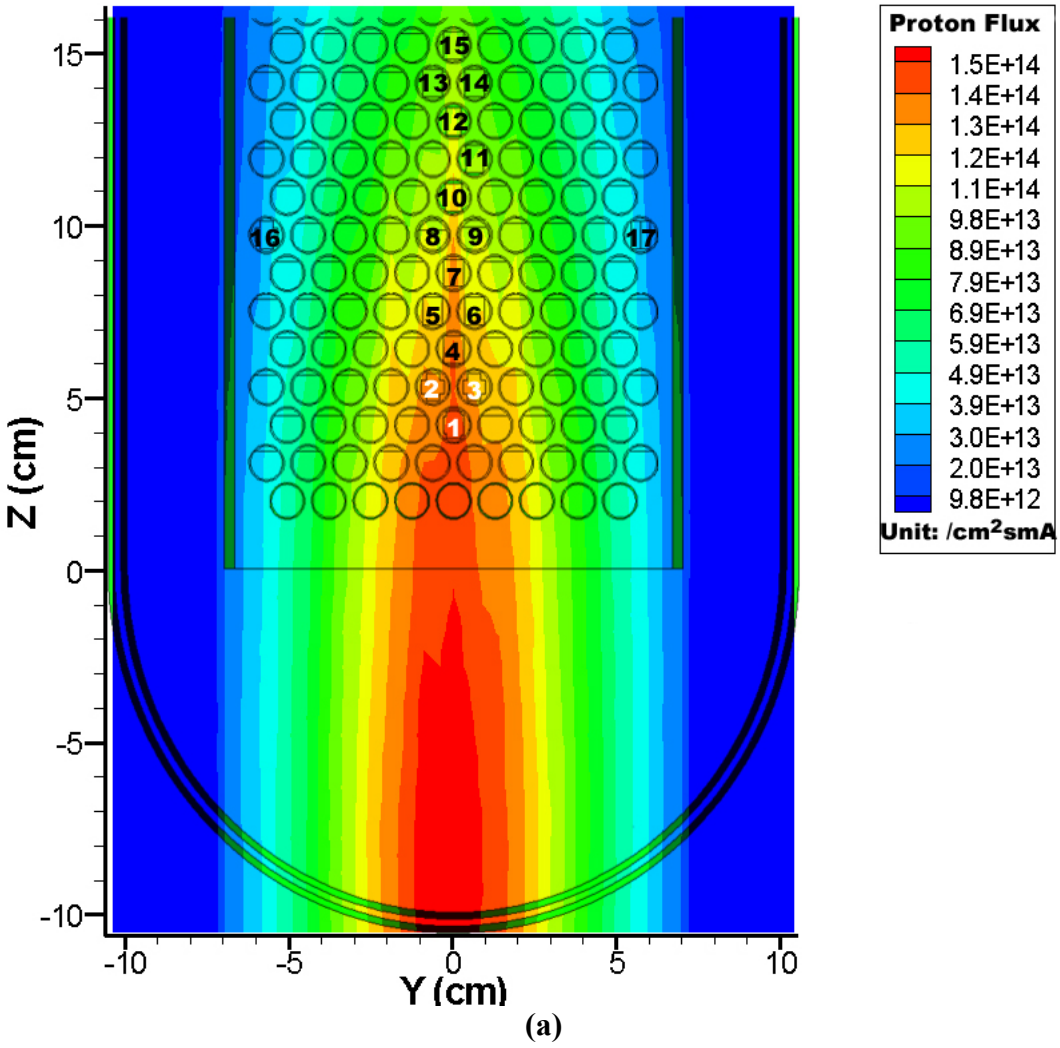
Proton Flux
1.5E+14
1.4E+14
1.3E+14
1.2E+14
1.1E+14
9.8E+13
8.9E+13
7.9E+13
6.9E+13
5.9E+13
4.9E+13
3.9E+13
3.0E+13
2.0E+13
9.8E+12
Unit: /cm2smA
Z (cm)
Y (cm)
15
10
5
0
-5
-10
-10
-5
0
5
10
1
2
3
4
5
6
7
8
9
10
11
12
13
14
15
16
17

(a)

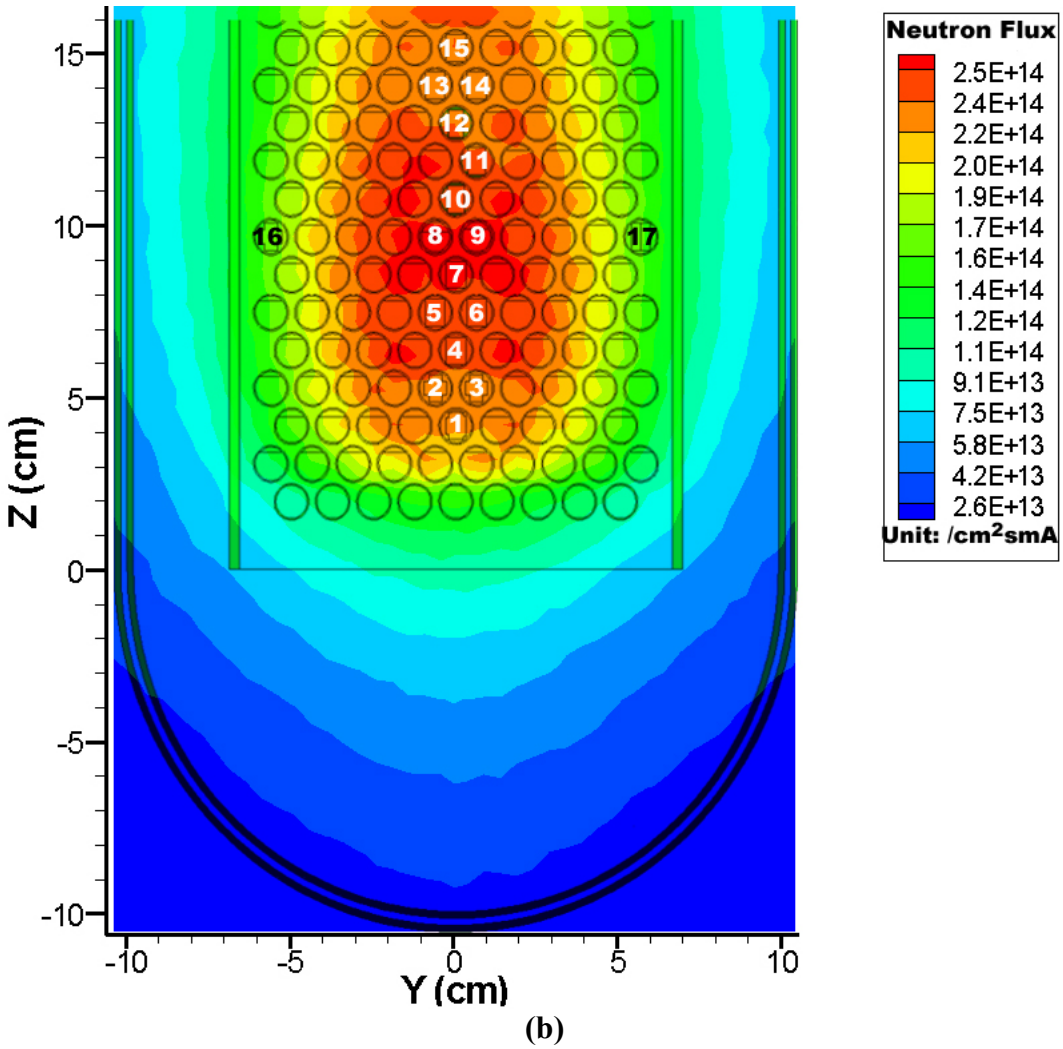

(b)

FIG. 6.9 Proton (a) and neutron (b) flux on Target 5 with part of Target 5 structure imposed for Beam 2.

6.9(a), 6.8(a) and 6.8(b) from the first layer of lead rods at Z = 3.0 cm where the proton beam first interacts with the spallation target to the end layer of the lead rods at Z = 42.5 cm. A comparison of FIG. 6.5(b) with FIGs. 6.8(a) and 6.8(b) reveals that the proton flux profiles in Target 5 follows the source beam profile quite well, that is wider at the Y-axis profile and narrower at X-axis profile.

The neutron flux profiles take a very different appearance than the proton flux profiles. The highest neutron flux region in FIG. 6.9(b) has its center at about Rod 7 and extends from Z = 6 cm to Z = 13 cm and from Y = -3 cm to Y = +3 cm, a central part of the Target 5. The neutron flux decreases gradually along the radial distance

from the highest flux region. The main reason for such a neutron flux profile is that neutrons are largely produced by the spallation reactions, which do not occur until the proton beam hits the lead target rods. The spallation reaction is intensified as the proton beam interacts with more and more lead target rods as it travels further into the Target 5. However, on the other hand as observed in FIGs. 6.8(a) and 6.8(b), the proton flux decreases due to the loss to the spallation reactions which results in fewer spallation reactions and therefore fewer neutrons produced. The neutron flux decreases with distance from the highest flux region more gradually than for the proton flux, especially along the beam direction (Z-axis). This is due to the reduced stopping power for neutrons as compared to protons.

As a production of spallation reaction induced by the proton beam, neutrons have their flux profile following the proton flux profile to some extent. Thus, in FIG. 6.8 for Beam 2 we see that proton flux in the YZ plane along Y (FIG. 6.8(b)) is thicker than in the XZ plane along X (FIG. 6.8(a)), and this is also true for the neutron fluxes as shown in FIGs. 6.8(c) and 6.8(d).

The above characteristics of the proton and neutron flux profiles for Beam 2 are observed in Beam 1 also. The difference between Beam 1 and Beam 2 lies in the profile of YZ plane along Y axis, in which Beam 1 shows both thicker proton and neutron profiles than Beam 2 due to its wider source beam profile along Y axis.

6.3.2 Fluxes at the specimen rods

In tallying fluxes at the specimen rods, each specimen rod is segmented every 0.5 cm in axial length symmetrically from the center until reaching the two ends of the specimen holder. The radial cross sections of the segmentations vary in detail from rod to rod, due to different rod configurations. FIG. 6.10 presents the differential proton and neutron flux spectra of selected central and side specimen rods

for Beams 2, where the rod locations are shown in FIG. 6.1. All the spectra refer to tally volumes 0.5 cm long that extend from x' = -0.5 cm to x' = 0, where the X' direction is indicated in FIG. 6.2.

The proton energy drops when the protons penetrate the layers of lead rods. As shown in FIG. 6.10(a), the proton energy at peak flux decreases as the rods go further away from the beam source or higher into the target rods region in Target 5. The peak flux usually decreases at the same time, but with an interesting exception in that the peak fluxes for Rod 2 and 3, which are at the symmetric position close above Rod 1, are higher than that of Rod 1. Similar phenomena happen for Rods 5 and 6 above Rod 4. This could be due to the inhomogeneous mass or thickness distribution of rods in the incident proton beam direction, which results in inhomogeneous energy absorption of protons. In another sense, it may be explained by the gain of protons spalled from the central rods below them. In addition, the curves of the spectra get wider as the proton beam goes further into the target. The spectra for the central rods above Rod 4 split into two peaks and then generally merge at the furthest rod. At a position far from the center axis (Z axis), the side rod, Rod 16 (FIG. 6.9(a)), has barely observable flux curve in FIG. 6.10(a) since the proton flux at Rod 16 is several orders lower than the central rods.

FIG. 6.10(b) shows the differential neutron flux spectra at three central rods (Rods 1, 7 and 15) and one side rod (Rod 16). Due to the statistical error in the calculations, the curves for the differential neutron fluxes fluctuate frequently at energies above 100 MeV since in this energy region much fewer neutrons are tallied in the calculations. Rods 1, 7, and 15 are well separated along the Z direction and they are also separated from Rod 16 (FIG. 6.9(b)). Nevertheless, the spectra for the four rods look quite alike and nearly overlap in FIG. 6.10(b) for neutron energies

below 0.1 MeV. Above 0.1 MeV, the neutron flux at a given location is more dependent on how well the location is surrounded by the Pb spallation target material.

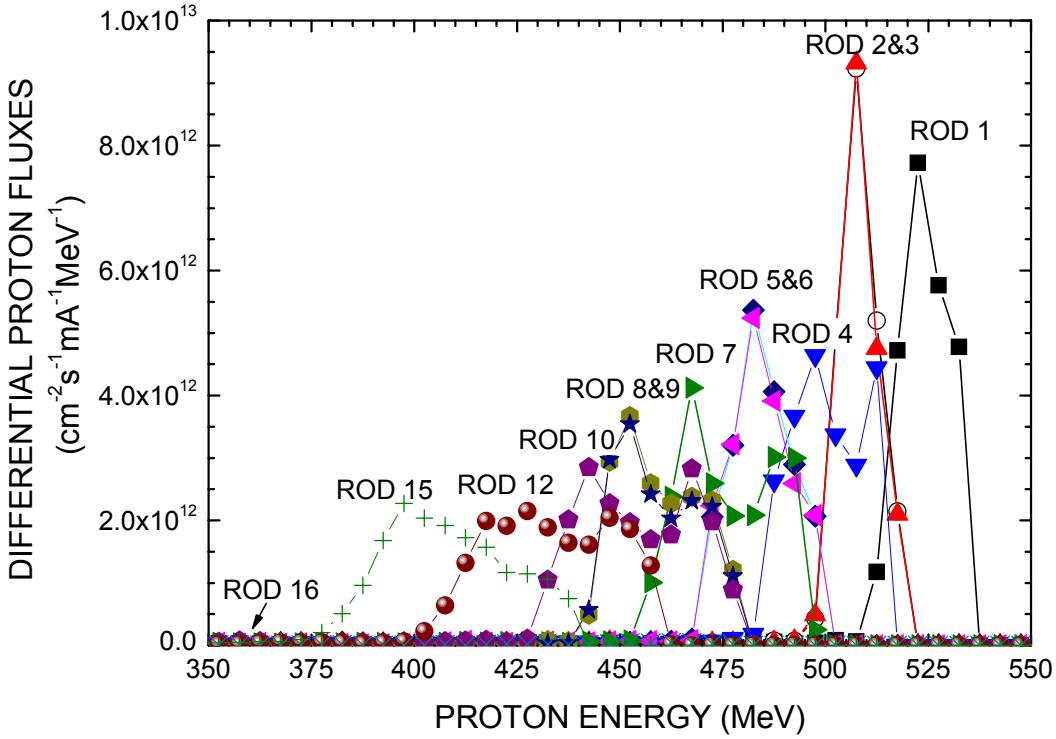

(a)

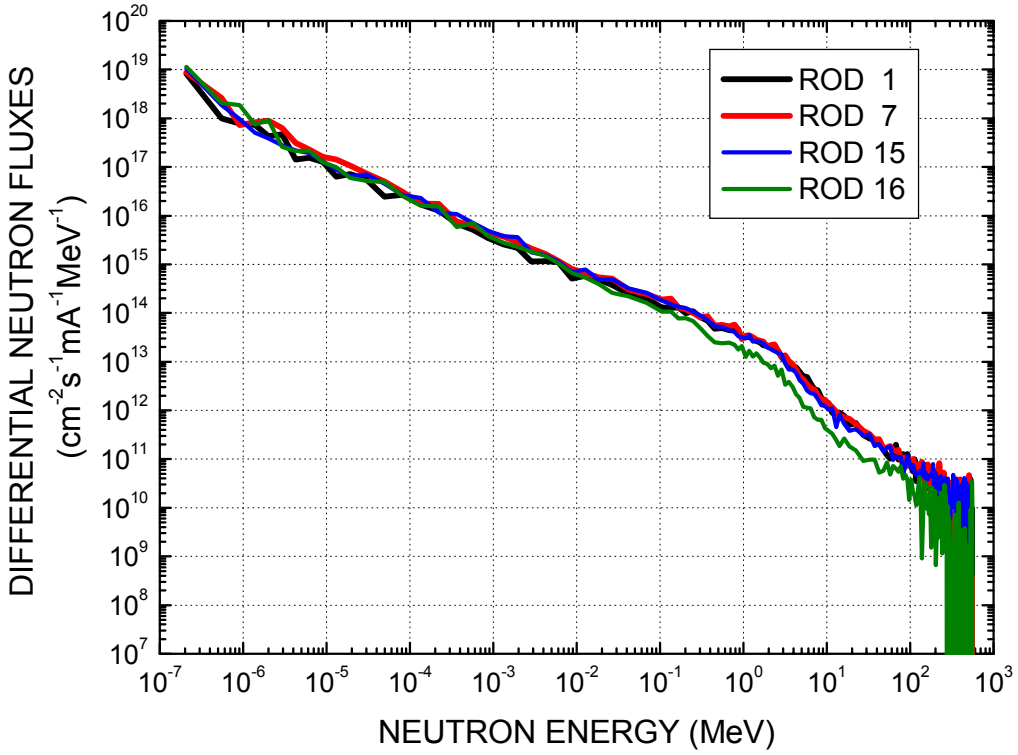

(b)

FIG. 6.10 (a)Proton and (b)neutron differential flux spectra at the centers of specimen rods for Beam 2.

As a result, the neutron fluxes for Rod 16 at the side of Target 5 fall below the fluxes for the central Rods 1, 7, and 15. Another interesting phenomenon observed in the ln-ln plot of FIG. 6.10(b) is that the curves of differential neutron fluxes can be treated as two linear fittings with slightly different slopes below or above the approximate division energy of 2 MeV. This reveals that the differential neutron flux has an exponential dependence on the neutron energy.

FIG. 6.11 presents the proton (FIG. 6.11(a)) and neutron (FIG. 6.11(b)) fluence as a function of distance along the central specimen rods for Beam 2. The fluence is calculated assuming receiving a proton charge of 10 Ahr (2.25×10^{23} protons). The neutron fluence is much higher than proton's, and it drops from the center to the two ends more smoothly than proton fluence, which was also reflected in the proton and neutron flux profiles in FIGs. 6.8 and 6.9. As for the proton fluence at the specimen rods, it reaches its peak at the center of Rod 1 of about 5.4×10^{25} protons/m^2. Then, the fluence drops in a downstream order of the source proton beam. However, for neutrons the highest fluence lies higher in the target at Rod 7 and then drops for rods above and below Rod 7. The reason is already explained in section 6.3.1.

The flux spectra and fluence profiles at the specimen rods for Beam 1 are quite similar, with 10%~20% higher values of peak fluxes or fluence than those produced by Beam 2.

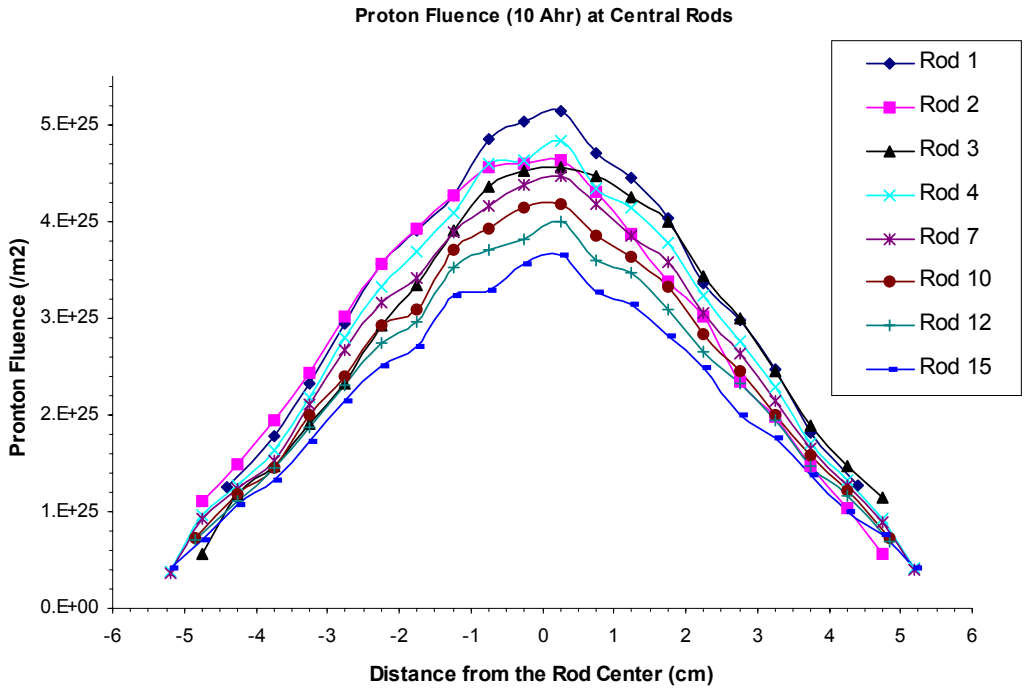

(a)

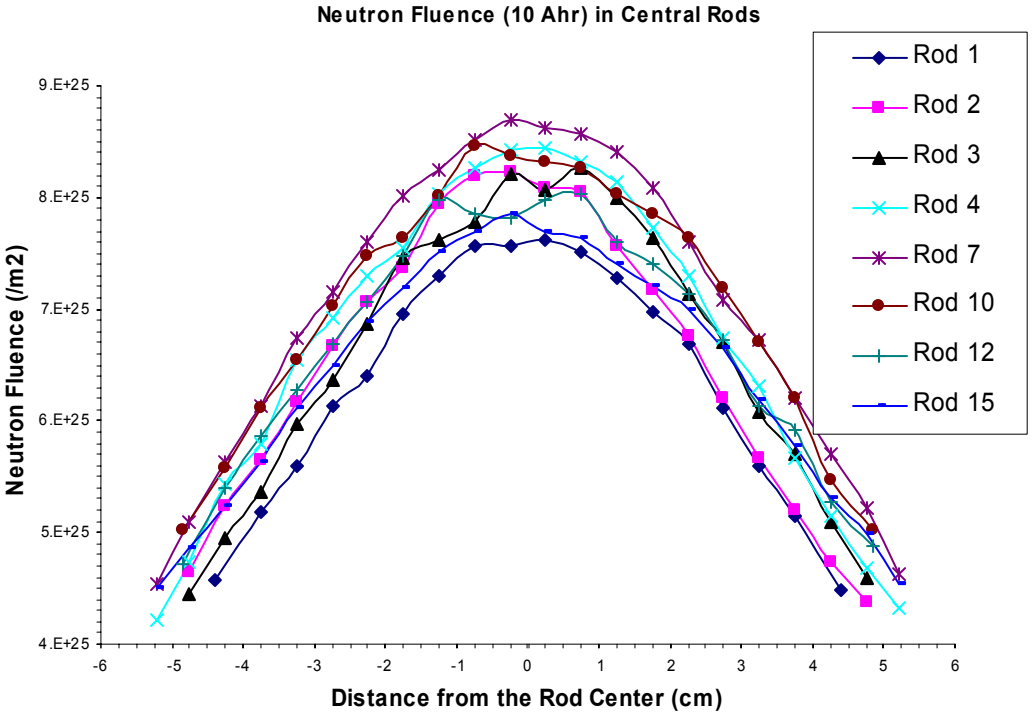

(b)

FIG. 6.11 (a) Proton and (b) neutron fluence after 10 Ahr of irradiation in the central specimen rods, Beam 2, incident proton energy, 570 MeV.

6.3.3 Fluxes at the entrance windows

FIG. 6.12(a) shows the differential proton flux spectra by Beam 2 for the lowest tips of the inner and outer entrance window, which are expected to receive the greatest radiation damage. The two differential proton flux curves look similar as expected. The dominant proton flux occurs at the energy of the incident source beam, and it is several orders higher than for the rest of the spectrum, which is mainly due to energy loss in passing through heavy water and aluminum windows. The proton spectrum extends down to 1 MeV, below which nearly no protons are tallied. Such spectra indicate the proton beam does not suffer too much energy loss when penetrating the double entrance windows. The integral of the differential proton spectra in FIG. 6.12(a) reveals an approximate total proton flux of 1.59 x 10^{14} p/cm^{2}s per mA for both the inner and the outer entrance window with slightly higher value for the inner window. The inner entrance window gains more secondary protons from the reaction with spallation neutrons.

FIG. 6.12(b) shows the same case for the differential neutron fluxes. The curves are similar to those for differential neutron flux spectra in FIG. 6.10(b). However, in FIG. 6.12(b) the curve for the differential neutron flux has a slope of –1 in the ln-ln scale through out the spectrum instead of 2 slightly different slopes for the curves in FIG. 6.10(b). It indicates that [55] : $\phi' = \frac{\phi_0}{E}$, where ϕ' is the differential neutron flux, ϕ_0 is a constant and E is the neutron energy. Therefore the flux of neutrons with energies between E_1 and E_2 is given by

$$\phi(E_1,E_2) = \phi_0 \ln(E_2/E_1) \qquad (6.5)$$

As a matter of fact, as observed in FIG. 6.9(b) the lowest tips of the double entrance windows are locate at a position about 13 cm from the target rods where spallation

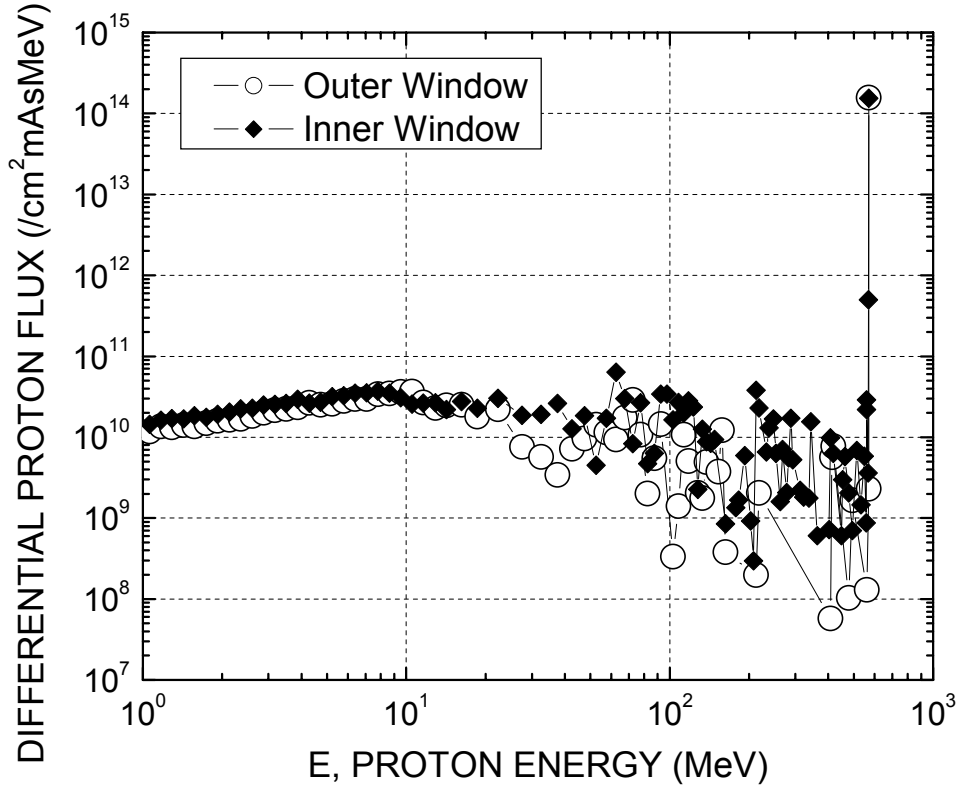

(a)

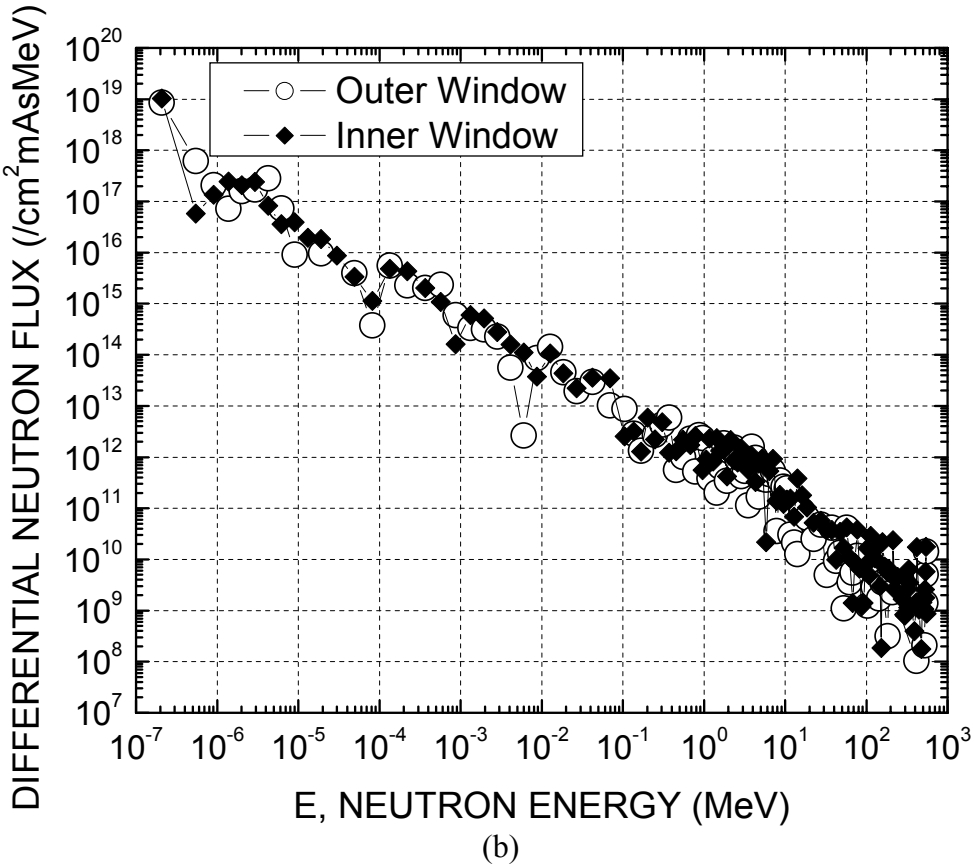

(b)

FIG. 6.12 (a)Proton and (b)neutron differential flux spectra at the centers of specimen rods for Beam 2.

neutrons are produced with heavy water follows between. The differential neutron spectra in FIG. 6.12(b) are actually a result of moderation by the heavy water, which reminds the similar differential neutron flux in the reactor. Although the spectra in FIG. 6.12(b) look quite similar for the inner and outer entrance window, the integral results reveal the total neutron fluxes of 2.06×10^{13} and 1.61×10^{13} n/cm^{2}s per mA for the inner and outer window, respectively. The inner entrance window has approximately 30% higher total neutron flux than the outer window due to its closer position to the center of spallation reactions (red region in FIG. 6.9(b)).

FIG. 6.13(a) shows the proton fluences corresponding to 10 Ahr (2.25×10^{23} protons) of irradiation for Beam 2 at the inner and outer entrance windows. The proton fluences in FIG. 6.13(a) lie within angles of ± 30 degree in the XZ plane and of ± 45 ~ 60 degree in the YZ plane, which corresponds to about ±5 cm along X axis and ±8 cm along Y axis, respectively, from the origin as seen in FIG. 6.5(a) where OP_6=OP'_6=10.6 cm. Outside those ranges, the proton fluxes are negligible.

A similar plot is shown in FIG. 6.13(b) for the neutron fluences with small peaks at the center of the entrance windows. As shown particularly in FIG. 6.13(b), as the angle increases the fluences reach a minimum at about 30 degrees and then increase again with a further increasing angle. This small peak may be due to spallation neutrons produced in the aluminum window walls. The spallation neutron production is greatest at the center because the incident proton current density is greatest there. The increase of neutron fluences at angles greater than 30 degrees is probably due to the fact that the entrance window walls approach closer to the target rods at higher angles (FIG. 6.1). The height of the small peak is greater in the XZ plane than in the YZ plane due to the broadness of Y profile of source Beam 2. The

height of the small peak is also greater for the inner window than the outer one since the lower tips of the inner window gain more spallation neutrons.

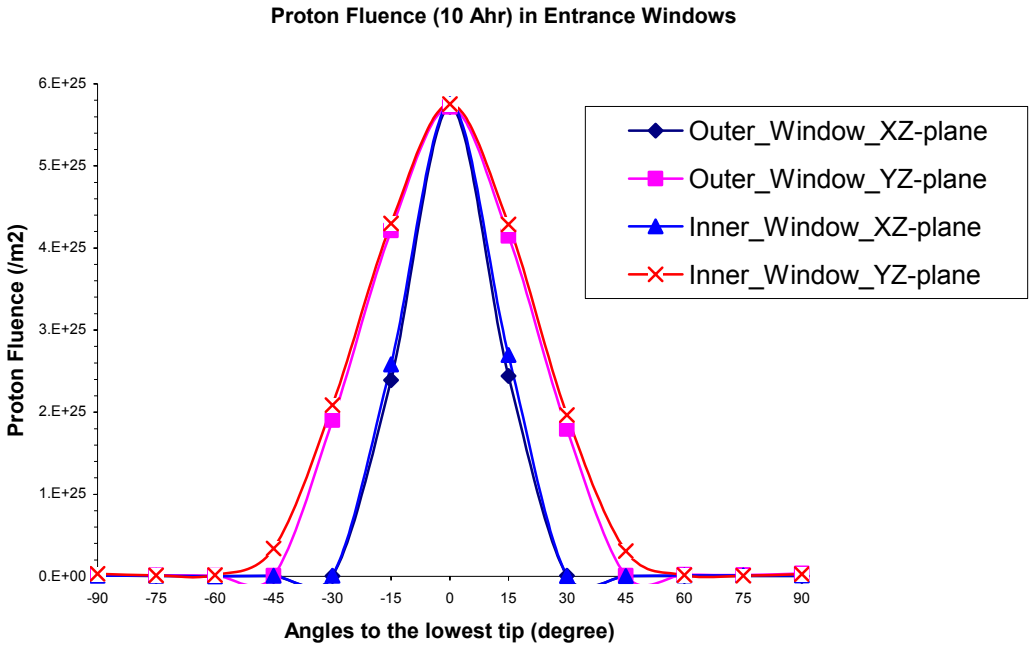

(a)

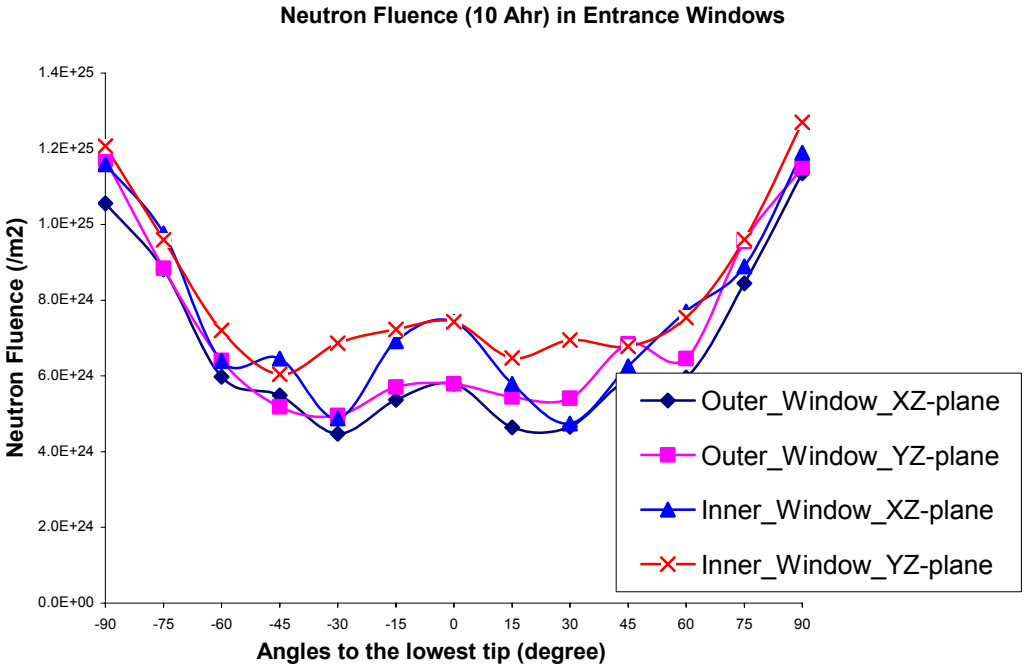

(b)

FIG. 6.13 (a) Proton and (b) neutron fluence after 10 Ahr of irradiation in the entrance windows Beam 2, incident proton energy, 570 MeV.

6.4 Cross sections

6.4.1 Cross section calculations

Radiation damage cross section data for four materials: Al6061, SS316, 9Cr-1Mo, and Zirc-4 are developed for the calculations. Al6061(Al + 1.13 wt% Mg +0.5 wt% Si) is very close to AlMg3 (Al + 2.72 wt% Mg), the material for the safety hull including both the double-layered entrance windows and tube. SS316 is the material for the external tubes of all the rods except the bottom layer rods. SS316 and 9Cr-1Mo are 2 types of stainless steels, representative for the stainless steel specimens in the specimen rods. Zirc-4 was the spallation target material in Target 3 (in STIP I). All of the four materials serve as checking points for the radiation damage to TARGET 5. Hence, it is important to evaluate their radiation damage cross sections. The evaluated cross section sources are preferred in the cross section developing, which include SPECTER [57] and ENDF VI [58] for neutron energies below 20 MeV and the recently developed LA150 [59] for neutron energies above 20 MeV and below 150 MeV, and proton energies from a few MeV to 150 MeV. For those elements among the compositions of the four materials whose cross sections are not found partially or completely in the above cross section sources, LAHET [31] calculations are used for the corresponding cross sections down to 20 MeV, although it is recognized that LAHET data may be unreliable at energies as low as 20 MeV.

FIG. 6.14 shows a friendly window program interface for the calculation of cross sections using LAHET/MCNPX. As a matter of fact, LAHET now is an incorporated part of MCNPX. The same calculations used LAHET before can be done in MCNPX. The program is coded in C++ language [60]. The integrated develop environment is Visual C++® [61] developed by Microsoft® Inc. The main goal of the programming is to save efforts in the painful preparing of MCNPX input

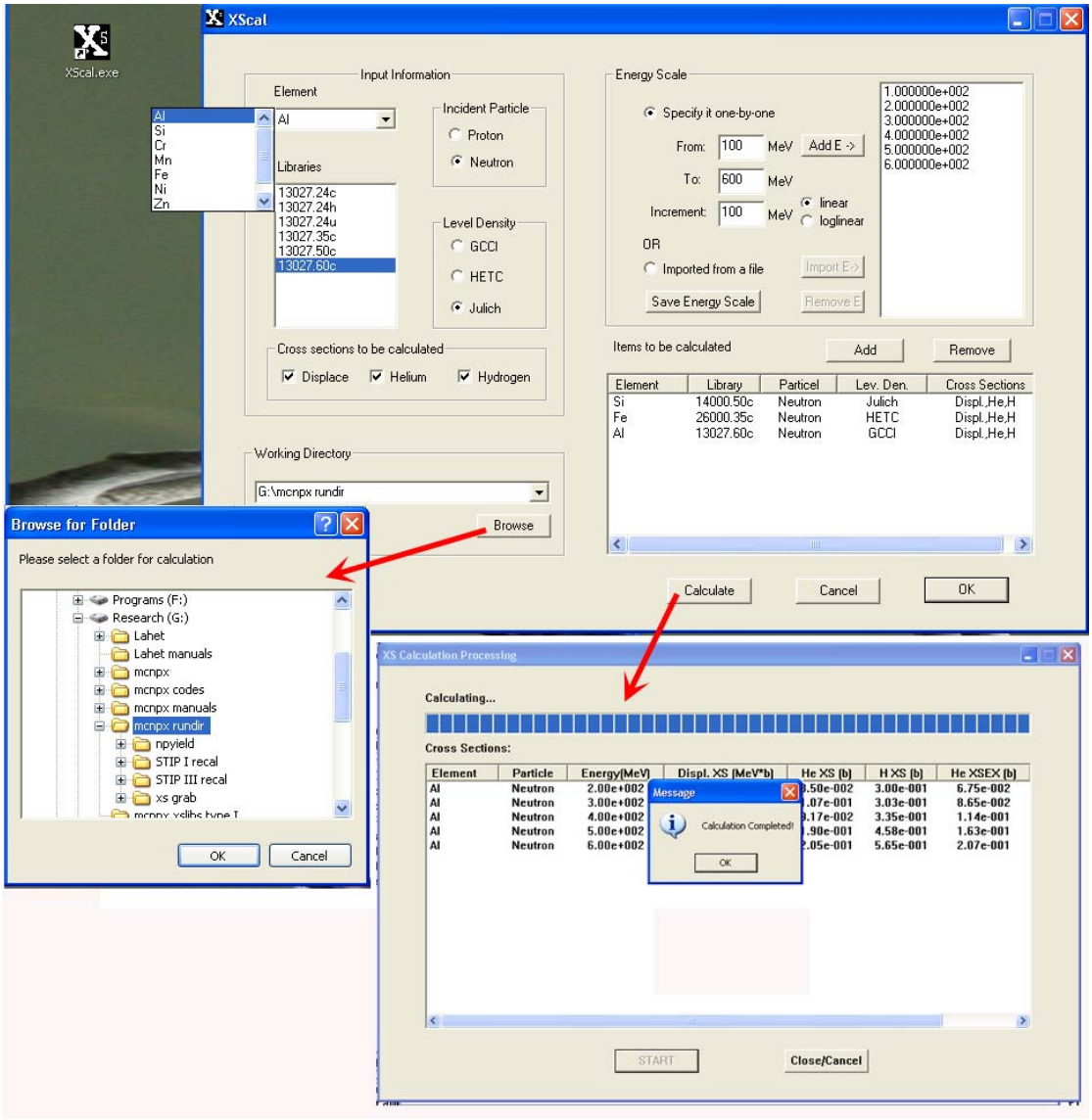

FIG. 6.14 Interfaces of the cross section calculation program: "XScal".

files, and grabbing and calculating results from the output files especially when there are many energy points. The input file for MCNPX contains lines of records, and has to be entered in a text format one-by-one according to the manual. In the cross section calculations, however, most of the records remain the same and only a few lines concerning the incident particle type and energy and the target material are different. Instead of preparing input files and entering execute commands one-by-one by hand tediously, a few clicks and presses in the program do all the work. The main

part of the coding is listed in the APPENDIX B. The code uses HTAPE [31] for the calculation of displacement cross sections, and both HTAPE and XSEX [31] for the calculation of helium and hydrogen production cross sections. The difference between the two methods is: HTAPE uses the recorded interaction information during the transportation of the particles; while XSEX forces the particles to interact with the target atoms without transporting them. The results from the two methods are listed in the final output for comparison.

The program works in windows systems. It can automatically detect MCNPX installed in the system and run it according to the system information of MCNPX. As shown in FIG. 6.14, the program has four parts in the main pop-up window. In the input section, the user may click an element and all of its cross section libraries installed in the computer are searched and listed. The user may choose a proper cross section library, an incident particle (only proton and neutron are programmed for the moment), the cross sections to calculate and the level density as an option. The user may specify an energy scale as instructed or simply import an energy scale from file in the energy scale section. Also the user may choose a working folder in the working directory section by browsing the directories of the hard drives in a folder browsing window prompted up after clicking the "Browse" button. The working folder is where the input and output for MCNPX, HTAPE and XSEX are generated, as well as the final results of cross sections. As shown in FIG. 6.14, in the bottom corner of the Xscal menu box there is a list of elements waiting in the calculation queue. The user may add or remove elements into or from the queue. The calculation progress is shown in the progress bar in another prompted up window after clicking the "calculate" button, and the results are listed as well.

6.4.2 Cross section analysis

FIG. 6.15 shows the neutron cross sections for the displacement, helium and hydrogen productions of Al6061 [62], SS316 [61], 9Cr-1Mo, and Zirc-4. All the neutron cross sections are from three sources in three energy E ranges: Range 1, E < 20 MeV, from SPECTER or ENDF VI; Range 2, 20 MeV < E < 150 MeV, from LA150; and Range 3, E > 150 MeV, from LAHET. The only exception is Zirc-4 at 20 MeV < E < 150 MeV, where the calculation results from LAHET are used due to the data absence in LA150.

As observed in FIG. 6.15, SS316 and 9Cr-1Mo have similarly-valued neutron cross sections for the radiation damage productions (displacement, helium and hydrogen), since they are both stainless steels and have similar concentrations of the major elements. Zirc-4 has displacement cross sections near those of SS316 and 9Cr-1Mo at energies below 20 MeV. However, Zirc-4 has much higher neutron cross sections at energies above 150 MeV. In FIG. 6.15(b), Al6061 has a peak for the helium production cross section at energies below 20 MeV which indicates that the contribution of neutrons to helium production within this energy region may be significant.

As mentioned above, we have attempted, where possible, to gather cross section information from three sources in three energy E ranges: Range 1, E < 20 MeV, from SPECTER or ENDF VI; Range 2, 20 MeV < E < 150 MeV, from LA150; and Range 3, E > 150 MeV, from LAHET. It can be seen in FIG. 6.15 that there are observable gaps or discrepancies in the cross section curves at the boundary between Ranges 1 and 2 at 20 MeV and at the boundary between Ranges 2 and 3 at 150 MeV. The gaps are particularly evident in the displacement cross sections at 20 MeV for Al6061 and Zirc-4 and in the helium and hydrogen cross sections at 150 MeV for

SS316 and 9Cr1Mo. They are artificial due to different cross section sources. Further work may be necessary to reduce or remove those gaps.

FIG. 6.16 shows the corresponding proton cross section curves. Unlike the neutron cross sections, LA150 does not contain displacement cross section for protons and SPECTER/ENDF does not contain any cross sections for protons. In FIG. 6.16(a), the displacement cross sections down to 20 MeV are calculated by LAHET. Below 20 MeV valuations by different authors are used. The evaluation of SS316 below 20 MeV by Barnett et al. in [63] was used, and others are adopted from James' cross sections in [56]. The vertical lines for Al6061 and SS316 in FIG. 6.16(a) indicate proton energies at which the displacement cross sections are evaluated to drop to zero. For the proton cross sections for helium and hydrogen production in 6.16(b) and 6.16(c), the LAHET calculation results are used down to 150 MeV. Below 150 MeV the LA150 data is used, which covers proton energies down to a few MeV. Zirc-4 is an exception since the evaluation from James [56] is used.

A similar peak of proton cross sections for the helium production of Al6061, as it appears in the neutron cross sections, is observed in the cross section curves of FIG. 6.16(b). Another interesting phenomenon is that at energies below 150 MeV for the helium and hydrogen productions the evaluated proton cross sections of Zric-4 are so close to the LA150 data of SS316 and 9Cr1-Mo. Although SS316 and 9Cr-1Mo are two types of stainless steel with common major compositions like Fe and Cr, Zirc-4 contains only 0.2 wt% of Fe and 0.1 wt% of Cr. This evaluation may be further examined by other means.

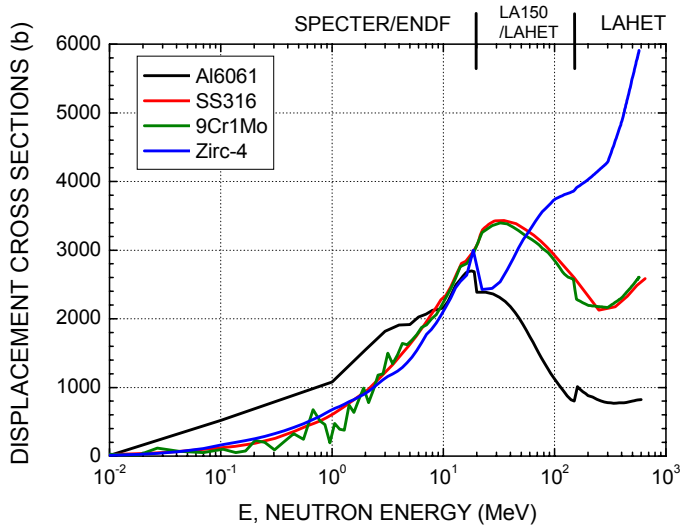

(a)

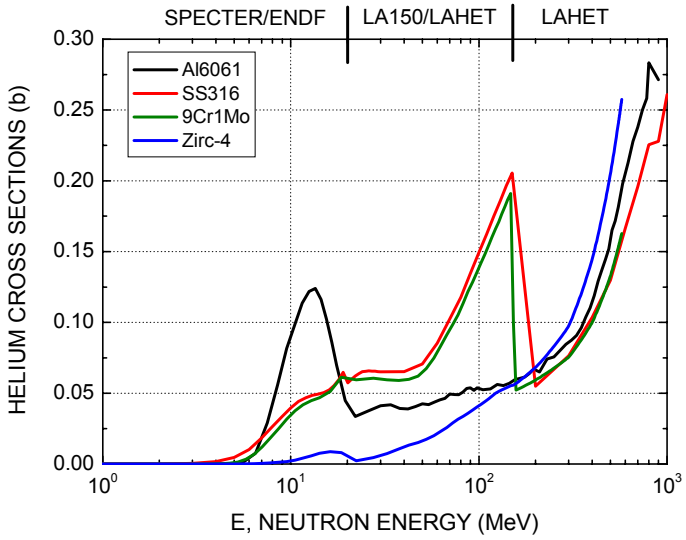

(b)

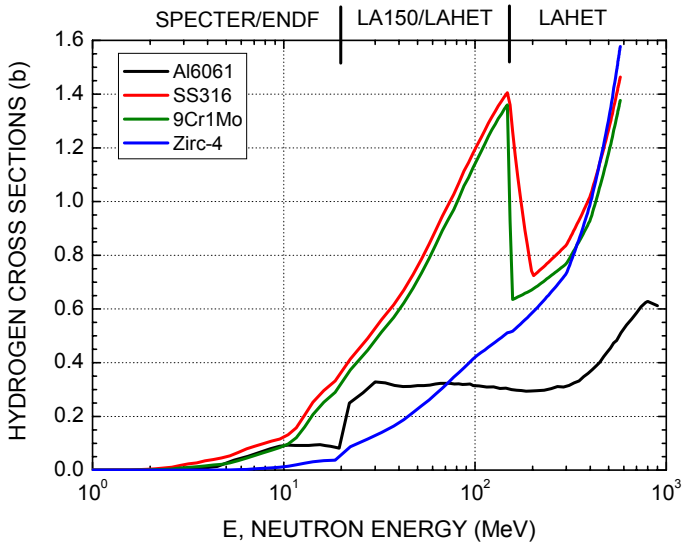

(c)

FIG. 6.15 Neutron cross sections for displacement (a), helium (b) and hydrogen (c) production of Al6061, SS316, 9Cr1Mo, and Zirc-4.

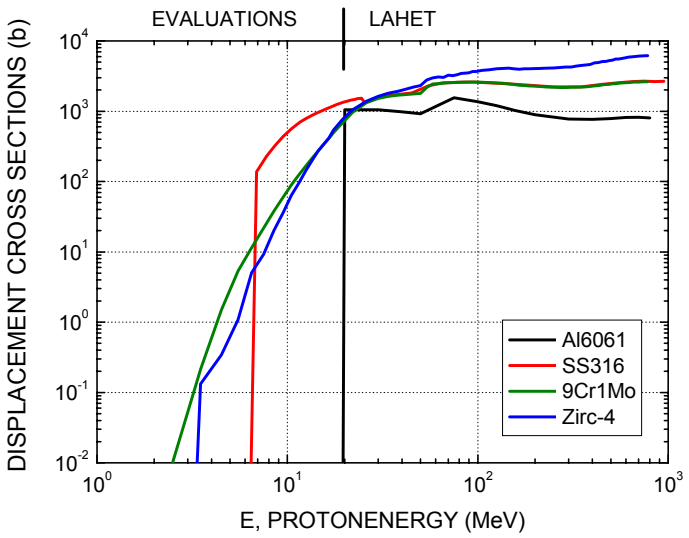

(a)

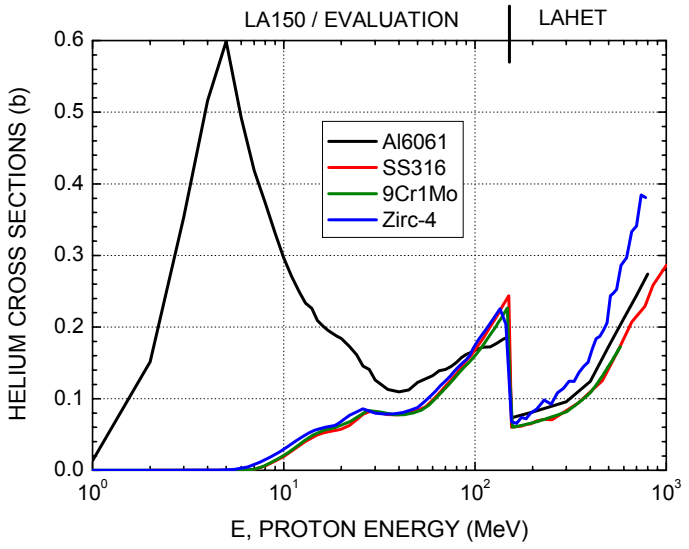

(b)

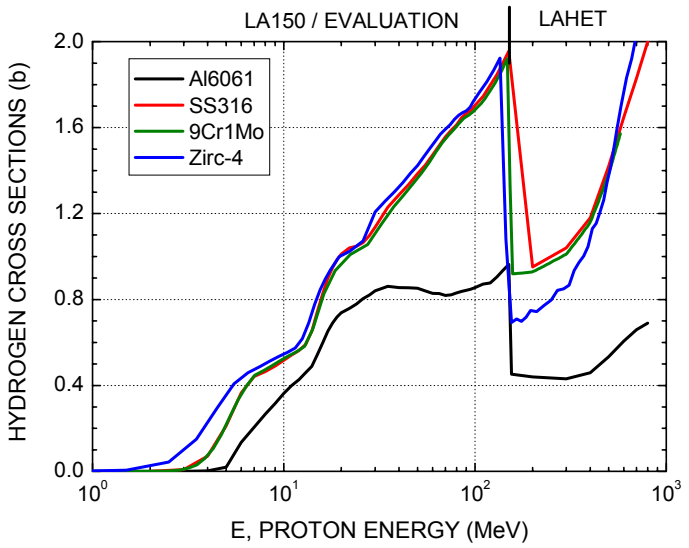

(c)

FIG. 6.16 Proton cross sections for displacement (a), helium (b) and hydrogen (c) production of Al6061, SS316, 9Cr1Mo, and Zirc-4.

6.5 Results of radiation damage productions

6.5.1 Radiation damage productions at the entrance windows

Upon the availability of proton and neutron fluxes and the cross sections, the radiation damage products, displacements, helium, and hydrogen, are calculated by folding the proton or neutron flux into the corresponding cross section as described in:

$$R = \int_0^\infty \Phi'(E)X(E)dE \qquad (6.6)$$

where R is the radiation product concentration, X(E) is the cross section at energy E, $\Phi'(E)$ is the corresponding differential fluence.

FIG. 6.17 shows displacement, helium, and hydrogen productions at the sampling points as described in FIG. 6.5(a) of the double entrance windows for Beam 2. The calculated productions assume an exposure of 10 Ah which is approximately the proton charge that Target 5 is to receive in STIP III. As indicated by the discussion in Section 6.3.3, the inner entrance window receives the same proton flux as the outer entrance window but more neutron flux due to the closer proximity to the source of spallation neutrons. Hence, there is slightly more radiation damage (displacement, helium and hydrogen) productions at the inner entrance window than at the outer entrance window.

If a comparison is made, we may observe that the shape of curves for the helium and hydrogen productions in FIGs. 6.17(b) and 6.17(c) mirrors the shape of curves for the proton fluences in FIG. 6.13(a). That is, the proton fluence dominates the contribution to helium and hydrogen production at the aluminum entrance windows. The larger proton fluence over the neutron fluence is one reason for this. The other reason lies in the neutron cross sections for the helium and hydrogen productions of Al6061, which drop to nearly zero for neutrons energies below a few MeV. But the cumulative neutron flux below a few MeV occupies the major part

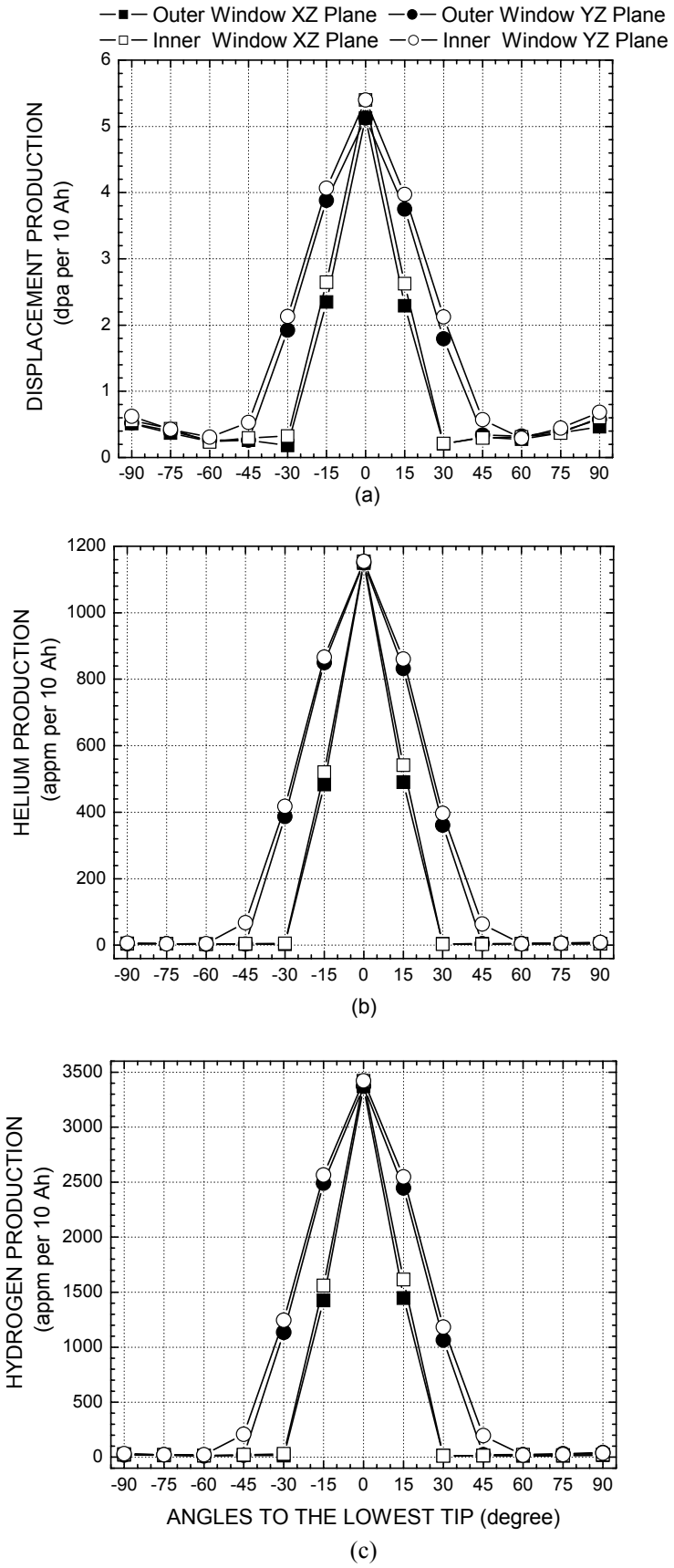

FIG. 17 Displacement, helium and hydrogen production in the entrance windows by Beam2 after 10 Ah exposure.

(more than 50%) of the total neutron flux (FIG. 6.15(e) in [56]). Such neutron cross section spectra further reduce the contribution from neutrons.

However, this is not the case for the displacement production. The shape of curves for the displacement production in FIG. 6.17(a) reflects, instead, the shape of curves for the neutron fluences in FIG. 6.13(b). The displacement production increases as the target rods inside the safety hull are approached, which indicates that Al6061 has higher cross sections for the displacement production due to the low energy neutrons.

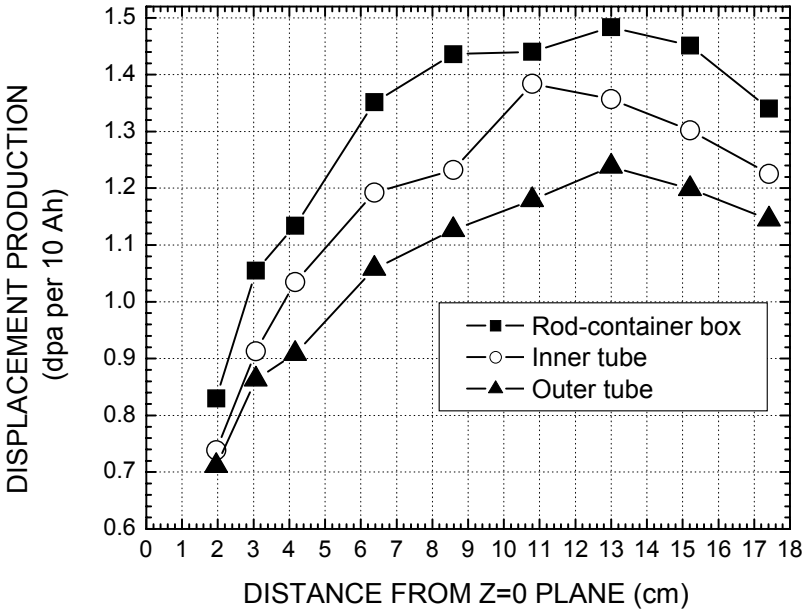

FIG. 6.18 Displacement production on the walls of the rod-container box and the double layered tube in YZ planes after 10 Ah irradiation by Beam 2 (Z=0 is where the double layered tubes mate the entrance windows, Z=18 cm is the 15th layer of rods).

It may be of concern to consider how displacement production varies as we move upward (parallel to +Z axis) along the walls of the safety hull. FIG. 6.18 shows displacement production versus distance from the Z=0 plane (FIG. 6.1) until the 15th layer from the bottom (Z=17.4 cm). The sampling method is similar to what FIG. 6.5(b) describes. Only the displacement productions in YZ plane are shown in FIG.

6.18 since as indicated in FIG. 6.8 the neutron flux has a wider profile along Y-axis, hence higher neutron flux at the same distance from where the peak neutron flux is located. As observed in FIG. 6.18, the displacement production may increase to about 1.5 dpa (assuming an exposure of 10 Ah).

As estimated, the highest radiation damage productions occur at the lowest tip of the entrance windows. TABLE 6.4 listed their displacement, helium and hydrogen productions due to proton fluence, neutron fluence, and both of them. It reveals the highest radiation damage production of 5.4 dpa, 1150 appm He and 3400 appm H at the inner entrance window.

TABLE 6.4 Displacement, helium, and hydrogen at the lowest tips of entrance windows, Beam 2, incident proton energy, 570 MeV, 10 Ahr of irradiation.

Outer Window			
	Neutron	**Proton**	**Total**
Displ. (dpa)	0.5	4.6	5.1
He (appm)	7	1143	1150
H (appm)	24	3348	3372
Inner Window			
	Neutron	**Proton**	**Total**
Displ. (dpa)	0.7	4.7	5.4
He (appm)	15	1140	1155
H (appm)	49	3372	3421

The insignificant contribution of neutrons to the helium and hydrogen production is as explained earlier in this section. The contributions of neutrons at different energies to displacement production are analyzed in FIG. 6.19 for the lowest tip at the inner entrance window, which shows about 75% of the displacements due to neutrons stem from neutrons of energies below 20 MeV, 20% due to neutrons from 20 to 150 MeV, and 5% from 150 to 570 MeV [55]. Such significant contribution from neutrons of lower energies explains the shape of the curves in FIG. 6.17(a).

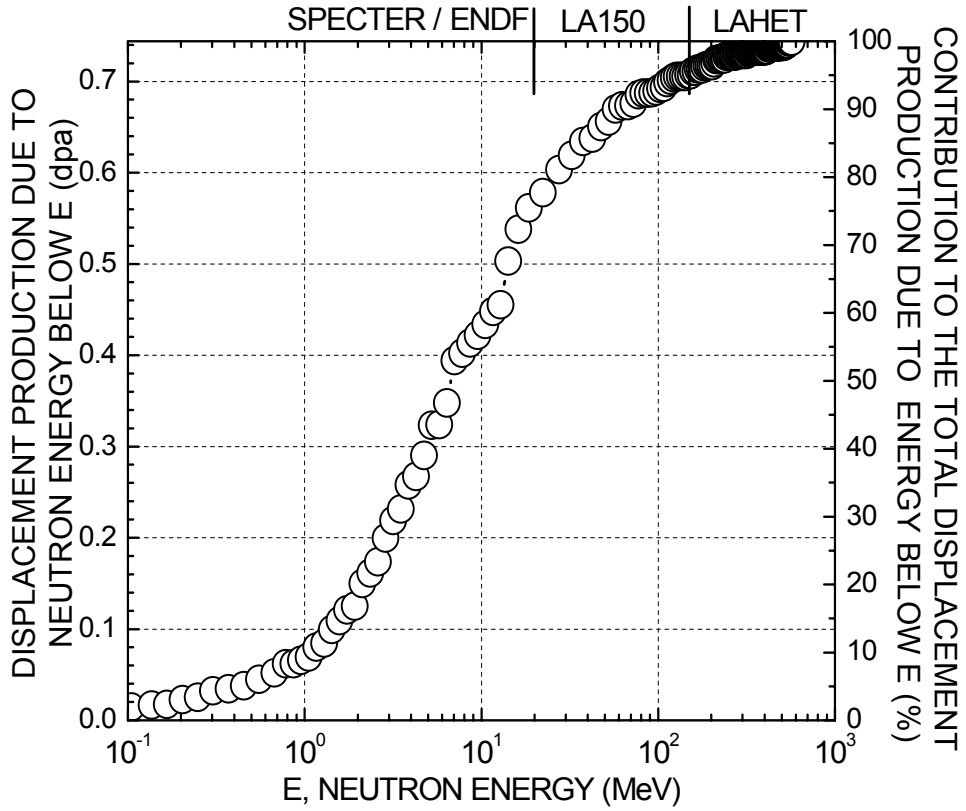

FIG. 6.19. Cumulative displacement production in aluminum due to neutron flux at the inner entrance window after 10 Ah exposure.

6.5.2 Radiation damage productions at the specimen rods

The radiation damage calculation at the specimen rods assumes SS316, Al6061, 9Cr-1Mo and Zirc-4 distributed all over the specimen rods. Due to the huge amount of data, only the partial results of SS316 are presented here. The similar data for Al6061, 9Cr-1Mo and Zirc-4 can be found in APPENDIX A. More detailed data can be found in [56]. FIG. 6.20 shows the displacement, helium, and hydrogen

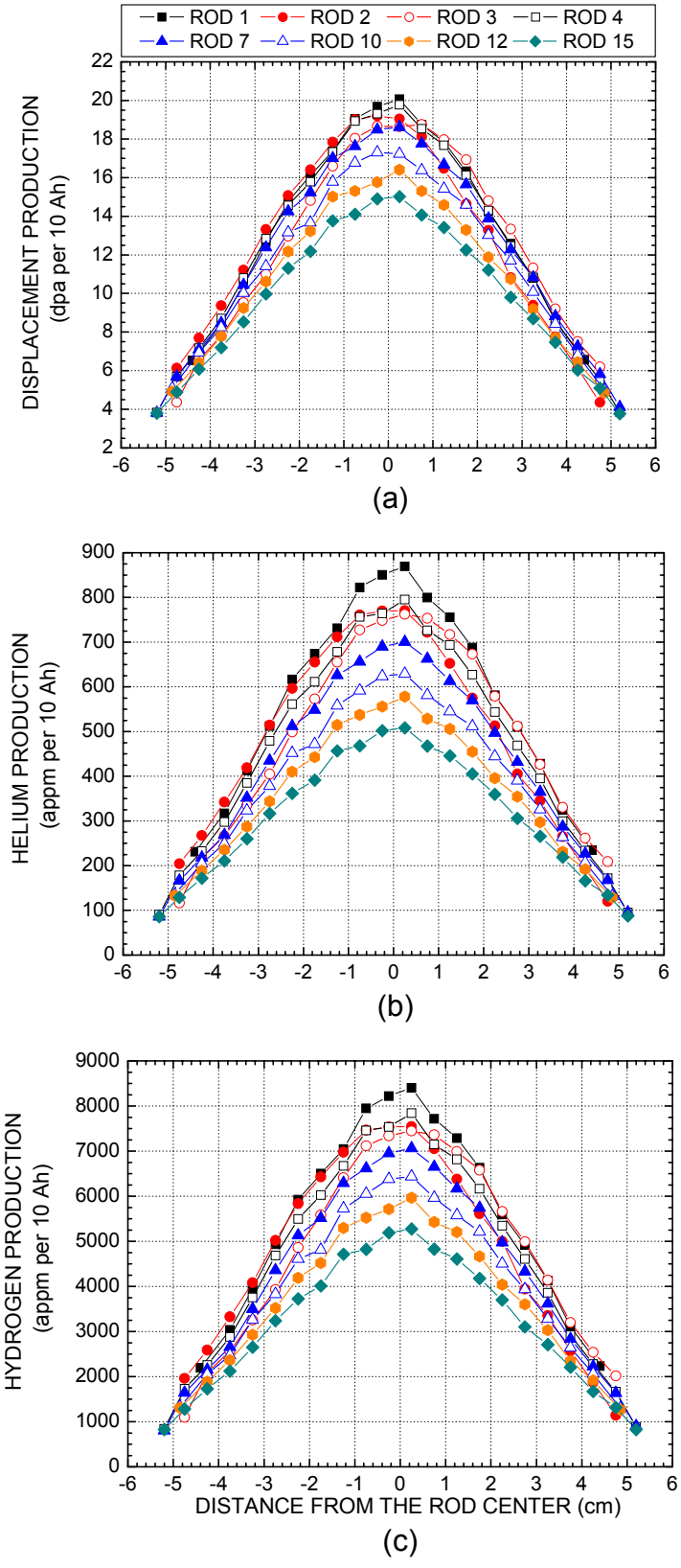

FIG. 6.20 Displacement, helium, and hydrogen productions at SS316 rods , Beam 2.

productions on the major central rods of SS316 for Beams 2 (assuming an exposure of 10 Ah).

As an item of interest FIG. 6.20 is compared to the corresponding proton and neutron fluence plots as shown in FIG. 6.11. The ordering of curves in FIG. 6.20 mirrors the ordering of curves for the proton fluence in FIG. 6.11(a). In other words, it is the proton fluence that is the controlling factor for radiation products. Such a phenomenon is due to the multiplication of cross section spectrum and fluence spectrum, as indicated in Eq. (6.6).

TABLE 6.5 Displacement, helium and hydrogen productions at the center of specimen rods of SS316, Beam 2,10 Ahr of irradiation.

SS316 Rods	Displacement			Helium			Hydrogen		
	Neutron (dpa)	Proton (dpa)	Total (dpa)	Neutron (appm)	Proton (appm)	Total (appm)	Neutron (appm)	Proton (appm)	Total (appm)
Rod1	7.3	12.5	19.9	114	746	860	924	7385	8309
Rod2	7.8	11.3	19.1	121	649	770	991	6549	7540
Rod3	7.5	11.1	18.7	117	638	755	952	6441	7393
Rod4	8.0	11.5	19.5	129	650	780	1061	6626	7687
Rod5	7.8	10.2	18.0	123	555	678	1006	5775	6781
Rod6	7.8	10.1	18.0	123	550	673	1004	5728	6732
Rod7	7.9	10.7	18.6	126	569	695	1037	5970	7007
Rod8	8.4	9.2	17.6	126	475	601	1036	5069	6105
Rod9	8.4	9.2	17.5	126	471	597	1030	5025	6055
Rod10	7.3	9.9	17.3	119	508	626	979	5429	6408
Rod11	6.8	8.4	15.3	105	424	529	876	4555	5431
Rod12	6.9	9.2	16.1	111	456	567	922	4918	5840
Rod13	6.4	7.8	14.2	101	379	480	839	4090	4929
Rod14	6.8	7.7	14.4	109	372	481	908	4044	4952
Rod15	6.6	8.4	15.0	105	401	505	870	4361	5231
Rod16	2.6	0.3	2.9	34	16	50	282	167	449
Rod17T91	2.9	0.4	3.3	39	21	60	317	229	547
Rod17EU97	2.6	0.3	2.9	34	16	50	275	169	445

For further explanation, TABLE 5 lists the neutron and proton contributions to radiation damage production for SS316 at the central segment of specimen rods. Since the peak neutron flux is found at its central position as indicated in FIG. 6.9(a), Rod 7 serves as a good example for illustrating how the maximum neutron contribution to the radiation damage production could be. As found in TABLE 5, the displacement, helium and hydrogen productions at the center of Rod 7 are 18.6 dpa, 695 appm and 7007 appm, respectively. The neutron contributions for the productions are, respectively, 42%, 18%, and 15%. The small contribution from neutrons to the gas productions can be attributed to the extremely lower neutron cross sections at the lower energies (below 20 MeV) where lie the major neutron fluxes, similar to the case of entrance windows. Neutrons make a larger contribution to displacement production though still less than the contribution from protons. FIG. 6.21 shows the cumulative displacement concentration in 316SS at the center segment

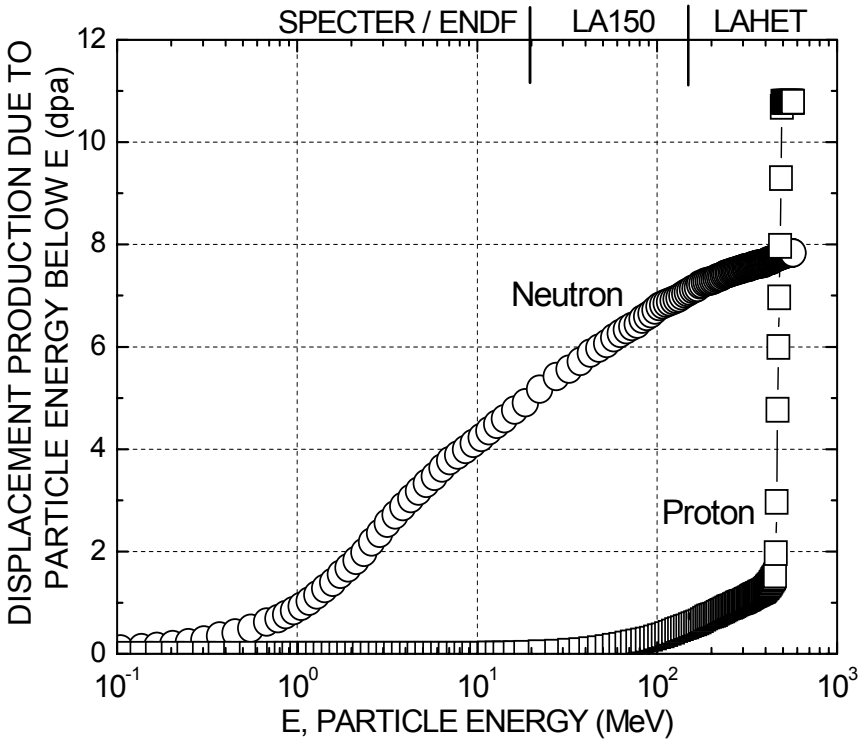

FIG. 9.21. Cumulative displacement production in SS316 at the center segment of Rod 7 after 10 Ah exposure.

of Rod 7 after 10 Ah exposure as a function of neutron and proton energies. For the protons, about 95% of the displacements are due to protons of energies above 150 MeV. For the neutrons, 63% of the displacements are due to neutrons of energies below 20 MeV, 26% due to neutrons in the range 20 to 150 MeV, and 11% from 150 to 570 MeV [55]. The low energy neutrons again play an important role in the displacement production.

The results for the more focused Beam 1 are not presented here. However, due to the characteristic profile of Beam 1, the radiation damage productions along the central axis of Target 5 (Z-axis), which includes the central specimen rods and the lowest tip of the entrance windows, are about 10–20% higher for Beam 1 than for Beam 2.

6.6 Summary and conclusions

The calculation of radiation damage to Target 5 involves geometry modeling, flux analysis and cross section development. The results of radiation damage production consist of two parts: (1) products at the entrance windows for monitoring the capacity of safety hull, and (2) products at the specimen rods for assisting further experiments. Some conclusions may be summarized as follows:

(1) The geometry modeling is consistent with Target 5 as actually built with some simplifications ~~to help~~ to improve the calculational efficiency without affecting significantly the outcome of the calculations.

(2) Target 5 is a lead spallation target bearing similar characteristics of its preceding targets. It contains layers of rods filled with spallation material, lead, among which specimen rods containing samples for the irradiation are interspersed.

(3) Two beams are used in STIP III: Beam 1 is a measured profile with 575 MeV incident protons; Beam 2 is a truncated double-Gaussian profile with 570 MeV incident protons. Only the results of Beam 2 are presented.

(4) Proton flux decreases as the proton beam travels further into Target 5 since the secondary protons produced in spallation reactions make a negligible contribution to the total proton flux. Neutrons are a different case, since they are mostly produced in spallation reactions. The peak of neutron flux is reached around the central position of Rod 7 and decreases along the radial distance from there.

(5) The proton and neutron flux profiles follow the pattern of the source beam in that the distribution is wider ~~at~~ in the YZ plane than in the XZ plane.

(6) At the entrance windows, the proton flux spectrum is dominated by the flux at the energy of source beam. The neutron flux spectrum, however, is dominated by the lower energy neutrons. The proton flux largely overwhelms the neutron flux. However, in the center of where spallation reactions occur most, the neutron flux due to all neutron energies outweighs the proton flux.

(7) The cross sections are developed and calculated based on three sources: SPECTER/ENDF, LA150 and LAHET. A program is made to make the calculation of cross section convenient. Further work may be done on the cross sections which are not covered by any of the above sources.

(8) The lowest tips of the entrance windows receive the highest proton flux~~es~~, and therefore experience the greatest radiation damage. The inner window receives slightly higher radiation damage than the outer window due to the neutrons from spallation reactions. The highest radiation damage productions are found at the lowest tip of the inner entrance window, which are approximately 5.4 dpa, 1200 appm

He, and 3400 appm H, compared to 18.6 dpa, 700 appm He, and 7000 appm H at the center of Rod 7 which receives the highest neutron flux.

(9) Protons have dominant contributions to the radiation damage productions in most cases due to the multiplication of cross section spectrum and flux spectrum. However the contribution from neutrons to the displacement productions can not be ignored since the displacement cross sections at the lower neutron energies, where lies the major neutron flux component, are large.

(10) Due to the focused profile of Beam 1, the results, though not presented, show a 10-20% higher value of fluxes and displacement and gas productions than is the case for Beam 2.

Chapter 7

Analysis and discussions

7.1 New method in the calculations

The calculations of radiation damage discussed in Chapter 6 are performed in a traditional manner, which folds the proton and neutron fluxes into corresponding cross sections for radiation products as displacement, helium and hydrogen, as shown in Eq. 6.6. However, the use of cross sections may be complicated due to their availability in various cross section sources and the validity of the cross section sources. In addition, the calculation of the cross sections within a given energy bound may, sometimes, be questionable. As discussed in Chapter 6, three cross section sources, SPECTER/ENDF, LA150 and LAHET, are used in the calculations for the radiation damage production cross sections. For proton and neutron energies above the upper limit of LA150 (or SPECER/ENDF when LA150 cross sections are not available), LAHET is used to calculate the cross sections. In running LAHET in order to obtain the cross sections, a synthetic target (usually a right-circular cylinder with thickness in the beam direction of about 0.1 cm) is assumed. The calculation method is described in Section 2.3. This method of cross section calculation is suitable in most cases. However, it introduces some inaccuracy into the calculation due to the difference between the synthetic target and the actual practical target. For example, the thickness of the synthetic target may be

a factor affecting the accuracy of the calculation. If the synthetic target is too thin, the radiation product may leave the target resulting in lower apparent cross sections. Otherwise, if it is too thick (i.e. if the thin target theory is violated), the calculated cross sections would not be representative of a single given energy.

Therefore a new method is proposed to calculate radiation damage productions without explicitly involving damage cross sections. To distinguish from the conventional method quoted as Method 1 hereafter, the new method is quoted as Method 2, which takes advantage of the interaction information recorded in Monte Carlo simulation. In Method 2, the damage cross sections are not explicitly determined and no synthetic sample is assumed. Instead, the actual modeling of a practical system is specified in the MCNPX input file. Then all the interactions in the relevant tally volumes are recorded into a HISTP [31] file. The HISTP file can later be extracted by HTAPE [31] using specified options for displacement, helium and hydrogen productions. The difference of Methods 1 and 2 are described in the flow chart of FIG. 7.1.

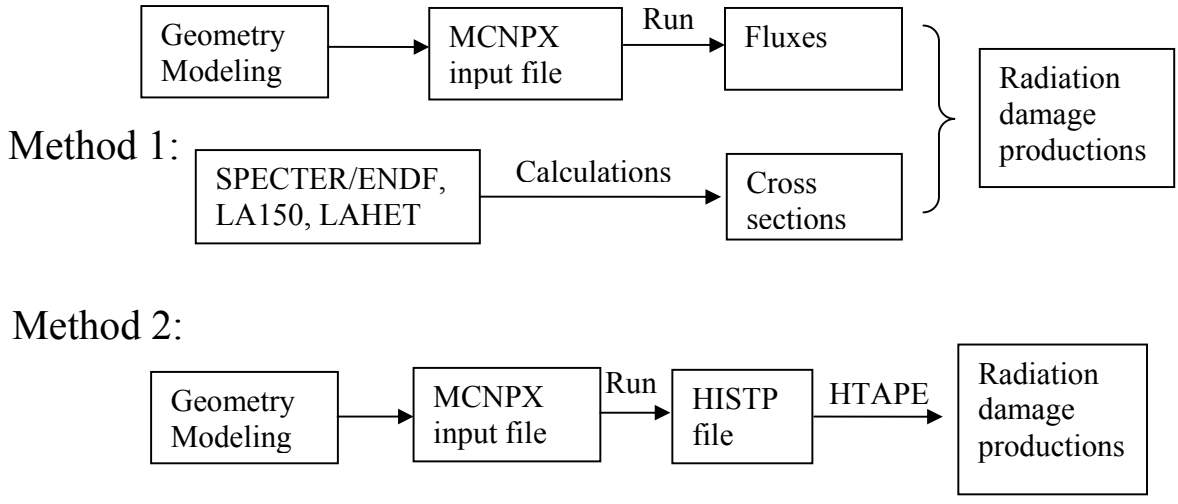

FIG. 7.1 The flow charts for procedures of Methods 1 and 2.

Method 2 was used to calculate the radiation damage productions at the lowest tip of the outer entrance window in Target 3 used in STIP I, which is the first phase of SINQ Target Irradiation Program. Target 3, as shown in FIG. 7.2 [4], bears similar characteristics as Target 5. But Target 3 uses zircaloy as the spallation target material and its rod container has a hexagonal shape instead of a square shape as in Target 5. Target 3 received a proton charge of 6.8 Ah in STIP I. TABLE 7.1 shows the comparison of the calculation results for Methods 1 and 2. The sampling method on the entrance windows is similar to FIG. 6.5(b) described in Section 5.1.3. As observed in TABEL 7.1, at an incident proton number of 10^6, the statistical error for Method 1 is 2%, however the error for Method 2, as indicated in the row of Method 2A in TABEL 7.1, stays around 15% to 30 %. Only when the incident proton number is increased to 10^7 in Method 2B, the error is close around 5% to 10%. We may conclude that Method 2 requires much greater computer capacity than Method 1. As the calculation time for a number of 10^7 incident protons can not be tolerated, only a portion of Target 3 was used in the calculation. The outcome of the approximation is quite reasonable since the entrance windows are away from the center of spallation reactions.

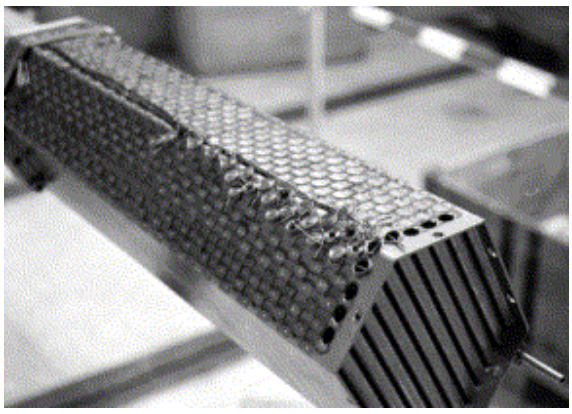

FIG. 7.2 A photo of Target 3 [4].

TABLE 7.1. Summary of radiation damage productions at the lowest tip of outer entrance window in Target 3 for STIP-I after an exposure of 6.8 Ah.

	DISPLACEMENTS (dpa)	HELIUM (appmHe)	HYDROGEN (appmH)
Method 1, 1E6 p's	3.6 (2%)	770 (2%)	2700 (2%)
Method 2A, 1E6 p's	2.8 (15%)	1140 (27%)	3200 (17%)
Method 2B, 1E7 p's	2.9 (5%)	730 (10%)	2700 (6%)

The results from Method 2B (10^7 protons) are very close to those from Method 1 (10^6 protons) for helium and hydrogen production. For helium, Method 2B and 1 give 730 appmHe and 770 appmHe, respectively. For hydrogen, both Methods 2B and 1 give 2700 appmH. The displacement production is 2.9 dpa from Method 2B and 3.6 dpa from Method 1. The difference between the two methods is relatively large. The reason lies in the fact that the interaction information for neutron energies below 20 MeV is not recorded into HISTP file. The previous discussion in Section 6.5.1 reveals that at the lowest tip of the entrance windows the neutrons of energies below 20 MeV, contribute 75% to the displacement production due to neutrons of all energies, as shown in FIG. 6.19. Since the total neutron-produced displacement concentration at the inner entrance window is 0.7 dpa as shown in TABLE 6.4, the missing neutron-produced displacement concentration is 0.7 x 0.75 = 0.525 dpa, and therefore the missing displacement concentration is about 10% of the displacement production due to protons and neutrons of all energies. Hence, the contribution from neurons of energies below 20 MeV to the displacement production may not be negligible, and plays a part in explaining the reduced displacement production in Method 2B. This problem of HISTP recording is summarized as the "mixed and match" problem [64] by MCNPX development group due

to the combination of two differently styled codes: MCNP and LAHET. The problem will be fixed in the future version of MCNPX [65].

Method 1 offers flexibility in the selection of cross sections. It, however, also involves the inaccuracy and pain in calculating and selecting cross sections. Compared to Method 1, Method 2 is easy to use and accurate without the extra trouble of calculating cross sections, but it requires greater computer capability and a fix of the MCNPX code. However, as the computers are getting faster and faster and MCNPX code is getting better, Method 2 is becomes promising.

7.2 Errors and accuracy of the calculations

7.2.1 Errors due to cross sections

The reliability and accuracy of the radiation damage calculations are usually questioned as to how close they are to the real case. An analysis is quite necessary to determine the uncertainty the calculations results. It, however, is difficult to perform a direct error analysis since there are various error sources. The main error sources in our calculations may be as described as follows:

(1) Error in the physics models for the particle interactions and transportation. Most of the physics models for the spallation reaction are described in Chapter 3. The accuracy of the models has been examined by either experiments or analysis as noted in Chapter 3. The physics models are the basis of our calculations, but it is beyond the scope of the dissertation to discuss their accuracy.

(2) Error in the Monte Carlo simulations. This type of error is given as statistical error in the output file of MCNPX, the major Monte Carlo code we used in the calculations. Our

calculations show that such error for the most part is not greater than 5%, which is an acceptable error limit for most of engineering problems.

(3) Error in the physics data. The physics data include the parameters of the physics models and the cross sections. As most of the physics model parameters are recommended by the MCNPX code, the remaining uncertain part is the cross sections.

The uncertainty of the cross sections may come from two sources: (1) errors in the evaluations, and (2) the difference of working conditions between the evaluated cross section data and the practical system environments such as temperature. Most of the cross sections are evaluated at room temperature, but the working temperature like in Target 5 ranges from 80 C to 550 C as discussed Chapter 4. The sensitivity of cross sections due to the temperature may be not quite significant in the common working environments [65], but it introduces error into the calculations. The cross section uncertainty analysis is necessary for revealing part of the uncertainty in the radiation damage production calculations.

Cross sections are used in the calculations first in the Monte Carlo simulation of the particle transport for obtaining the particle fluxes, then in the calculations of radiation damage productions, where the particle fluxes are folded into corresponding cross sections. For the later scenario, the uncertainty of the radiation damage productions is proportional to the uncertainty of the cross sections. It remains unknown how the uncertainty of the cross sections may affect the results in the first scenario.

The perturbation card (PERT card) [30] of MCNPX is used for exploring the effects of uncertainty of the cross sections. The PERD card allows perturbation in cell material density, composition and reaction cross section data. The perturbation analysis uses first and second order differential operator technique [66]. The PERT card is only

suitable for the cross sections below the upper limit of the cross section libraries, in our case, 20 MeV for neutrons. Since no proton cross sections in LA150 were used in our calculation for the fluxes due to the "mixed and match" problem, no analysis for the uncertainty of proton cross section is made here. Therefore, the uncertainty analysis of cross sections is made in Target 5 only for neutrons of energies below 20 MeV.

The total cross sections for Al, the structural material of Target 5, and Pb, the spallation material of Target 5, are perturbed for analysis by changing the densities of the two materials since the macro cross sections are proportional to material atomic densities. The displacement productions at the lowest tip of the inner entrance window and the central segment of Rod 7 are watched. At both locations pervious discussion in Chapter 6 reveals that neutrons of energies below 20 MeV contribute 60-75% of displacement productions due to neutrons of all energies. TABLE 7.2 shows the perturbation of displacement productions in percentage due to changes of mass densities of Al and Pb. The minus symbol means decrease of the densities, and the plus symbol means increase.

TABLE 7.2 The perturbation of displacement production due to neutrons of energies below 20 MeV in percentage versus the change of densities of spallation material, Pb, and structure material, Al.

	Displacement production change in percentage				
Pb Density change %	**-90%**	**-75%**	**-50%**	**50%**	**100%**
Rod 7	-3.22	-2.65	-1.74	1.63	3.14
Inner Window	1.31	1.05	0.66	-0.49	-0.81
	Displacement production change in percentage				
Al Density change %	**-90%**	**-75%**	**-50%**	**50%**	**100%**
Rod 7	-0.31	-0.26	-0.17	0.17	0.33
Inner Window	-1.31	-0.97	-0.52	0.00	-0.52

As observed in TABLE 7.2, the displacement productions due to neutrons of energies below 20 MeV are not sensitive to the cross section changes of Pb or Al via density changes. A 90% decrease or a 100% increase of the density of the spallation material, Pb, results only a 3% change of displacement productions at Rod 7. The fluctuation of the neutron spectrum, increasing flux at one part and decreasing flux at another part, may be a factor in canceling the effects of cross section changes. Compared to the results from the cross section change of Al, the displacement productions at both locations are more sensitive to the cross section changes of Pb due to the role of Pb in producing neutrons as spallation target material.

The above analysis is made upon the cross section changes of one material at one time. However, in a large system the effects of cross sections of several materials in combination may take place, which further complicated the analysis. A better way to examine the radiation damage production calculation results is through the experimental data as discussed in next section.

7.2.2 Comparison to the experimental data

Although the displacement production can not be measured by the experiments yet, the helium and hydrogen production can be measured with satisfying precision. In the measurement, the specimens are heated to about 1200 C and the helium or hydrogen retained in the specimens is extracted and then measured by the mass spectrometer detector [66-67]. The measurement of helium and hydrogen productions of specimens irradiated in STIP I (the irradiation of STIP III has not finished yet) were performed at Pacific Northwest National Laboratory (PNNL). The data of the measurement were reported in [68]. TABLE 7.3 lists the calculated results and experimental measurement for the aluminum specimens. The measurement was done on the duplicated specimens

and only the mean values are presented in TABLE 7.3. The uncertainty of the helium measurement is about 1% for greater than 10^{11} helium atoms [66]. The uncertainty of the hydrogen measurement is estimated as about 20% [67]. The positions of the specimens during irradiation are also specified in TABLE 7.3, and the organization of the specimen rods is shown in FIG. 7.3.

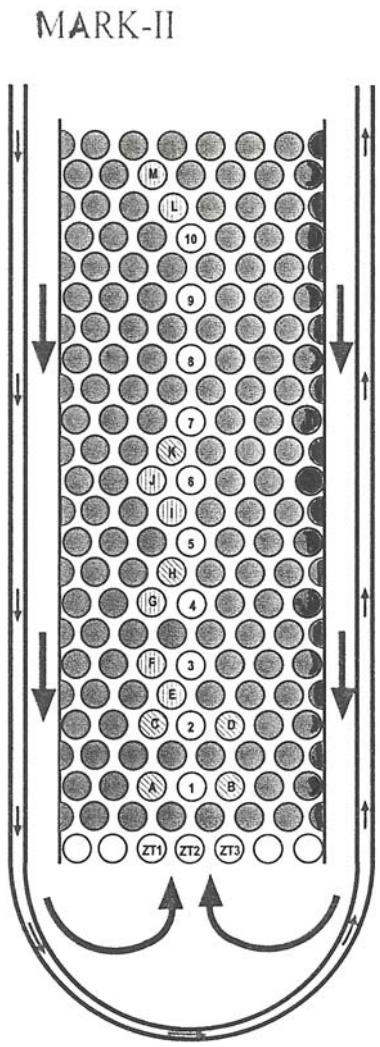

FIG. 7.3 A Schematic diagram of Target 3.

TABLE 7.3. Comparison of calculation results and experimental data for helium and hydrogen production in Target 3 after an exposure of 6.8 Ah.

Material	Position	Helium (appm)		Hydrogen (appm)	
		Calc.	Meas.	Calc.	Meas.
Al	Rod 6, center	350	520	1310	1300
Al	Rod 5, 5.5 cm from center	150	187	540	775
AlMg3	Lowest tip of outer window	770	1125	2700	1900

As observed in TABLE 7.3, the discrepancy remains (up to about 40% of the measured data) between the calculations and the measurement for the helium and hydrogen productions. The calculated hydrogen productions agree relatively well with the measured data if errors from both sides are accounted.

7.3 Analysis of the calculation results

7.3.1 STIP I and STIP III comparison

Target 3 and Target 5 are respectively used in STIP I and STIP III. The spallation target materials are Zircaloy-2 for Target 3 and lead for Target 5. However, the two targets have very similar characters in the structure design and the specimen rods configuration. In addition, the incident proton beams onto Targets 3 and 5 are basically the same. Therefore, a comparison of the two targets may help the evaluation of the target design.

A mesh tally of MCNPX was conducted along the beam direction (Z-axis, X=Y=0) in Targets 3 and 5 to explore the spatial distribution of the proton and neutron fluxes. FIG. 7.4 presents the proton flux distribution along beam direction, starting from the lowest tips of entrance windows (Z = -11 cm) until the highest layer of target rods (Z = 44 cm). Since the contribution of the secondary protons from spallation reactions to the

total proton flux is generally small, the two curves look quite similar at the lower part of the targets (Z < 25 cm). At the higher part of the targets (Z > 25 cm), Target 3 has a higher proton flux than Target 5 due to the poorer shielding capacity of zirconium as compared to lead. The secondary proton does have observable contribution to the total

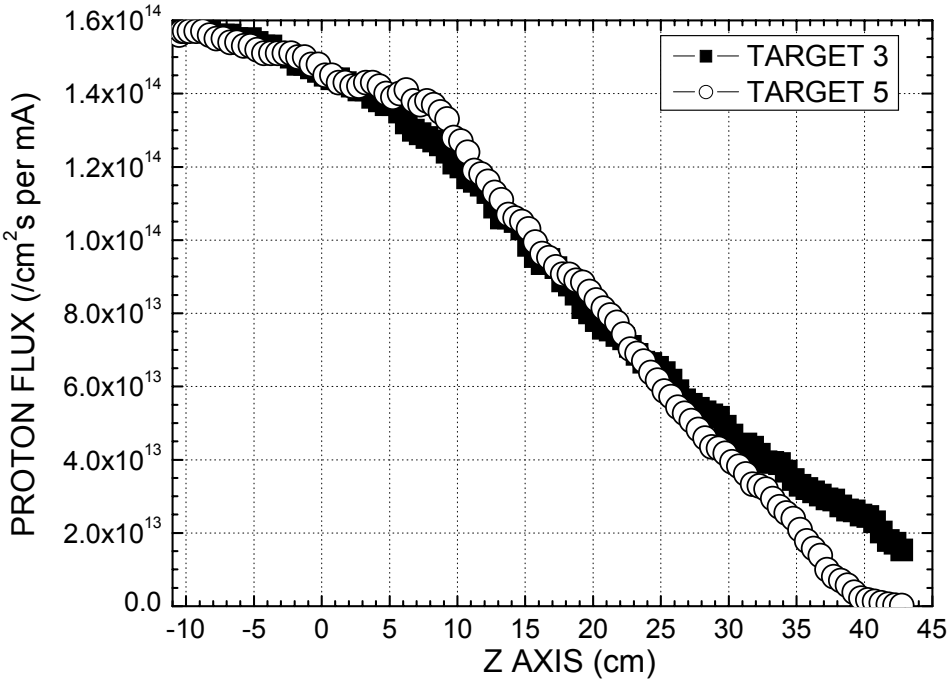

FIG 7.4. Proton fluxes as a function of distance along Z-axis for Targets 3 and 5.

proton flux in the region of 3 cm < Z < 10 cm, where the incident proton beam encounters the first few layers of target rods and the intensive spallation reactions occur. Since lead produces more spallation neutrons and also secondary protons than zirconium, Target 5 shows higher proton flux in this small region.

FIG. 7.5 shows the same case for the neutron fluxes due to neutron energies above 2 x 10^{-7} MeV. The major difference in the neutron fluxes for Targets 3 and 5 exists in the range from Z = 3 cm to Z = 35 cm. The higher neutron flux for Target 5 is attributed to the greater number of spallation neutrons produced in the heavier lead target as compared

to lighter zirconium target. As we analyzed for the neuron production capacity in Chapter 5, at 570 MeV (the incident proton beam energy), the neutrons produced per incident proton are 14.8 and 8.7 for Pb and Zr, respectively. Above Z = 35 cm the higher

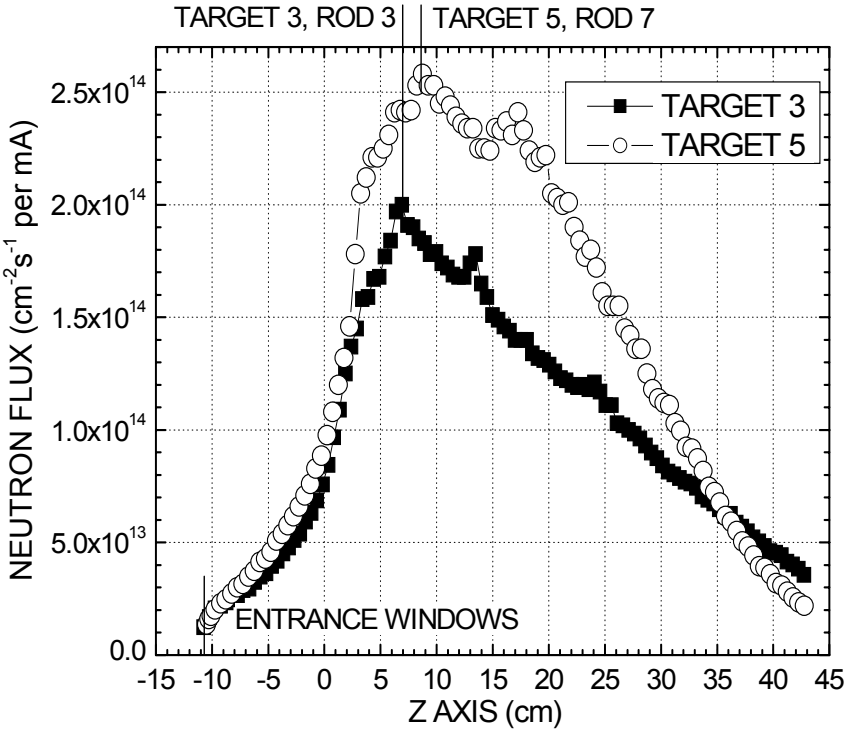

FIG. 7.5. Neutron fluxes as a function of distance along Z-axis for Targets 3 and 5.

neutron flux for Target 3 is attributed to the poorer shielding capacity of zirconium as compared to lead, as is the case for the proton fluxes in FIG. 7.4. The peak neutron flux is reached at Rod 7 in Target 5, and Rod 3 in Target 3. The two rods are actually located in the similar positions in the targets and serve as our checkpoint where maximum neutron flux resides. Another checkpoint is at the lowest tip of the entrance window where maximum proton flux resides (FIG. 7.4).The two curves look like quite close to each other from the entrance windows at Z = -11 cm to about Z = 3 cm, as this region lies

below the spallation target material. However, a further look at the entrance windows may reveal that it is not always the case.

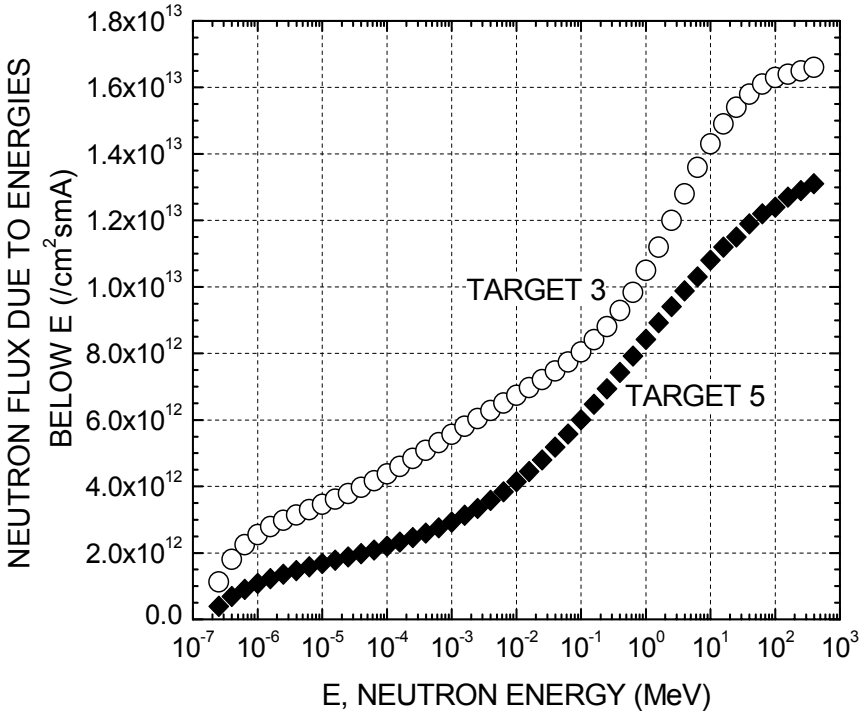

FIG. 7.6. Cumulative neutron flux for the outer entrance windows at SINQ Targets 3 and 5 and at SNS.

FIG. 7.6 shows the cumulative neutron flux at outer entrance windows as a function of neutron energy from 2 x 10^{-7} to 570 MeV for Targets 3 and 5. As observed in FIG. 7.6, Target 3 has higher neutron flux than Target 5 at the outer entrance window, which indicates more neutrons are able to escape the core of Target 3 than that of Target 5. The reason may be again attributed to poorer shielding capacity of zirconium than lead.

TABLE 7.4 shows the calculated displacement productions at the two checkpoints of Targets 3 and 5. Due to the rounding off, Target 3 shows the same displacement production as Target 5 at the outer entrance window. In fact, it has a slightly higher value

due to the higher neutron flux it receives than Target 5. At the places where peak neutron fluxes occur, Target 3 shows lower displacement production due to neutrons at Rod 3 than that at Rod 7 in Target 5. However, even at peak neutron flux the contribution of neutrons to the displacement production can not outweigh that of protons.

TABLE 7.4. Displacement concentrations at the entrance windows of SINQ Targets 3 and 5.

DISPLACEMENTS (dpa/10 Ah)	P	N	P + N
SINQ Windows			
Target 5, Inner Window	4.7	0.7	5.4
Target 5, Outer Window	4.7	0.5	5.2
Target 3, Outer Window	4.7	0.5	5.2
SINQ Rods			
Target 5, Rod 7	11	8	19
Target 3, Rod 3	10	6	16

7.3.2 Significance of the radiation damage productions

At the entrance windows for Target 5, the highest displacement production is 5.4 dpa at the lowest tip of the inner window after an exposure of 10 Ah, as shown in TABLE 7.4. An item of concern is how much damage this amount of displacements will bring to the entrance windows. FIG. 7.7 shows the experimental data of K. Farrell [69] showing tensile properties after irradiation at the HFIR reactor of Al5052 (Al-2.2 wt% Mg), which is an aluminum alloy with close composition to AlMg3, the entrance windows material of Target 5. The blue line designates the displacement production of 5.4 dpa received by the inner entrance windows of Target 5. As observed in FIG. 7.7, a displacement production of 5.4 dpa would be expected to cause a drop in uniform elongation from 14% for the unirradiated alloy to about 7%. Also the total elongation

drops from 37% to 23%. Such reductions in the uniform and total elongations indicate that the material becomes hardened and embrittled. This indicates the necessity of performing further examination on the entrance window material in order to assess its

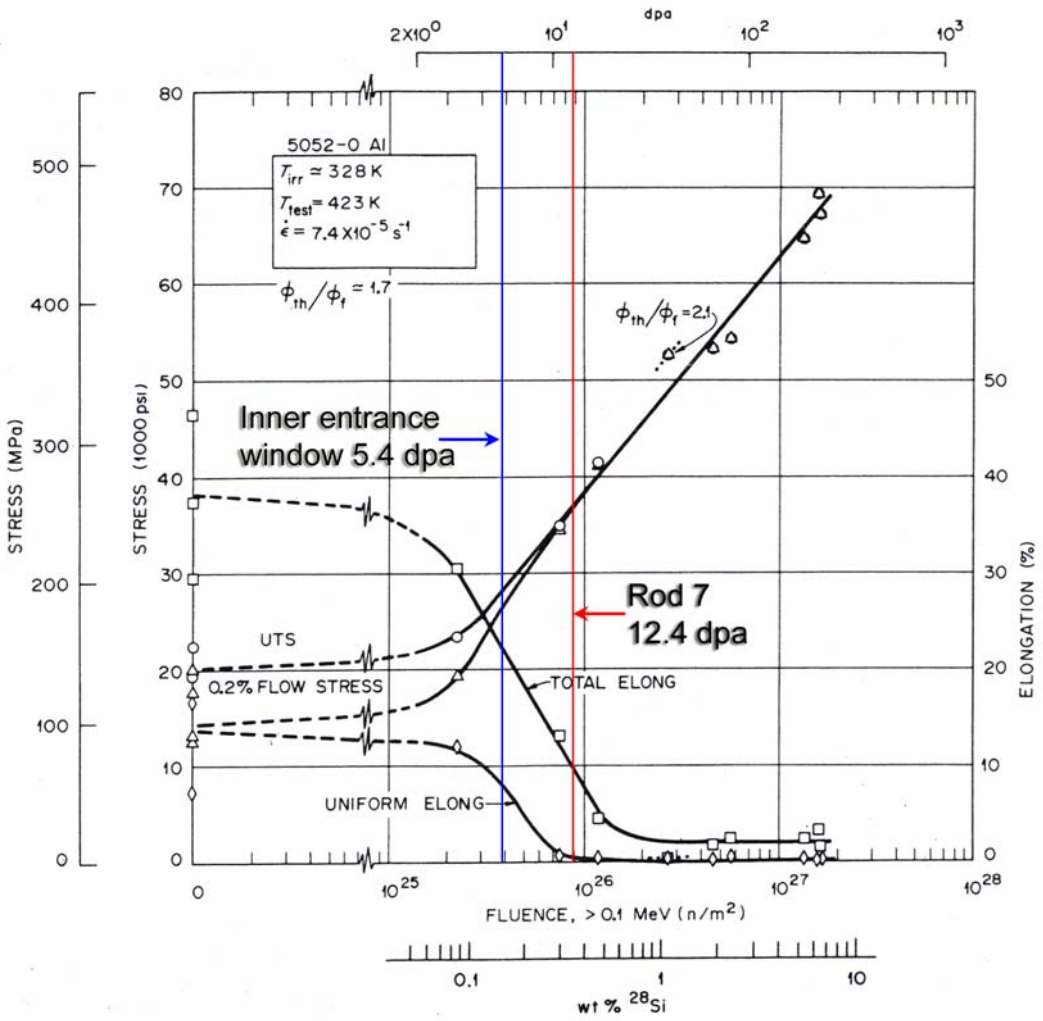

FIG. 7.7 Tensile properties of Al5052 after irradiation (after [69]).

integrity over its working lifetime. In this regard, suppose an aluminum specimen is placed at the center of the Rod 7, the TABLE A.1 in Appendix A indicates that at Rod 7 the aluminum specimen should receive about 12.4 dpa after an exposure of 10 Ah. As shown by the red line the uniform elongation of the specimen would be expected to drop to below 1% and the total elongation to 10%. The experimental data in [68] as shown in

FIG. 7.7 are, however, including the effects of the presence of silicon which also may make the material brittle. Our calculations, as discussed in the next section, show insignificant amount of the silicon produced at the entrance windows in Target 5. But, on the other hand, there is significant gas production, as shown in TABLE 6.4, of about 1150 appmHe and 3400 appmH, and the effect of the gas production may even exceed the effect of silicon in making material brittle.

7.4 Other factors of radiation damage

Besides displacement and gas productions, the transmutation products may bring damage to the material also. One of the transmutation products of concern at the AlMg3 entrance windows is silicon as mentioned in Section 7.3.2. The silicon is produced mainly by the bombardment of thermal neutrons on the aluminum through (n, γ) reactions followed by β decays as shown in Eq. 7.1:

$$\begin{aligned} {}^{27}Al(n,\gamma) &\rightarrow {}^{28}Al \\ {}^{28}Al &\rightarrow {}^{28}Si + \beta \end{aligned} \qquad (7.1)$$

The transmutation-produced silicon then interacts with the dissolved magnesium and forms Mg_2Si precipitate, which is accountable for the strengthening and hardening of the aluminum alloy.

We calculated the silicon productions at the entrance windows of both Targets 3 and 5. The (n, γ) reaction cross sections are downloaded from T2 website (t2.lanl.gov) and are folded into the neutron fluxes at the lowest tips of the entrance windows. The results reveal less than 100 appm of silicon productions in both Targets 3 and 5 after receiving exposures of 6.8 Ah and 10 Ah, respectively. The transmutation-produced silicon is an order less than that already present in the unirradiated alloy, which is 0.29

at%. Therefore, the silicon production by transmutation is insignificant for effects on the properties of the aluminum alloy at the entrance windows.

A further investigation of the transmutation products inside Target 5 includes the Fe-Cr alloy specimens such as HT-9, Eurofer97, T91 and FH82H. Since they all show similar transmutation production spectra, only the transmutation production spectrum of one of them, HT-9 (Fe + 11.8 Cr wt%+1.02 Mo wt%) at Rod 7, is shown in FIG. 7.8. The transmutation products can be categorized into four groups: Carbon Group, Iron Group, Molybdenum Group and Tungsten Group. As can be concluded from the analysis [70], the highest-concentration transmutation impurities are in the range 0.01-0.1 atomic percent and most of them are already present in the unirradiated alloy and have insignificant effects on the specimens.

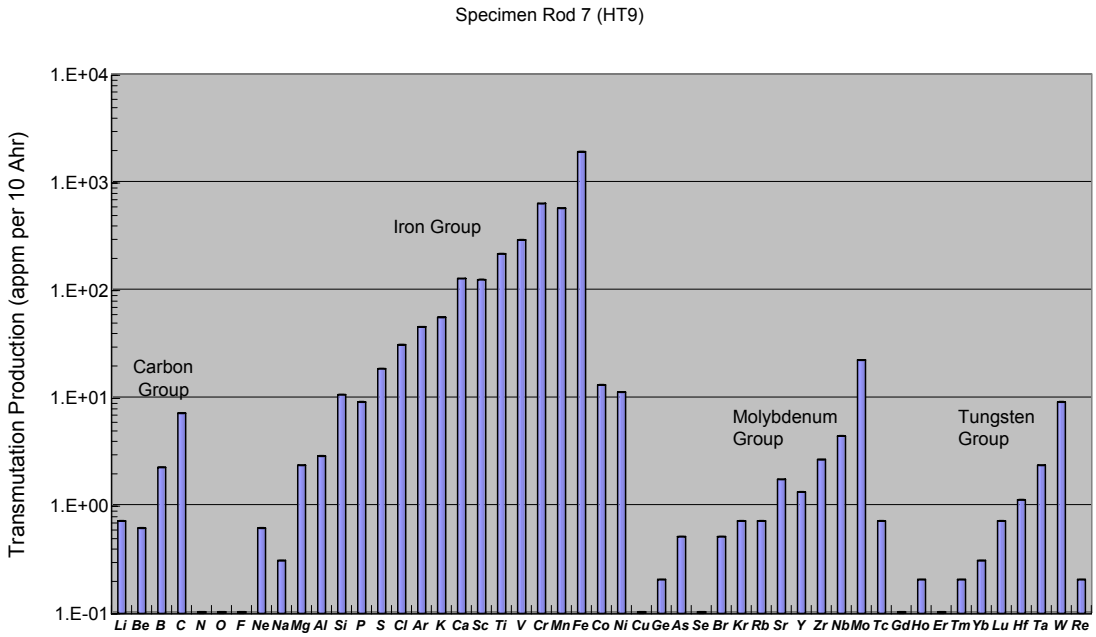

FIG. 7.8. Transmutation Product Concentration Per 10 Ah vs Product Element in Target 5, STIP III.

7.5 Summaries and conclusions

The results of radiation damage calculations of Targets 3 and 5 are further explored in this chapter. A second method is proposed for the calculations, the error of the calculations are analyzed, the results of Targets 3 and 5 are compared, and the transmutation products are discussed. Some of the conclusions can be made as follows:

(1) Method 2, though it requires greater computer capacity and improvement of the MCNPX code, proves itself to be a better method for calculating radiation damage due to its accuracy and convenience.

(2) Some of the helium and hydrogen productions are compared to the experimental data, which reveals a reasonable agreement if errors from both sides are accounted.

(3) Although the spallation target material of Target 5, lead, has a better capacity in producing neutrons and secondary protons than zirconium, the spallation target materials of Target 3, the neutron fluxes at the entrance windows and the higher layers of rods at Target 5 are lower than those at Target 3, due to the poorer shielding capacity of zirconium.

(4) The displacement productions at the entrance windows indicate a significant strengthening and hardening of the aluminum alloy. The entrance windows may be further examined for their working lifetime.

(5) The transmutation products at the entrance windows and specimen rods are not significant compared to their compositions already presented in the alloys. Hence, they have insignificant effects on the properties of the alloys.

Chapter 8

Conclusions

Radiation damage calculations are performed on SINQ Targets 3 and 5. Unlike the conventional calculations, a new method, Method 2, was proposed for its accuracy and convenience. The results from Method 2 on Target 3 were compared to those from Method 1, the conventional method, and showed a good agreement in TABLE 7.1. Due to the limit of computer capacity, the results from Method 2 in TABLE 7.1 so far showed larger statistical errors than those from Method 1. However, with expected improvements in computer capacity and in the MCNPX code in the near future, Method 2 can be expected to yield more precise radiation damage calculations given its convenience in calculation and eliminating errors due to the improper use of cross sections as discussed in Section 7.1.

Besides the radiation damage calculations, the role of spallation reaction physics was explored in the neutron production capacities of the spallation target materials, in which an "infinite" target was used for eliminating the geometry size effect. The number of neutrons produced per incident proton was found proportional to the incident proton energy above an apparent "threshold" energy of about 220 MeV for all the possible spallation target materials calculated here. The relationship between the neutron production capacities of the materials and their atomic number was explored, in which it shows that, for the materials whose atomic number ranges between 73 and 83, their capacities of neutron production are insensitive to the atomic

number. The physics behind this was partly discussed, and areas requiring further study were identified.

Method 1 was performed on the calculations of Target 5, including the geometry modeling, fluxes analysis, cross section development and radiation damage production analysis. The peak proton flux was 1.6 x 10^{14} protons/cm^{2}s per mA and occurred at the lowest tips of the entrance windows which are closest to the incident source beam. The proton flux profile showed a gradually decreasing proton flux along the beam direction. Since the neutrons are mainly produced in spallation reactions under the bombardment of protons upon spallation target rods, the peak neutron flux of 2.4 x 10^{14} protons/cm^{2}s occurred at the center of specimen Rod 7 where the strongest spallation reactions took place. The neutron flux decreased with increasing distance from the center of the peak neutron flux.

The development of the cross sections involved the use of data from three sources: evaluated cross sections from SPECTER/ENDF, LA150 cross sections downloaded from the Internet, and our calculated results from LAHET. The cross sections were then folded into the proton and neutron fluxes to calculate the displacement, helium and hydrogen productions. The lowest tip of the inner entrance window where peak proton flux occurred and the center of the Specimen Rod 7 where peak neutron flux occurred served as checkpoints for the calculations. The radiation damage productions for 10 Ah of exposure are 5.4 dpa, 1350 appmHe and 3400 appmH for the inner entrance window, and 18.6 dpa, 700 appmHe and 7000 appmH for Rod 7 (TABLE 6.4). Due to the combined effect of cross section and flux, protons, not neutrons, make the dominant contribution to the radiation damage productions.

The significance of the radiation damage production was examined against the available experimental data for the aluminum alloy entrance windows and Rod 7, which indicated significant strengthening and hardening of the materials as discussed in Section 7.3.2. Such results further suggested that experimental examinations on the other possible structure materials of a spallation neutron source at places other than the entrance windows and Rod 7 may be necessary. Additional radiation damage calculations, if not covered by our study, are also required.

One of the error sources, cross section sensitivity, for the radiation damage calculations was discussed for the neutron energies below 20 MeV, where the main contribution to displacement production due to neutrons is made, at the two checkpoints, the entrance window and the center of Rod 7. Furthermore, part of the calculation results, helium and hydrogen productions at certain places (the outer entrance window, Rods 5 and 6) in Target 3, were compared with the experimental data. The results showed a good agreement if the errors from both sides are included.

The results from Target 5 were further compared to those from Target 3. Target 5 showed higher neutron fluxes at the spallation reaction core than Target 3 due to its use of lead as spallation target material. Lead is a better material in producing neutrons than zirconium, the spallation target material used in Target 3. Target 5, however, showed lower neutron fluxes at the entrance windows and the higher part of the target ($Z > 25$ cm). The reason lies in the poorer shielding capacity of zirconium compared to that of lead.

Other transmutation products, like the Si production in the aluminum alloy entrance windows, were investigated for their possibility to make contributions to the radiation-induced damage on the material. The results showed insignificant effects of those transmutation products on the materials.

It would be useful to examine in what ways the results of the present investigation may be of benefit in the design of future spallation neutrons sources. The major criterion for the lifetime of a spallation source component is probably the displacements per atom that the component must sustain. For example, our study shows in TABLE 7.4 that the AlMg3 entrance inner window may receive as much as 5.4 dpa in a 10 Ah proton irradiation exposure. Experimental observation has shown that an alloy similar to AlMg3 indicates a decrease in uniform elongation from 14 to 7% for a dose of 5.4 dpa, as shown in FIG. 7.7. This reminds the designer that it would be unwise to permit an aluminum component to receive a dose as high as 5.4 dpa in the practical operation. A similar determination may be made, stemming from our calculations, for using 316SS at locations like Rod 7 where it receives a dose as high as 18.6 dpa, as shown in TABLE 6.5. FIG. 2.2 shows that 316SS undergoes a decrease in uniform elongation from about 50% to almost zero after receiving a dose of 9.3 dpa, only half of the dose it may receive in STIP III.

The major results from the present investigation, radiation damage productions at the specimen rods, are instructive as concerns post-irradiation examinations (PIE). The goal of the examinations is to study the microstructure and mechanical property changes after the irradiation in a spallation spectrum. The design of the experiments has to be based on the knowledge as to what dpa, He, and H doses the specimens may receive due to the STIP irradiation. This knowledge is supplied by calculations like those described in the present study.

Some areas for the future work may be concluded from the present dissertation work, as follows:

(1) More complete investigation of cross sections. A more complete and evaluated cross section database is quite necessary for improving the accuracy of the calculations and the convenience in the other engineering applications.

(2) More detailed analysis of error sources, including the physics model errors in the high energy portion, are necessary for improving the accuracy of the calculations.

(3) Further study on the physics of the neutron production due to the spallation reaction is required to explain the relationship between the incident proton energy and the neutron production capacity of the spallation target material.

Appendices

Appendix A

Radiation damage productions at the specimen rods of Al6061, 9Cr-1Mo, and Zirc-4

TABLE A.1 Displacement, helium and hydrogen productions at the center of specimen rods of Al6061, 9Cr-1Mo and Zirc-4, Beam 2, 10 Ah of irradiation.

Al6061 Rods	Displacement			Helium			Hydrogen		
	Neutron (dpa)	Proton (dpa)	Total (dpa)	Neutron (appm)	Proton (appm)	Total (appm)	Neutron (appm)	Proton (appm)	Total (appm)
Rod1	8.2	4.1	12.3	96	897	993	350	2842	3192
Rod2	8.7	3.7	12.4	100	786	886	376	2528	2904
Rod3	8.5	3.7	12.2	98	774	872	359	2487	2845
Rod4	8.9	3.8	12.7	107	788	896	397	2567	2964
Rod5	8.8	3.4	12.2	99	674	772	376	2252	2628
Rod6	8.8	3.4	12.2	104	670	773	378	2236	2614
Rod7	8.8	3.5	12.4	102	690	793	384	2329	2713
Rod8	9.6	3.1	12.7	102	574	675	389	1993	2382
Rod9	9.6	3.1	12.7	105	568	673	383	1976	2359
Rod10	8.2	3.3	11.6	97	609	707	362	2133	2494
Rod11	7.8	2.8	10.7	85	504	589	326	1799	2126
Rod12	7.7	3.1	10.8	90	540	629	339	1942	2281
Rod13	7.4	2.6	10.0	81	436	517	309	1632	1941
Rod14	7.7	2.6	10.3	87	434	521	336	1616	1952
Rod15	7.5	2.8	10.3	82	462	544	322	1742	2063
Rod16	3.3	0.1	3.4	27	17	44	106	74	179
Rod17T91	3.6	0.2	3.8	31	24	55	122	100	222
Rod17EU97	3.3	0.1	3.4	26	17	44	104	74	178

9Cr1Mo Rods	Displacement			Helium			Hydrogen		
	Neutron (dpa)	Proton (dpa)	Total (dpa)	Neutron (appm)	Proton (appm)	Total (appm)	Neutron (appm)	Proton (appm)	Total (appm)
Rod1	7.0	12.3	19.4	101	754	855	811	7215	8026
Rod2	7.5	11.1	18.6	108	659	767	873	6378	7251
Rod3	7.2	10.9	18.2	104	650	753	837	6279	7116
Rod4	7.7	11.3	19.0	115	662	777	935	6450	7385
Rod5	7.4	10.0	17.5	109	567	677	887	5618	6505
Rod6	7.5	9.9	17.4	109	564	673	884	5578	6462
Rod7	7.5	10.5	18.0	112	582	694	911	5810	6721
Rod8	8.0	9.0	17.1	111	486	598	908	4942	5850
Rod9	8.0	8.9	17.0	111	482	593	902	4896	5798
Rod10	7.0	9.7	16.7	105	518	623	861	5288	6150
Rod11	6.5	8.2	14.8	94	429	523	774	4440	5214
Rod12	6.6	9.0	15.6	99	461	559	814	4802	5617
Rod13	6.1	7.6	13.7	89	375	464	735	3989	4724
Rod14	6.5	7.5	14.0	97	371	467	800	3948	4748
Rod15	6.3	8.2	14.5	93	396	489	770	4258	5028
Rod16	2.5	0.3	2.8	30	14	45	247	161	408
Rod17T91	2.8	0.4	3.2	34	20	54	279	219	498
Rod17EU97	2.5	0.3	2.8	30	14	44	240	161	401

Zirc-4 Rods	Displacement			Helium			Hydrogen		
	Neutron (dpa)	Proton (dpa)	Total (dpa)	Neutron (appm)	Proton (appm)	Total (appm)	Neutron (appm)	Proton (appm)	Total (appm)
Rod1	7.7	26.5	34.2	47	1175	1222	397	7289	7685
Rod2	8.2	23.6	31.8	49	1028	1077	420	6318	6738
Rod3	8.0	23.2	31.2	48	1014	1062	409	6221	6631
Rod4	8.5	23.9	32.4	54	997	1051	462	6346	6808
Rod5	8.2	21.0	29.2	51	814	864	433	5440	5873
Rod6	8.3	20.8	29.2	53	809	862	447	5408	5855
Rod7	8.4	21.9	30.3	53	835	888	454	5585	6039
Rod8	8.9	18.9	27.7	52	700	752	446	4686	5132
Rod9	8.9	18.7	27.6	53	693	746	449	4641	5090
Rod10	7.9	20.3	28.2	53	751	804	444	5006	5450
Rod11	7.3	17.2	24.5	45	628	673	386	4183	4569
Rod12	7.4	18.8	26.1	48	681	729	410	4527	4937
Rod13	6.9	15.6	22.5	43	551	594	367	3748	4116
Rod14	7.3	15.4	22.7	48	547	595	411	3719	4130
Rod15	7.1	16.7	23.8	44	578	622	382	3986	4368
Rod16	2.7	0.5	3.3	12	19	31	108	149	257
Rod17T91	3.0	0.7	3.8	14	26	39	124	202	326
Rod17EU97	2.7	0.6	3.2	10	19	29	98	149	247

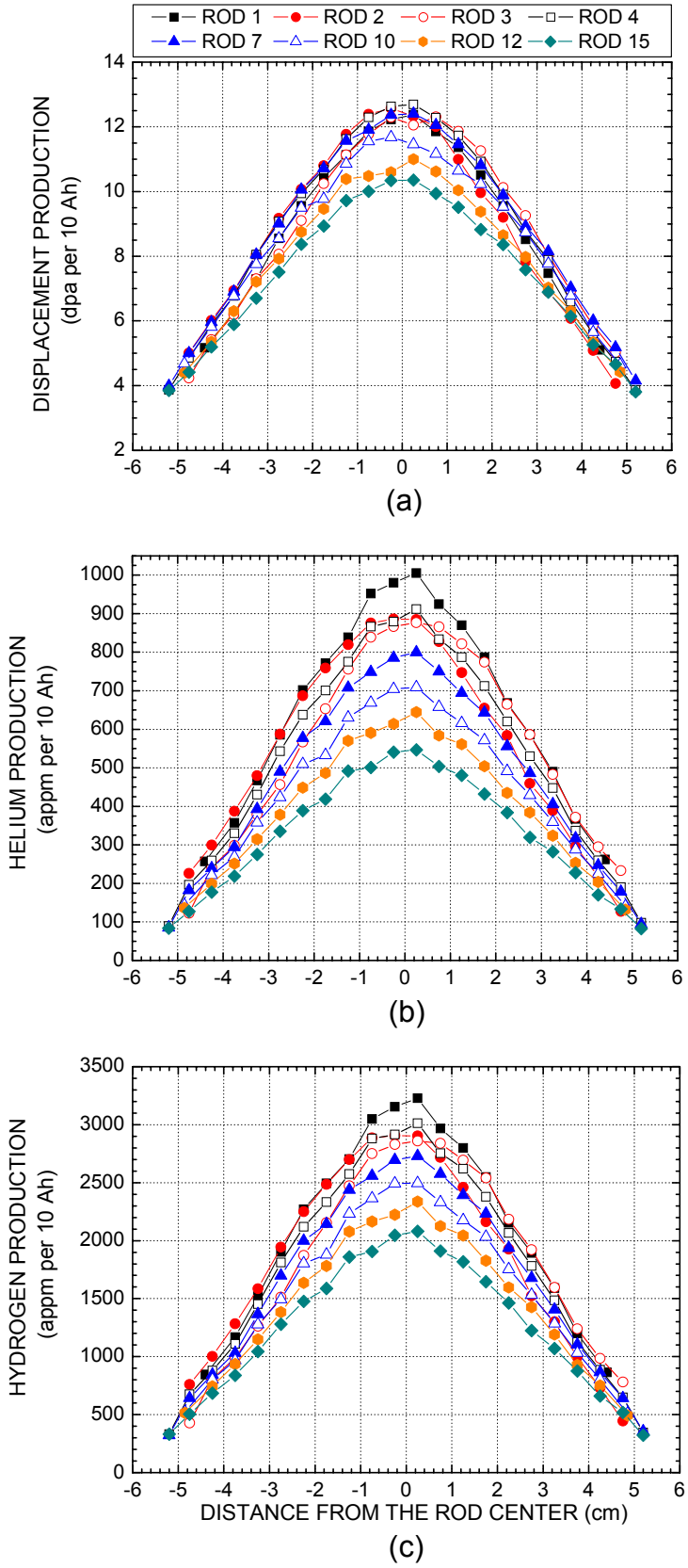

FIG. A.1 Displacement, helium, and hydrogen productions at Al6061 rods, Beam 2.

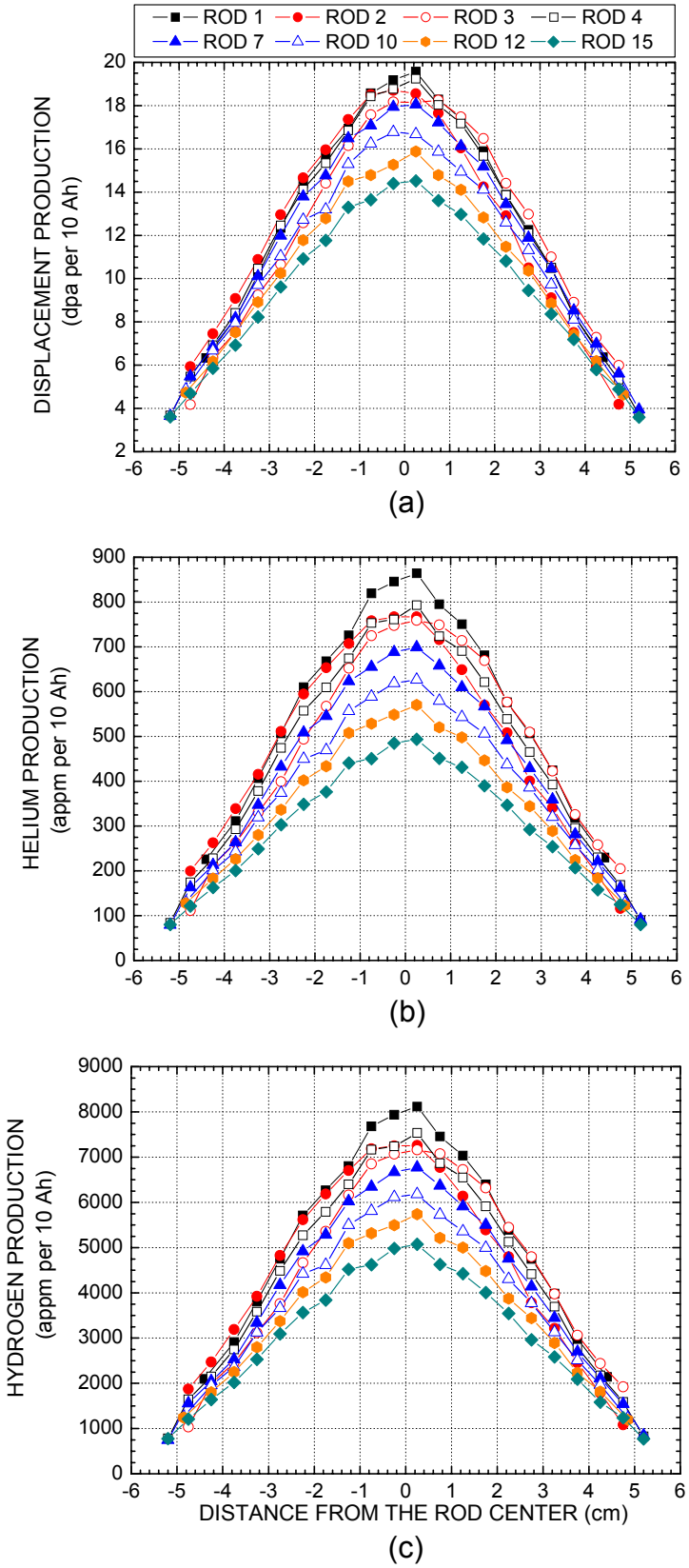

FIG. A.2 Displacement, helium, and hydrogen productions at 9Cr-1Mo rods, Beam 2.

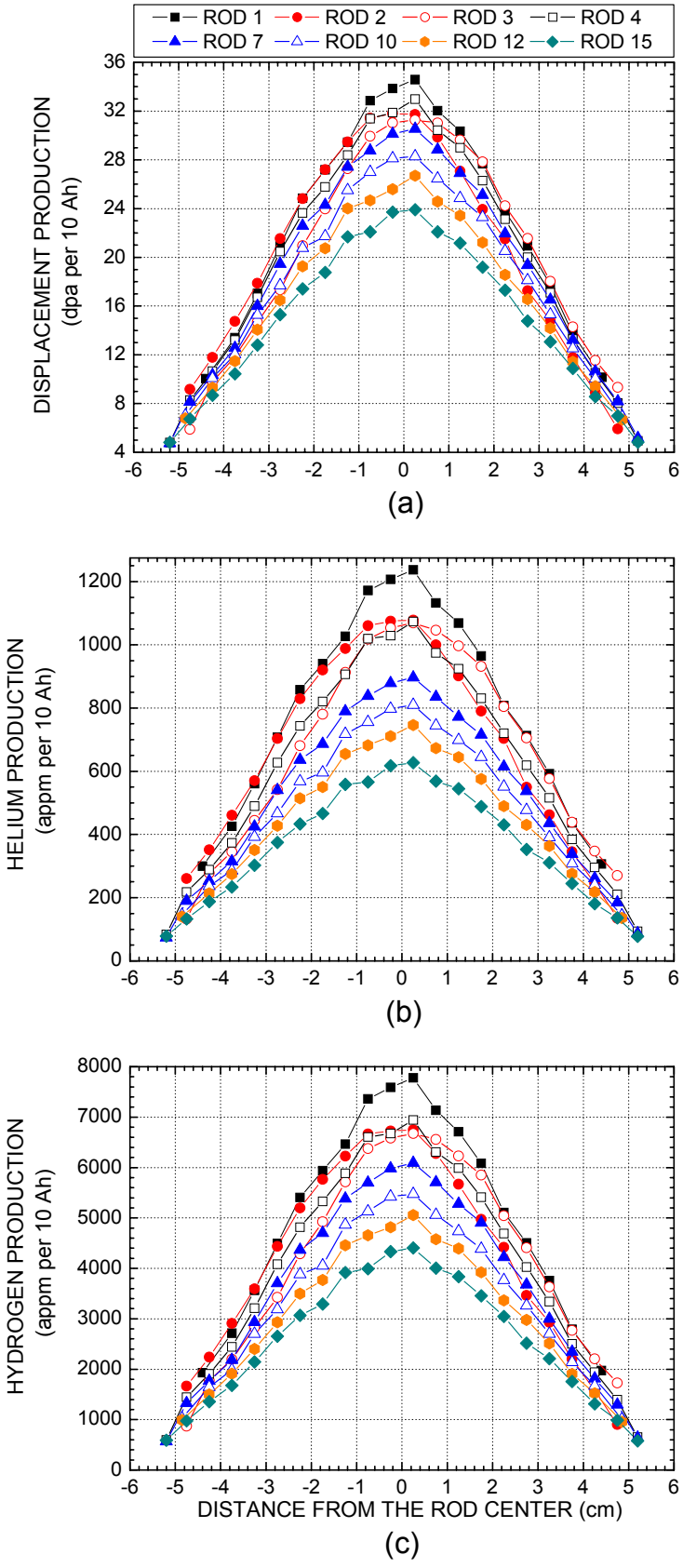

FIG. A.3 Displacement, helium, and hydrogen productions at Zirc-4 rods, Beam 2.

Appendix B

Part of Source codes for “Xscal” program

```
// XScalDlg.cpp : implementation file
//

#include "stdafx.h"
#include "XScal.h"
#include "XScalDlg.h"
#include "DirDialog.h"
#include "CalprocDialog.h"

#ifdef _DEBUG
#define new DEBUG_NEW
#undef THIS_FILE
static char THIS_FILE[] = __FILE__;
#endif


char *elementNames[8]={"Al","Si","Cr","Mn","Fe","Ni","Zn","Zr"};
int elementNo[8]={13,14,24,25,26,28,30,40};
float atomDensity[8]={0.06,0.06,0.06,0.06,0.06,0.06,0.06,0.06};
char *calitemCol[5]={"Element","Library","Particel","Lev. Den.", "Cross Sections"};


/////////////////////////////////////////////////////////////////////////////
// CAboutDlg dialog used for App About

class CAboutDlg : public CDialog
{
public:
	CAboutDlg();

// Dialog Data
	//{{AFX_DATA(CAboutDlg)
	enum { IDD = IDD_ABOUTBOX };
	//}}AFX_DATA

	// ClassWizard generated virtual function overrides
	//{{AFX_VIRTUAL(CAboutDlg)
	protected:
	virtual void DoDataExchange(CDataExchange* pDX);    // DDX/DDV support
	//}}AFX_VIRTUAL

// Implementation
protected:
	//{{AFX_MSG(CAboutDlg)
	//}}AFX_MSG
	DECLARE_MESSAGE_MAP()
};

CAboutDlg::CAboutDlg() : CDialog(CAboutDlg::IDD)
```

```
{
	//{{AFX_DATA_INIT(CAboutDlg)
	//}}AFX_DATA_INIT
}

void CAboutDlg::DoDataExchange(CDataExchange* pDX)
{
	CDialog::DoDataExchange(pDX);
	//{{AFX_DATA_MAP(CAboutDlg)
	//}}AFX_DATA_MAP
}

BEGIN_MESSAGE_MAP(CAboutDlg, CDialog)
	//{{AFX_MSG_MAP(CAboutDlg)
		// No message handlers
	//}}AFX_MSG_MAP
END_MESSAGE_MAP()

/////////////////////////////////////////////////////////////////////////////
// CXScalDlg dialog

CXScalDlg::CXScalDlg(CWnd* pParent /*=NULL*/)
	: CDialog(CXScalDlg::IDD, pParent)
{
	//{{AFX_DATA_INIT(CXScalDlg)
	m_iIncp = 0;
	m_iLevd = 0;
	m_iEnergy = 0;
	m_bDispl = TRUE;
	m_bHe = TRUE;
	m_bH = TRUE;
	m_strLibs = _T("");
	m_iIncr = 0;
	//}}AFX_DATA_INIT
	// Note that LoadIcon does not require a subsequent DestroyIcon in Win32
	m_hIcon = AfxGetApp()->LoadIcon(IDR_MAINFRAME);
}

void CXScalDlg::DoDataExchange(CDataExchange* pDX)
{
	CDialog::DoDataExchange(pDX);
	//{{AFX_DATA_MAP(CXScalDlg)
	DDX_Control(pDX, IDC_LISTenergy, m_clistEnergy);
	DDX_Control(pDX, IDC_LISTlibs, m_clistLibs);
	DDX_Control(pDX, IDC_LISTcal, m_clistctrlCal);
	DDX_Control(pDX, IDC_COMBOwdir, m_ccombWdir);
	DDX_Control(pDX, IDC_COMBOele, m_ccombEle);
	DDX_Radio(pDX, IDC_RADIOincp, m_iIncp);
	DDX_Radio(pDX, IDC_RADIOlevd, m_iLevd);
	DDX_Radio(pDX, IDC_RADIOenergy, m_iEnergy);
	DDX_Check(pDX, IDC_CHECKdispl, m_bDispl);
	DDX_Check(pDX, IDC_CHECKhe, m_bHe);
	DDX_Check(pDX, IDC_CHECKh, m_bH);
	DDX_LBString(pDX, IDC_LISTlibs, m_strLibs);
	DDX_Radio(pDX, IDC_RADIOincr, m_iIncr);
	//}}AFX_DATA_MAP
}

BEGIN_MESSAGE_MAP(CXScalDlg, CDialog)
	//{{AFX_MSG_MAP(CXScalDlg)
```

```
	ON_WM_SYSCOMMAND()
	ON_WM_PAINT()
	ON_WM_QUERYDRAGICON()
	ON_CBN_SELENDOK(IDC_COMBOele, OnSelendokCOMBOele)
	ON_BN_CLICKED(IDC_RADIOenergy, OnRADIOenergy)
	ON_BN_CLICKED(IDC_RADIO7, OnRadio7)
	ON_BN_CLICKED(IDC_BUTTONimpE, OnBUTTONimpE)
	ON_LBN_SELCHANGE(IDC_LISTenergy, OnSelchangeLISTenergy)
	ON_BN_CLICKED(IDC_BUTTONremE, OnBUTTONremE)
	ON_EN_CHANGE(IDC_EDITfrom, OnChangeEDITfrom)
	ON_BN_CLICKED(IDC_BUTTONbrowse, OnBUTTONbrowse)
	ON_LBN_SELCHANGE(IDC_LISTlibs, OnSelchangeLISTlibs)
	ON_BN_CLICKED(IDC_BUTTONadd, OnBUTTONadd)
	ON_BN_CLICKED(IDC_BUTTONrem, OnBUTTONrem)
	ON_NOTIFY(NM_CLICK, IDC_LISTcal, OnClickLISTcal)
	ON_BN_CLICKED(IDC_BUTTONaddE, OnBUTTONaddE)
	ON_EN_UPDATE(IDC_EDITfrom, OnUpdateEDITfrom)
	ON_EN_KILLFOCUS(IDC_EDITfrom, OnKillfocusEDITfrom)
	ON_EN_UPDATE(IDC_EDITto, OnUpdateEDITto)
	ON_EN_KILLFOCUS(IDC_EDITto, OnKillfocusEDITto)
	ON_EN_UPDATE(IDC_EDITincr, OnUpdateEDITincr)
	ON_EN_KILLFOCUS(IDC_EDITincr, OnKillfocusEDITincr)
	ON_BN_CLICKED(IDC_BUTTONsaveE, OnBUTTONsaveE)
	ON_BN_CLICKED(IDC_BUTTONcal, OnBUTTONcal)
	//}}AFX_MSG_MAP
END_MESSAGE_MAP()

/////////////////////////////////////////////////////////////////////////////
// CXScalDlg message handlers

BOOL CXScalDlg::OnInitDialog()
{
	CDialog::OnInitDialog();

	// Add "About..." menu item to system menu.

	// IDM_ABOUTBOX must be in the system command range.
	ASSERT((IDM_ABOUTBOX & 0xFFF0) == IDM_ABOUTBOX);
	ASSERT(IDM_ABOUTBOX < 0xF000);

	CMenu* pSysMenu = GetSystemMenu(FALSE);
	if (pSysMenu != NULL)
	{
		CString strAboutMenu;
		strAboutMenu.LoadString(IDS_ABOUTBOX);
		if (!strAboutMenu.IsEmpty())
		{
			pSysMenu->AppendMenu(MF_SEPARATOR);
			pSysMenu->AppendMenu(MF_STRING, IDM_ABOUTBOX,
strAboutMenu);
		}
	}

	// Set the icon for this dialog.  The framework does this automatically
	//  when the application's main window is not a dialog
	SetIcon(m_hIcon, TRUE);			// Set big icon
	SetIcon(m_hIcon, FALSE);		// Set small icon

	// TODO: Add extra initialization here
	for(int i=0; i<8; i++)  //initialization for the element combox
```

```
		m_ccombEle.AddString(elementNames[i]);

		//initialization for the list view of the items for calculation
	LV_COLUMN lvc;
	//LV_ITEM lvi;
	lvc.mask=LVCF_FMT|LVCF_WIDTH|LVCF_TEXT|LVCF_SUBITEM;
	lvc.fmt=LVCFMT_CENTER;

	for(i=0;i<5;i++){
		lvc.pszText=calitemCol[i];
		lvc.cx=m_clistctrlCal.GetStringWidth(calitemCol[i])+33;
		lvc.iSubItem=i;
		m_clistctrlCal.InsertColumn(i,&lvc);
	}

	return TRUE;  // return TRUE  unless you set the focus to a control
}

void CXScalDlg::OnSysCommand(UINT nID, LPARAM lParam)
{
	if ((nID & 0xFFF0) == IDM_ABOUTBOX)
	{
		CAboutDlg dlgAbout;
		dlgAbout.DoModal();
	}
	else
	{
		CDialog::OnSysCommand(nID, lParam);
	}
}

// If you add a minimize button to your dialog, you will need the code below
//  to draw the icon.  For MFC applications using the document/view model,
//  this is automatically done for you by the framework.

void CXScalDlg::OnPaint()
{
	if (IsIconic())
	{
		CPaintDC dc(this); // device context for painting

		SendMessage(WM_ICONERASEBKGND, (WPARAM) dc.GetSafeHdc(), 0);

		// Center icon in client rectangle
		int cxIcon = GetSystemMetrics(SM_CXICON);
		int cyIcon = GetSystemMetrics(SM_CYICON);
		CRect rect;
		GetClientRect(&rect);
		int x = (rect.Width() - cxIcon + 1) / 2;
		int y = (rect.Height() - cyIcon + 1) / 2;

		// Draw the icon
		dc.DrawIcon(x, y, m_hIcon);
	}
	else
	{
		CDialog::OnPaint();
	}
}
```

```
// The system calls this to obtain the cursor to display while the user drags
//  the minimized window.
HCURSOR CXScalDlg::OnQueryDragIcon()
{
	return (HCURSOR) m_hIcon;
}

void CXScalDlg::OnSelendokCOMBOele()
{
	// TODO: Add your control notification handler code here
	char szBuf[256] = "\0";
	unsigned int i,indexEle;
	// first get the index of the selected element from the comboEle
	indexEle=m_ccombEle.GetCurSel();

	// search the system if there is a "datapath" for storing cross sections
	// headfile
	i=GetEnvironmentVariable("datapath", szBuf, 256);
	if (i==0)
		MessageBox("Can not find any XS data in the system", "Error",
MB_OK|MB_ICONSTOP);
	else{// if the search for xsdir is successful, search the libraries for the selected element
		CString fileName;
		fileName+=szBuf;
		fileName+="\\xsdir";
		CStdioFile xsFile;
		xsFile.Open(fileName, CFile::modeRead);
		// first clear those already inside the library listbox
		int itemNo=m_clistLibs.GetCount();
		for(int l=0;l<itemNo;l++)
			m_clistLibs.DeleteString(0);
		// then add the searched libs into library listbox
		char buf[200],buf2[15],buf3[15];
		while(xsFile.ReadString(buf,199)!=NULL){
			sscanf(buf,"%s",buf2);
			if (strcmp(buf2,"directory")==0)	break;
		}
		while(xsFile.ReadString(buf,199)!=NULL){
			sscanf(buf,"%s",buf2);
			int len=strlen(buf2);
			if (buf2[len-1]=='c'||buf2[len-1]=='h'||buf2[len-1]=='u'){
				strcpy(buf3,buf2);
				buf2[len-1]='\0';
				float lib;
				sscanf(buf2,"%f",&lib);
				if ((int)(lib/1000)==elementNo[indexEle])
m_clistLibs.AddString(buf3);
			}
		}
		//if no library found
		if (m_clistLibs.GetCount()==0)
			MessageBox("No XS libs found for the selected element", "Error",
MB_OK|MB_ICONSTOP);
	}

}

void CXScalDlg::OnRADIOenergy()
{
	// TODO: Add your control notification handler code here
```

```
	GetDlgItem(IDC_EDITfrom)->EnableWindow(TRUE);
	GetDlgItem(IDC_EDITto)->EnableWindow(TRUE);
	GetDlgItem(IDC_EDITincr)->EnableWindow(TRUE);
	GetDlgItem(IDC_BUTTONimpE)->EnableWindow(FALSE);
}

void CXScalDlg::OnRadio7()
{
	// TODO: Add your control notification handler code here
	GetDlgItem(IDC_BUTTONimpE)->EnableWindow(TRUE);
	GetDlgItem(IDC_EDITfrom)->EnableWindow(FALSE);
	GetDlgItem(IDC_EDITto)->EnableWindow(FALSE);
	GetDlgItem(IDC_EDITincr)->EnableWindow(FALSE);
	GetDlgItem(IDC_BUTTONaddE)->EnableWindow(FALSE);
}

void CXScalDlg::OnBUTTONimpE()
{
	// TODO: Add your control notification handler code here
	// open a file open dialog to select an input file,
	// get the file path at the same time and show data into listbox energy
	CFileDialog fdlg(TRUE,NULL,NULL,OFN_HIDEREADONLY,NULL,NULL);
	if(fdlg.DoModal()==IDOK){
		CString fileName;
		fileName=fdlg.GetPathName();
		CStdioFile inputFile;
		inputFile.Open(fileName, CFile::modeRead);
		int strNO=m_clistEnergy.GetCount();
		for(int i=0;i<strNO;i++){
			m_clistEnergy.DeleteString(0);
		}
		char buf[200];
		while(inputFile.ReadString(buf,199)!=NULL)
			m_clistEnergy.AddString(buf);
	}
	if (m_clistEnergy.GetCount()>0)
		GetDlgItem(IDC_BUTTONsaveE)->EnableWindow(TRUE);
}

void CXScalDlg::OnSelchangeLISTenergy()
{
	// TODO: Add your control notification handler code here
	GetDlgItem(IDC_BUTTONremE)->EnableWindow(TRUE);
}

void CXScalDlg::OnBUTTONremE()
{
	// TODO: Add your control notification handler code here
	unsigned int i;
	i=m_clistEnergy.GetCurSel();
	m_clistEnergy.DeleteString(i);
	if(m_clistEnergy.GetCount()==0){
		GetDlgItem(IDC_BUTTONremE)->EnableWindow(FALSE);
		GetDlgItem(IDC_BUTTONsaveE)->EnableWindow(FALSE);
	}
}


void CXScalDlg::OnChangeEDITfrom()
{
```

```
	// TODO: If this is a RICHEDIT control, the control will not
	// send this notification unless you override the CDialog::OnInitDialog()
	// function and call CRichEditCtrl().SetEventMask()
	// with the ENM_CHANGE flag ORed into the mask.

	// TODO: Add your control notification handler code here
	GetDlgItem(IDC_BUTTONaddE)->EnableWindow(TRUE);
}

void CXScalDlg::OnBUTTONbrowse()
{
	// TODO: Add your control notification handler code here
	CDirDialog myDir;
	//myDir.m_strSelDir=_T("C:\\");
	myDir.m_strTitle=_T("Please select a folder for calculation");
	if(myDir.DoBrowse()){
		m_ccombWdir.InsertString(0,myDir.m_strPath);
		m_ccombWdir.SetCurSel(0);
	}
}

void CXScalDlg::OnSelchangeLISTlibs()
{
	// TODO: Add your control notification handler code here
	GetDlgItem(IDC_BUTTONadd)->EnableWindow(TRUE);
}

void CXScalDlg::OnBUTTONadd()
{
	// TODO: Add your control notification handler code here
	UpdateData(TRUE);
	if(!m_bDispl && !m_bH && !m_bHe)
		MessageBox("Please select a cross section for calculations", "Warning",
MB_OK|MB_ICONWARNING);
	else{
		LV_ITEM lvi;
		char *rowDetail[5];
		lvi.mask=LVIF_TEXT;
		lvi.iSubItem=0;
		rowDetail[0]=elementNames[m_ccombEle.GetCurSel()];
		char strTemp[20],strTemp2[20];
		m_clistLibs.GetText(m_clistLibs.GetCurSel(),strTemp2);
		rowDetail[1]=strTemp2;
		if (m_iIncp==0)
			rowDetail[2]="Proton";
		else
			rowDetail[2]="Neutron";
		if (m_iLevd==0)
			rowDetail[3]="GCCI";
		else if (m_iLevd==1)
			rowDetail[3]="HETC";
		else
			rowDetail[3]="Julich";
		rowDetail[4]="\0";
		strTemp[0]='\0';
		if (m_bDispl)
			strcat(strTemp,"Displ.,");
		if (m_bHe)
			strcat(strTemp,"He,");
		if (m_bH)
```

```
                        strcat(strTemp,"H");
                rowDetail[4]=strTemp;
                if (ItemExistCheck(rowDetail))
                        MessageBox("This item is already in the queue", "Warning",
MB_OK|MB_ICONWARNING);
                else{
                        lvi.pszText=rowDetail[0];
                        lvi.iItem=0;
                        m_clistctrlCal.InsertItem(&lvi);
                        for (int i=1;i<5;i++)
                                m_clistctrlCal.SetItemText(0,i,rowDetail[i]);
                }
        }
        if (m_clistctrlCal.GetItemCount())
                GetDlgItem(IDC_BUTTONcal)->EnableWindow(TRUE);

}

void CXScalDlg::OnBUTTONrem()
{
        // TODO: Add your control notification handler code here
        POSITION pos=m_clistctrlCal.GetFirstSelectedItemPosition();
        if (pos==NULL)
                MessageBox("Please select an item", "Warning", MB_OK|MB_ICONWARNING);
        else{
                while(pos)
                        m_clistctrlCal.DeleteItem(m_clistctrlCal.GetNextSelectedItem(pos));
        }
        if (m_clistctrlCal.GetItemCount()==0){
                GetDlgItem(IDC_BUTTONrem)->EnableWindow(FALSE);
                GetDlgItem(IDC_BUTTONrem)->EnableWindow(FALSE);
        }

}



void CXScalDlg::OnClickLISTcal(NMHDR* pNMHDR, LRESULT* pResult)
{
        // TODO: Add your control notification handler code here
        GetDlgItem(IDC_BUTTONrem)->EnableWindow(TRUE);
        *pResult = 0;
}

void CXScalDlg::OnBUTTONaddE()
{
        // TODO: Add your control notification handler code here
        float addStart,addEnd;
        int addNO,inNO,mark;
   CString strEditText;
        GetDlgItem(IDC_EDITfrom)->GetWindowText(strEditText);
        int lenFrom=strEditText.GetLength();
        float From=-1.0,To=-1.0,Incr=-1.0;
        if (lenFrom>0)
                sscanf(strEditText,"%f",&From);
        GetDlgItem(IDC_EDITto)->GetWindowText(strEditText);
        int lenTo=strEditText.GetLength();
        if (lenTo>0)
                sscanf(strEditText,"%f",&To);
        GetDlgItem(IDC_EDITincr)->GetWindowText(strEditText);
```

```
	int lenIncr=strEditText.GetLength();
	if (lenIncr>0)
		sscanf(strEditText,"%f",&Incr);
	UpdateData(TRUE);

	bool insert=true;
	if(Incr<=0.0){//if the increment is 0, insert the input energy in
		// from or to edit box, or both if applicable
		if (From <=0.0 && To <=0.0){
			insert=false;
			MessageBox("Please enter correct energy point", "Warning",
MB_OK|MB_ICONWARNING);
		}
		else if (From>0.0 && To <=0.0){
			addStart=From;
			addEnd=From;
			addNO=1;
		}
		else if (From<=0.0 && To >0.0){
			addStart=To;
			addEnd=To;
			addNO=1;
		}
		else{
			if (From > To){
				insert=false;
				MessageBox("Starting energy point should not be greater than end
point", "Warning", MB_OK|MB_ICONWARNING);
			}
			else if (From==To){
				addStart=From;
				addNO=1;
			}
			else{
				addStart=From;
				addEnd=To;
				addNO=2;
			}
		}
	}
	else{// if the increment is >0, validate the input in from and to edit box
		if (From <=0.0 || To <=0.0){
			insert=false;
			MessageBox("Please enter correct energy point", "Warning",
MB_OK|MB_ICONWARNING);
		}
		else{
			if (From >= To){
				insert=false;
				MessageBox("Starting energy point should not be less than end
point", "Warning", MB_OK|MB_ICONWARNING);
			}
			else{
				addStart=From;
				addEnd=To;
				addNO=1;
				float middle=addStart;
				while (middle<addEnd){
					if (m_iIncr==0)
						middle+=Incr;
```

```
                                        else{
                                                if (Incr>1.0)
                                                        middle=middle*Incr;
                                                else{
                                                        insert=false;
                                                        MessageBox("For Loglinear scale,
increment should be greater than 1.0", "Warning", MB_OK|MB_ICONWARNING);
                                                        break;
                                                }

                                        }
                                        addNO++;
                                }
                        }
                }
        }
        CString strAddFloatText;
        if (insert){
                float tempF;
                inNO=m_clistEnergy.GetCount();
                if(inNO==0){
                        tempF=addStart;
                        while(addNO>0 && tempF<= addEnd){
                                strAddFloatText.Format("%.6e",    tempF);
                                m_clistEnergy.InsertString(-1,strAddFloatText);
                                addNO--;
                                if (Incr>0.0){
                                        if (m_iIncr==0)
                                                tempF+=Incr;
                                        else
                                                tempF=tempF*Incr;
                                }
                                else{
                                        if (addNO>0)
                                                tempF=addEnd;
                                }
                        }
                        if(addNO>0){
                                strAddFloatText.Format("%.6e",    addEnd);
                                m_clistEnergy.InsertString(-1,strAddFloatText);
                        }
                }
                else{
                        float inboxF;
                        CString strListText;
                        mark=0;
                        tempF=addStart;
                        bool everInserted=false;
                        while(addNO>0 && tempF<= addEnd){
                                for(int i=mark;i<inNO;i++){
                                        m_clistEnergy.GetText(i,strListText);
                                        sscanf(strListText,"%f",&inboxF);
                                        if (inboxF>tempF){
                                                strAddFloatText.Format("%.6e",tempF);
                                                m_clistEnergy.InsertString(i,strAddFloatText);
                                                everInserted=true;
                                                mark=i+1;
                                                inNO++;
                                                break;
                                        }
```

```
                                        else if (inboxF==tempF){
                                                everInserted=true;
                                                mark=i+1;
                                                break;
                                        }
                                }
                                if(everInserted)
                                        everInserted=false;
                                else{
                                        strAddFloatText.Format("%.6e",tempF);
                                        m_clistEnergy.InsertString(-1,strAddFloatText);
                                        mark=inNO+1;
                                }
                                addNO--;
                                if (Incr>0.0){
                                        if (m_iIncr==0)
                                                tempF+=Incr;
                                        else
                                                tempF=tempF*Incr;
                                }
                                else{
                                        if (addNO>0)
                                                tempF=addEnd;
                                }
                        }
                        if(addNO>0){
                                for(int i=mark;i<inNO;i++){
                                        m_clistEnergy.GetText(i,strListText);
                                        sscanf(strListText,"%f",&inboxF);
                                        if (inboxF>addEnd){
                                                strAddFloatText.Format("%.6e",addEnd);
                                                m_clistEnergy.InsertString(i,strAddFloatText);
                                                everInserted=true;
                                                mark=i+1;
                                                inNO++;
                                                break;
                                        }
                                        else if (inboxF==addEnd){
                                                everInserted=true;
                                                mark=i+1;
                                                break;
                                        }
                                }
                                if(everInserted)
                                        everInserted=false;
                                else{
                                        strAddFloatText.Format("%.6e",tempF);
                                        m_clistEnergy.InsertString(-1,strAddFloatText);
                                        mark=inNO+1;
                                }
                        }
                }
        }
        if(m_clistEnergy.GetCount()>0)
                GetDlgItem(IDC_BUTTONsaveE)->EnableWindow(TRUE);
}

bool CXScalDlg::FloatValidation(CString &strCurText)
{
        int eNO=0,opNO=0,dotNO=0;
```

```
int ePOS,opPOS,dotPOS;
int i,j, l=strCurText.GetLength();
bool output=true;
float myF;
if (sscanf(strCurText,"%f",&myF)==1){
	for(i=0;i<l;i++){
		j=(int)strCurText[i];
		if ((j>=48 && j<=57) || j==43 || j==45 || j==46 || j==101 || j==69){
			switch(j){
				case 43:
					opNO++;		break;
				case 45:
					opNO++;		break;
				case 46:
					dotNO++; break;
				case 69:
					eNO++; break;
				case 101:
					eNO++; break;
				default: break;
			}
			if(opNO>1 || eNO>1 || dotNO>1){
				output=false;
				break;
			}
			else{
				if (j==43 || j==45)		opPOS=i;
				if (j==46) dotPOS=i;
				if (j==101 || j==69) ePOS=i;
			}
		}
		else{
			output=false;
			break;
		}

	}
}
else{
	if(l>0) output=false;
}

if(output){
	if(eNO==0 && opNO==1)
		output=false;
	else if (eNO==0 && opNO==0)
		output=true;
	else if (eNO==1 && opNO==0 && dotNO==0){
		output=true;
	}
	else if (eNO==1 && opNO==0 && dotNO==1){
		if (dotPOS-ePOS==1)
			output=false;
		else
			output=true;
	}
	else if (eNO==1 && opNO==1 && dotNO==0){
		if (opPOS-ePOS==1)
			output=true;
		else
```

```
                                output=false;
                }
                else{
                        if (opPOS-ePOS==1 && dotPOS<ePOS)
                                output=true;
                        else
                                output=false;
                }

        }

        return output;
}

void CXScalDlg::OnUpdateEDITfrom()
{
        // TODO: If this is a RICHEDIT control, the control will not
        // send this notification unless you override the CDialog::OnInitDialog()
        // function to send the EM_SETEVENTMASK message to the control
        // with the ENM_UPDATE flag ORed into the lParam mask.

        // TODO: Add your control notification handler code here
        static CString strOldText="";
   CString strCurText;
        GetDlgItem(IDC_EDITfrom)->GetWindowText(strCurText);
        if(FloatValidation(strCurText))
                strOldText=strCurText;
        else
                GetDlgItem(IDC_EDITfrom)->SetWindowText(strOldText);
}

void CXScalDlg::OnKillfocusEDITfrom()
{
        // TODO: Add your control notification handler code here
        FloatValidationMore(IDC_EDITfrom);
}

void CXScalDlg::FloatValidationMore(int nID)
{
        CString strCurText;
        GetDlgItem(nID)->GetWindowText(strCurText);
        int l=strCurText.GetLength();
        if(l>=2){
                if((strCurText[l-2]==101    ||    strCurText[l-2]==69)&&    (strCurText[l-1]==43    ||
strCurText[l-1]==45) )
                        strCurText.SetAt(l-2,'\0');
                else  if  (strCurText[l-1]==43  ||  strCurText[l-1]==45  ||  strCurText[l-1]==69  ||
strCurText[l-1]==101)
                        strCurText.SetAt(l-1,'\0');
        }
        else if (l==1){
                if (strCurText[l-1]==43 || strCurText[l-1]==45 || strCurText[l-1]==69 || strCurText[l-
1]==101)
                        strCurText.SetAt(l-1,'\0');
        }
        GetDlgItem(nID)->SetWindowText(strCurText);
}

void CXScalDlg::OnUpdateEDITto()
{
```

```
	// TODO: If this is a RICHEDIT control, the control will not
	// send this notification unless you override the CDialog::OnInitDialog()
	// function to send the EM_SETEVENTMASK message to the control
	// with the ENM_UPDATE flag ORed into the lParam mask.

	// TODO: Add your control notification handler code here
	static CString strOldText="";
   CString strCurText;
	GetDlgItem(IDC_EDITto)->GetWindowText(strCurText);
	if(FloatValidation(strCurText))
		strOldText=strCurText;
	else
		GetDlgItem(IDC_EDITto)->SetWindowText(strOldText);
}

void CXScalDlg::OnKillfocusEDITto()
{
	// TODO: Add your control notification handler code here
	FloatValidationMore(IDC_EDITto);
}


void CXScalDlg::OnUpdateEDITincr()
{
	// TODO: If this is a RICHEDIT control, the control will not
	// send this notification unless you override the CDialog::OnInitDialog()
	// function to send the EM_SETEVENTMASK message to the control
	// with the ENM_UPDATE flag ORed into the lParam mask.

	// TODO: Add your control notification handler code here
	static CString strOldText="";
   CString strCurText;
	GetDlgItem(IDC_EDITincr)->GetWindowText(strCurText);
	if(FloatValidation(strCurText))
		strOldText=strCurText;
	else
		GetDlgItem(IDC_EDITincr)->SetWindowText(strOldText);
}

void CXScalDlg::OnKillfocusEDITincr()
{
	// TODO: Add your control notification handler code here
	FloatValidationMore(IDC_EDITincr);
}

void CXScalDlg::OnBUTTONsaveE()
{
	// TODO: Add your control notification handler code here
	CFileDialog fdlg(FALSE,NULL,NULL,OFN_HIDEREADONLY,NULL,NULL);
	if(fdlg.DoModal()==IDOK){
		CString fileName;
		fileName=fdlg.GetPathName();
		CStdioFile outputFile;
		outputFile.Open(fileName, CFile::modeCreate | CFile::modeWrite);
		int strNO=m_clistEnergy.GetCount();
		CString strListText;
		for (int i=0;i<strNO;i++){
			m_clistEnergy.GetText(i,strListText);
			strListText+="\n";
			outputFile.WriteString(strListText);
```

```
		}
		outputFile.Close();
	}
}

bool CXScalDlg::ItemExistCheck(char *itemText[])
{
	CString strItemText[5],strItemText2[5];
	bool repeated=false;
	int i,j;
	for (i=0;i<5;i++)
		strItemText[i]=itemText[i];
	int itemNO=m_clistctrlCal.GetItemCount();

	for (i=0;i<itemNO;i++){
		int status=0;
		for (j=0;j<5;j++)
			strItemText2[j]=m_clistctrlCal.GetItemText(i,j);
		for (j=0;j<5;j++){
			status+=abs(strItemText2[j].Compare(strItemText[j]));
		}
		if (status==0){
			repeated=true;
			break;
		}
	}

	return repeated;
}

void CXScalDlg::OnBUTTONcal()
{
	// TODO: Add your control notification handler code here
	//validation for the inputs
	CString strErrText=_T("");
	if (m_ccombWdir.GetCurSel()==CB_ERR)
		strErrText+="Need to specify working directory for the calculation!\n";
	if (m_clistEnergy.GetCount()==0)
		strErrText+="Need to input energy scale for the calculation\n";
	if (strErrText.GetLength()>0)
		MessageBox(strErrText, "Warning", MB_OK|MB_ICONWARNING);
	else{
		CCalprocDialog chDlg(this);
		chDlg.DoModal();
	}

}
```